Dune Formation and Sand Transportation on Titan

by

Xinting Yu

A dissertation submitted to The Johns Hopkins University

in conformity with the requirements for the degree of

Doctor of Philosophy

Baltimore, Maryland

March, 2019

Abstract

Nearly 20% of Titan's surface is covered with equatorial linear dunes similar to sand dunes on Earth. However, the sand on Titan is not made of silicates, as on Earth, but mainly of organic materials produced by photochemistry in the atmosphere. The combination of low gravity, high atmospheric density, low temperature, and the unique composition of sand means that additional theoretical and experimental studies are needed to improve our understanding of aeolian sediment transport on Titan. An improved understanding of the minimum wind speed to initiate sand particle movements (threshold wind speed) will better constrain models of the global circulation of Titan's atmosphere. The formation of dune particles on Titan is also not well understood. The particles may be formed by transforming small aerosol particles ($\sim$1 μm) in Titan's atmosphere into large sand-size saltating particles on the surface (100–300 μm). Alternatively, deposits of organics on the surface may be eroded into sand-sized particles. Even though several mechanisms have been proposed for this transformation, there has been no experimental data to help determine which, if any, of the formation mechanisms are occurring.

Here, I experimentally measured the liquid adsorption properties of materials used in the Titan Wind Tunnel (TWT), and modeled the effect of adsorbed

liquid on threshold wind speed for materials frequently used in the TWT, silicate sand on Earth, and organic sand on Titan. I demonstrated that the effect of methane humidity on tholin is similar to the effect of water on silicate sand, but different from the effect of water on the low density wind tunnel materials. I also found that it may be easier to transport “wet" (methane-saturated) sand than “dry" sand on Titan, because the methane capillary force may be smaller than the “dry" adhesion forces between the organic sand particles.

I have also used atomic force microscopy to study the interparticle interactions between Titan aerosol analogues, or ‘tholin’. I found that the interparticle cohesion forces are much larger for tholin and presumably Titan sand particles than for silicate sand and other materials used in the TWT. This suggests that we should increase the interparticle forces in both analog experiments (TWT) and threshold models to correctly translate the results to real Titan conditions. The strong cohesion of tholin also indicates that Titan’s sand could be formed by effective agglomeration of small aerosol particles in the atmosphere.

I have also used nanoindentation to study the mechanical properties of a few Titan sand candidates to understand the mobility of Titan sand. I measured the elastic modulus, hardness, and fracture toughness of these materials. The elastic modulus and hardness of tholin are both an order of magnitude smaller than silicate sand and are smaller than mechanically weak sand like white gypsum sand. With an order of magnitude smaller fracture toughness, tholin is also much more brittle than silicate sand. Other possible Titan sand candidates are also mechanically weaker than sand on Earth. This indicates that Titan sand should be derived close to the equatorial regions

where the current dunes are located, because tholin and other organics are too soft and brittle to be transported for long distances.

The above results suggest that it is more favorable for the Titan sand to be formed by “dry" agglomeration of small aerosol particles. Since the organics have higher cohesion and are less likely to be formed in the polar liquid reservoirs on Titan by “wet" agglomeration, they are not mechanically strong enough to transport long distances to form the equatorial dunes.

Thesis Committee

Primary Readers

Sarah Hörst (Primary Advisor)
Assistant Professor
Department of Earth and Planetary Sciences
Johns Hopkins Krieger School of Arts & Sciences

Kevin Lewis
Assistant Professor
Department of Earth and Planetary Sciences
Johns Hopkins Krieger School of Arts & Sciences

Alternate Readers

Anand Gnanadesikan
Professor
Department of Earth and Planetary Sciences
Johns Hopkins Krieger School of Arts & Sciences

Darrell Strobel
Professor
Department of Earth and Planetary Sciences
Johns Hopkins Krieger School of Arts & Sciences

Acknowledgments

I would like to thank my advisor Sarah Hörst, for the amazing knowledge and skills she passed along to me through this five-year journey, and my committee members Anand Gnanadesikan and Kevin Lewis. I am also grateful to my group members Joe Serigano, Michael Radke, Sarah Moran, Kristin Sotzen, Bryné Hadnott, and Marcella Roth. I would like to express special thanks to Chao He, who devoted lots of time and energy with my experiments. In particular, I would like to thank my wonderful collaborator Patty McGuiggan, who taught me to become a materials science expert, and Nathan Bridges, who started my journey in the dune worlds. I am also grateful to my fellow planetary students such as Hannah Susorney, Kirby Runyon, and Mariah Baker. Thanks to all my Chinese friends, for bringing hometown warmth to me: Wanshu Nie, Yifan Zhou, Chi Yan, Jingyi Huang, Yan Cheng, and Eric Yee.

I am grateful to my parents, Ronggui Mu and Guangming Yu. Without their support, I would not be able to pursue my PhD in a different country. My grandparents have been always supporting me and my grandma Jianmei Chang showed me how a woman could achieve a strong and successful career. Last but not least, I want to thank my dear and loving husband Xu Yang who

drives me everywhere and for all his care and support during my lows and highs.

Table of Contents

List of Tables

List of Figures

Chapter 1

Introduction

Titan is the largest moon of Saturn. As an exotic world it is intriguing because it is the only moon with a substantial atmosphere in our Solar System. The main constituent in Titan's atmosphere is nitrogen (N_2), similar to Earth. The atmospheric pressure is slightly higher on Titan than Earth, about 1.5 bar (Lindal et al., 1983; Fulchignoni et al., 2005; Jennings et al., 2009). Meanwhile, Titan is much colder than Earth, with a surface temperature of merely 94 K. The second most abundant component in Titan's atmosphere is methane (CH_4). Titan's surface temperature and pressure are close to methane's triple point (90.7 K, 0.117 bar), thus similar to the water cycle on Earth, Titan also has an active methane cycle.

In visible light, we cannot see through Titan's atmosphere to the surface. This is because the visible photons are blocked by the photochemically generated thick haze layers in Titan's atmosphere. The haze layers are made of particles produced by complex organic chemistry involving methane, nitrogen, and other trace components like carbon monoxide or benzene. Voyager

1, Cassini and various ground-based telescopes have detected numerous organic compounds in Titan's atmosphere that are photochemically produced, such as ethane (C_2H_6), ethylene (C_2H_4), acetylene (C_2H_2), propane (C_3H_8), propene (C_3H_6), propyne (C_3H_4), diacetylene (C_4H_2), benzene (C_6H_6), hydrogen cyanide (HCN), cyanoacetylene (HC_3N), and cyanogen (C_2N_2) (Hanel et al., 1981; Kunde et al., 1981; Coustenis et al., 2007; Waite et al., 2005, 2007; Nixon et al., 2013). The Cassini Plasma Spectrometer (CAPS) instrument has detected negative ions in Titan's upper atmosphere up to 10,000 m/z (Coates et al., 2007, 2009). Measurements from the Huygens probe suggest that the photochemically generated organic particles could grow up to $\sim$1 μm in diameter when reaching Titan's surface (Tomasko et al., 2005).

However, Titan's atmosphere is transparent in a few infrared windows and at radio wavelengths. The Cassini-Huygens mission utilized this fact and investigated Titan's surface through these wavelengths with three instruments, the Imaging Science Subsystem (ISS), the Visual and Infrared Mapping Spectrometer (VIMS), and Radio Detection and Ranging instrument (RADAR). Titan has a geologically young and diverse surface. In the high latitude regions of Titan, Cassini-Huygens discovered lakes and seas made of methane and ethane (Stofan et al., 2007; Hayes et al., 2008). While in the low latitudes around the equator ($\pm 30^\circ$), Cassini-RADAR found vast areas of repetitive, radar-dark long streaks, which are interpreted as longitudinal dunes (Lorenz et al. 2006; Radebaugh et al. 2008), morphologically similar to the ones in Namib Desert on Earth (Lorenz et al. 2006; Radebaugh et al. 2010). Mountains on Titan are often eroded extensively (Radebaugh et al., 2007; Mitri et

al., 2010; Moore and Pappalardo, 2011). There are only a few impact craters and they are often covered by sediments on the bottom or highly degraded (Lorenz et al., 2007; Wood et al., 2010; Neish and Lorenz, 2012; Moore and Pappalardo, 2011). There are also possible cryovolcanoes (Lopes et al., 2007, 2013; Solomonidou et al., 2014, 2016). So far, several major surface units have been identified on Titan (Lopes et al., 2010, 2016), including labyrinth units (3–5% coverage, mostly at high latitudes), crater units (<1% coverage), hummocky/mountainous units (10–15% coverage, including hills, mountain chains, and blocks, e.g., the Xanadu region), undifferentiated units (15–20% coverage), dune units (15–20% coverage), and fluvial channel and lake units (3-5% coverage).

Titan also has an active climate. Like Earth, Saturn's large obliquity (26.7°) leads to seasonal variations of solar heating, even though Titan's seasons are much longer (7.5 Earth years per season). Titan also has a Hadley cell like Earth, but Titan's Hadley cell can extend all the way from one pole to the other during summer and winter, while it will split into two equator-to-pole cells during equinoxes (Newman et al., 2011; Lebonnois et al., 2012; Vinatier et al., 2015). The single Hadley cell redistributes heat efficiently on Titan, leading to a relatively small temperature difference between the poles and the equator in the troposphere. The Cassini mission spanned from Titan's northern winter (2004) to northern summer (2017), and was able to observe seasonal changes on Titan such as atmospheric composition, temperature structure, and haze structure (Mitchell and Lora, 2016; Hörst, 2017). Hydrocarbon rains and clouds were also observed in Titan's atmosphere and were shown to have

seasonal variations (e.g. Turtle et al., 2009, 2011a, 2011b, 2018; Rodriguez et al., 2009, 2011; Le Mouélic et al., 2018).

1.1 Dunes on Titan

1.1.1 History: Prior to Cassini

Titan is a moon with low gravity and a dense atmosphere, resulting in a low friction threshold wind speed for saltation, around 0.03 m/s (Greeley & Iversen, 1985; Lorenz et al., 1995). Because of the scarce sunlight received by Titan's surface, winds driven by solar heating were predicted to be too weak ($<$0.01 m/s) to form aeolian landforms (Lorenz et al., 1995). However, Titan is tidally locked to Saturn, and the resulting tidal forces could dominate over solar heating in the atmosphere (Tokano & Neubauer, 2002), inducing tidal winds that might be strong enough to saltate sand on Titan.

Tidal forces were predicted to serve as the dominant driver for ocean circulation on Titan, potentially resulting in a friction wind speed of around 0.3–3 mm/s (Sears, 1995). While the wind on Titan's surface was predicted to be insufficient to form dunes on land (Lorenz et al., 1995), undissolved organic sediments that are submerged in Titan's liquid methane reservoirs may be able to form dune-like bedforms, since only $\sim$2 mm/s of threshold friction wind speed is needed there (Lorenz et al., 1995).

Prior to Cassini, it seemed that the available sand-sized grains would be scarce on Titan, which is another reason why aeolian features were unexpected on Titan before Cassini-Huygens. Weathering processes such as thermal cracking and abrasion of bedrock were both estimated to be very weak due to

Titan's low insolation and thick atmosphere. Thus sand formed by weathering and erosion products would not be as abundant as on Earth and Mars. Photochemically formed aerosol particles could be abundant (forming a 50–200 m layer of sediments on Titan's surface), but they may be too sticky (due to small size and potential methane humidity/rain) to be saltated. Another predicted source of sand was impact excavated ejecta particles formed from the bedrock, but the amount predicted to be produced was modest and hydrocarbon lakes and seas may be strong sinks for those sediments (Lorenz et al., 1995).

1.1.2 Dune Morphology

Before being recognized as dunes, hundreds of dark streaks (originally referred to as "cat-scratches") were first observed by the Cassini ISS ($\sim$km resolution). With the Cassini RADAR instrument operating in the 2.17 cm wavelength in the Synthetic Aperture Radar (SAR) mode, achieving a spatial resolution of up to 300 m, these features were first speculated to be linear dunes in the T3 flyby swath (see Figure 1.1; Elachi et al., 2006). More RADAR mapping data then confirmed that these features are longitudinal dunes (see e.g., Lorenz et al., 2006).

These radar dark streaks are tens to hundreds of kilometers long, 500 m to 1 km across, and are separated by 1–2 km (Elachi et al., 2006). Multiple morphological characteristics point to an aeolian origin of these features: 1) the streaks resemble linear dunes found on Earth such as those in the Namib (Figure 1.2), Saharan, and Arabian deserts (Lorenz et al., 2006; Radebaugh et al., 2008, 2010); 2) the subparallel orientation of the structure (Radebaugh et al.,

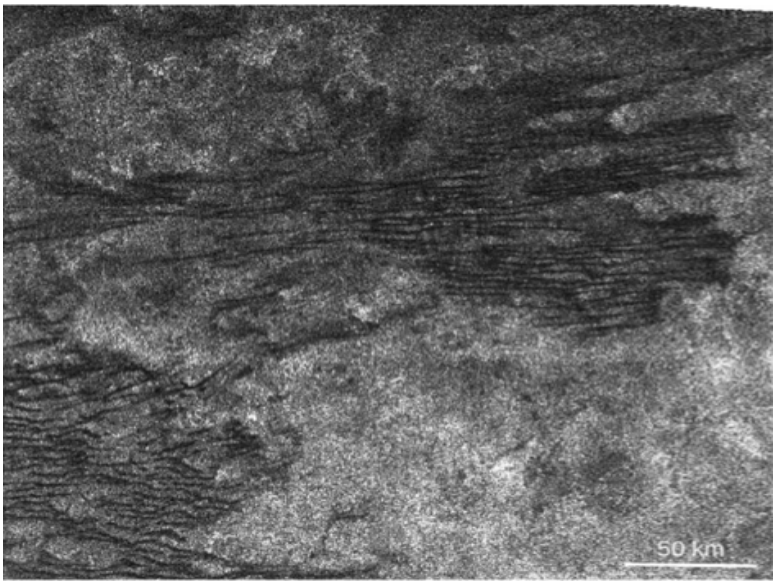

Figure 1.1: Dunes (“cat-scratches") in Cassini/RADAR T3 flyby swath (Figure from Radebaugh et al. 2008).

2008); 3) the streaks have significant slopes of about 6° to 10° and estimated heights of 100–150 m (Lorenz et al., 2006); 4) the streaks’ interaction and superposition on topography (Radebaugh et al., 2007, 2008); 5) the way the streaks merge into Y-shaped or “tuning fork" junctions (e.g. Figure 1.3, Elachi et al., 2006; Lorenz et al., 2006).

Various techniques that used different instruments on Cassini have been developed to retrieve more detailed morphological information of the dunes. Morphological characteristics such as the height and the spacing of dunes have been retrieved through SAR images (Lucas et al., 2014a; Savage et al., 2014), SAR radarclinometry (Lorenz et al., 2006; Neish et al., 2010), SAR-stereo (Kirk et al., 2012), VIMS photoclinometry (Barnes et al., 2008), and RADAR altimetry (Mastrogiuseppe et al., 2014). The dune heights and dune spacings seems to vary with locations, but dune heights are generally between 30–200

Figure 1.2: Longitudinal dunes in the Namib sand sea on Earth (Figure from Lorenz et al. 2006).

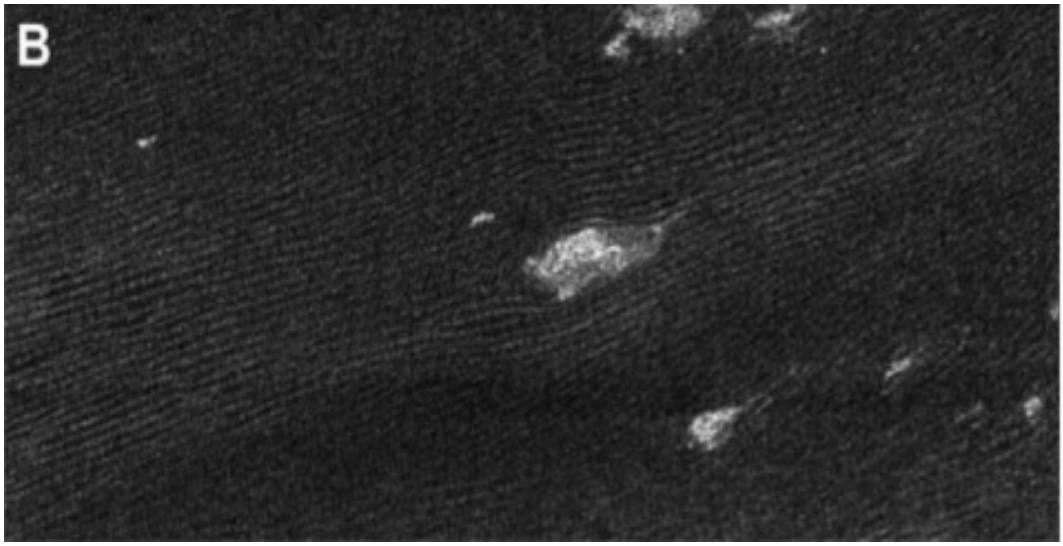

Figure 1.3: Dunes in Cassini/RADAR T8 flyby swath. The bright feature is a small hill. The linear features sometimes would merge and form 'tuning fork' junctions. Sand flow also diverges before and converges after going through the obstacle, which suggests eastward flow (Figure from Lorenz et al. 2006).

m, and the dune spacings are between 1–3 km. The interdune spacing on Titan could be controlled by the atmospheric boundary layer (Lorenz et al., 2010). The slopes of the dunes are around 6°, with a standard deviation of 2–3° (Lorenz et al., 2006; Neish et al., 2010).

On Titan, the dune and the interdune gap has a ratio of $\frac{1}{2}$, which indicates ample sand supply for the dunes similar to terrestrial linear dunes (Bagnold, 1941; Lancaster, 1982, 1995). Barnes et al., (2008) observed sand-free interdunes at the Belet sand sea with VIMS, and suggested that the dunes were active recently–since inactive dunes on Earth tend to redistribute sand by filling in the lower interdune areas through mass movement or fluvial action, making a continuous sand sea. The detection of dust storms on Titan also suggests that Titan's dune fields are currently active (Rodriguez et al., 2018).

The asymmetric pattern of the dunes indicates a west to east net transport direction (Lorenz et al., 2006). Dune orientation mapped globally reveal that the winds on Titan are probably composed of a dominant eastward component that is aligned with the dune axis plus several off-axis of seasonally alternating winds (Radebaugh et al., 2008). The local and regional deviations of dune orientation is up are 40° (Lorenz and Radebaugh, 2009).

The absence of large bodies of standing liquids in Titan's equatorial regions make it possible for the sand to transverse the equatorial circumference without getting trapped. The observation was further confirmed by global circulation models (GCMs) that the equator to pole transport of methane is very efficient, leaving the equatorial regions dry (Rannou et al., 2006; Mitchell et al., 2006, 2009; Mitchell, 2008; Schneider et al., 2012; Lora et al., 2014, 2015;

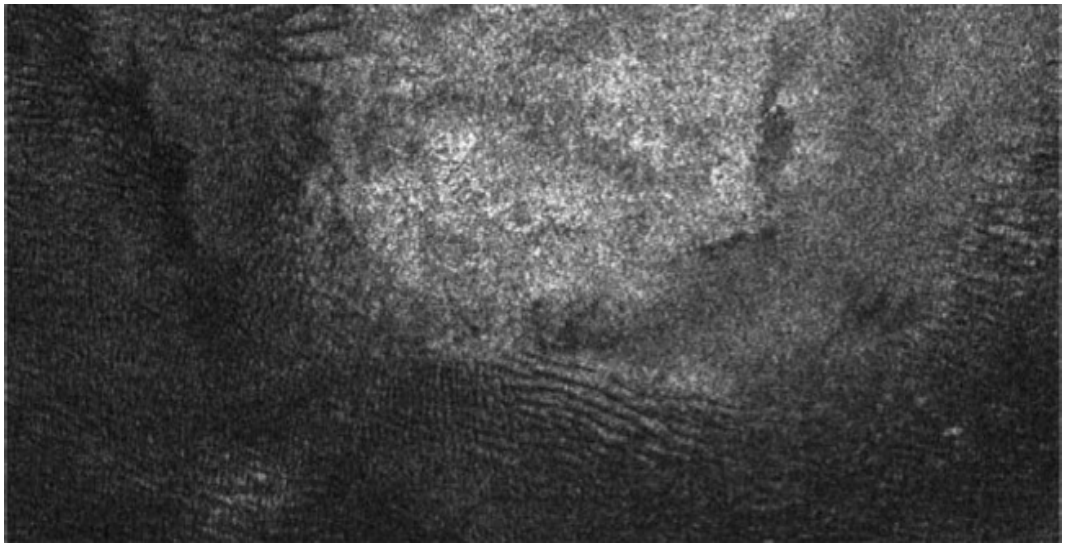

Figure 1.4: Dunes in Cassini/RADAR T8 flyby swath. Longitudinal dunes transformed into transverse dunes when running into the bright obstacle at the southwestern side (Figure from Lorenz et al. 2006).

Mitchell and Lora, 2016).

Transverse dunes, though very rare, are found on Titan when longitudinal dunes run into an obstacle (e.g. Figure 1.4). This could be caused by topographic elevation blocking the fluctuating component of the wind, leaving only the pure, unidirectional wind to form the observed transverse dunes (Lorenz et al., 2006, Radebaugh et al., 2010). Barchan dunes and star dunes (dune formed with limited sand supply) are also observed on de-speckled RADAR SAR images where the sand supply may be limited (Ewing et al., 2015), indicating the complexity of small-scale surface wind regimes on Titan.

1.1.3 Dune Distribution

Titan dunes are mostly located in the $\pm$ 30° latitude regions, with a global coverage about 10–20% of the whole surface (Figure 1.5, Radebaugh et al.

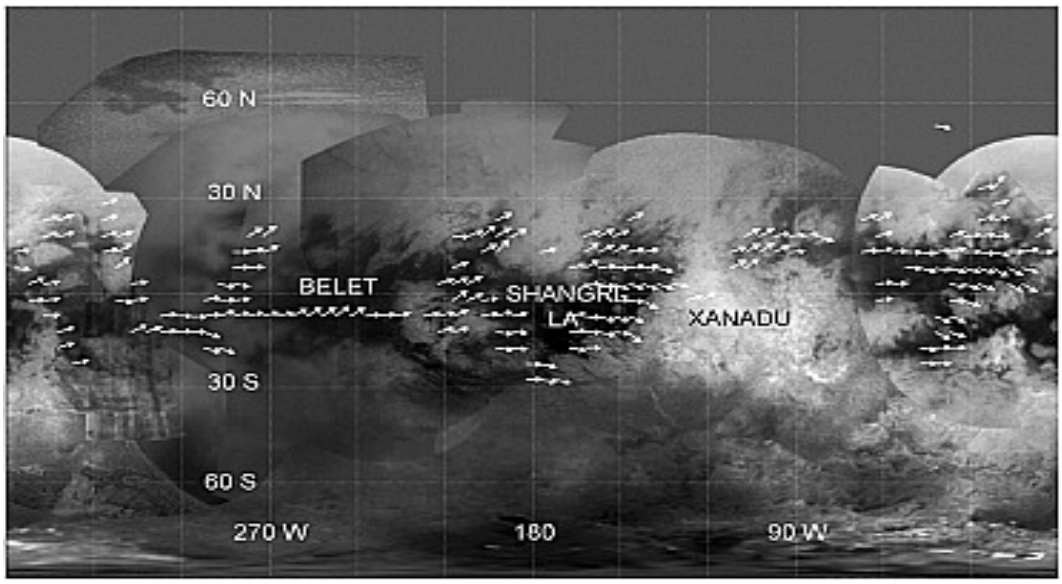

Figure 1.5: Dune distribution on Titan overlain on a Cassini ISS map. Line orientations indicate mean dune directions and arrowheads show hypothesized wind directions. (Figure from Lorenz and Radebaugh, 2009).

2008; Lorenz and Radebaugh, 2009; Le Gall et al., 2011; Rodriguez et al., 2014), corresponding to an area of $\sim$10–20 million km^2, and sand volume of 0.5–5×10^5 km^3 (Lorenz et al., 2006; Le Gall et al., 2011). Note that the sand volume on Titan is probably larger than the liquid hydrocarbon volume, which is estimated to be around 0.3×10^5 km^3 (assuming lake depth of 20 m, Lorenz et al., 2008), even though later studies found lakes that are quite deep, up to 160 m (Mastrogiuseppe et al., 2014; Le Gall et al., 2016; Hayes, 2016).

The dominant dune type on Titan is longitudinal dunes, which accounts for over 90–95% of the all dunes observed by RADAR and VIMS (Radebaugh et al., 2008). Longitudinal dunes are usually formed with ample sand supply; however, there are cases when they can also be formed from a limited sand supply. For example, longitudinal dunes can be formed by elongating one

horn of a barchan dune under low sand supply, which has been observed on Earth (Bagnold, 1941) and may exist in the higher-latitudes dune regions on Titan (>30°, up to 55°, Radebaugh et al., 2008, 2010). This implies that sand supply may be more limited with increasing latitudes on Titan.

The sand supply transition can also be supported by the interdune distribution. Le Gall et al. (2011) found the reflectivities of the interdunes are highly variable globally: some interdunes are radar bright, sand-free, and widely spaced, while some are radar-dark, and closely spaced (Figure 1.6). The interdunes in higher latitudes tend to be brighter and more widely spaced. The fraction of interdunes also increases northward, which indicate a smaller sand coverage and lower sand supply with higher latitudes. Furthermore, the undifferentiated terrains in the mid-latitudes are spectrally similar to interdunes in ISS and VIMS, and could be a result of longitudinal dunes transitioning into higher latitudes (Barnes et al., 2008; Lopes et al., 2016).

1.1.4 Winds and Dunes

Huygens Probe descended through Titan's atmosphere, landing at 192°W, 10°S in 2005. The Descent Imager and Spectral Radiometer (DISR) instrument on Huygens used optical tracking and measured the wind velocity to be ∼1 m/s eastward at 2 to 3 km altitude. Near the surface (200 to 300 m altitude), the wind is ∼0.3 m/s and the direction is west-northwest (Tomasko et al. 2005). The Huygens Doppler tracking shows a consistent wind speed of ∼1 m/s in the lowest 5 km (Bird, 2005). Higher resolution Huygens Doppler Wind Experiment (DWE) data further constrained the wind profile in the last

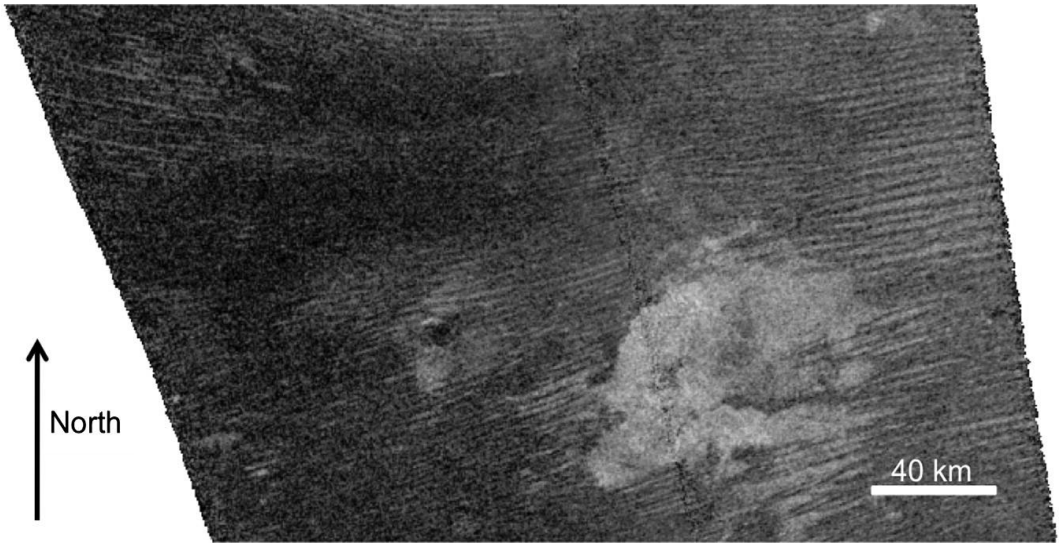

Figure 1.6: Dunes in Cassini/RADAR T49 flyby swath. Two types of dune fields can be seen in this image. Dunes are more narrowly spaced and interdunes are radar-dark in the west dune field. While dunes are widely spaced with bright interdunes in the east field. The dichotomy could be caused the topographic relief in the center of the image. (Figure from Le Gall et al., 2011)

5 km (Folkner et al., 2006), finding an eastward wind that switches direction and becomes a weak westward wind ($<$1 m/s) at about 1 km altitude.

A number of atmospheric modeling works tried to reproduce the observed dune pattern on Titan using GCMs, but failed to produce strong enough winds to saltate sand particles (e.g., Tokano, 2008; Friedson et al., 2009; Mitchell et al., 2009). The resulting mean wind direction is westward rather than eastward as indicated by the dune morphology. Note that the Huygens Probe detected weak westward wind ($\sim$1 m/s) at altitudes around 1 km, but weak eastward wind ($<$1 m/s) near the surface (Folkner et al., 2006).

Tokano (2010) used the Köln GCM and generated fast eastward winds during both of Titan's equinoxes. Lucas et al. (2014b) and Charnay et al. (2015) found that the addition of equatorial convective methane storms during Titan's

equinoxes could produce eastward winds that are strong enough to saltate sand particles on the surface. Charnay et al. (2015) also predicted the existence of dust storms on Titan similar to haboobs formed by convective clouds, which were later seen by Rodriguez et al. (2018) during Titan's northern spring equinox in 2009 and 2010. These kind of short-duration, annual-peak wind events are also found to govern terrestrial dune orientation such as the Namib sand seas (Lancaster, 1984). McDonald et al. (2016) suggests orbital forcing and topography could also be important in governing dune orientations and should be considering in future modeling.

There is also the possibility that the current dune orientations reflect Titan's past wind conditions instead of the present (Lorenz, 2014; Ewing et al., 2015; McDonald et al., 2016), since reorientation of the dunes on Titan acts on a timescale of around 10^5 years, which is controlled by Saturn's orbital forcing (Ewing et al., 2015).

Longitudinal dunes on Earth can be formed under different wind regimes: 1) one main direction (unimodal) of wind (Rubin and Hesp, 2009), 2) cross directions (bimodal) of winds with either an acute angle or an obtuse angle between the two directions (Tsoar, 1983; Rubin and Ikeda, 1990; Lancaster, 1995), or 3) complex winds (more than two modes), such as winds with one major axis and minor off-axis components (Blandford, 1877; Fryberger and Dean, 1979; Lancaster, 1995).

All the above wind regimes have been proposed for the formation of Titan dunes. Rubin and Hesp (2009) suggests that if the sediments are cohesive enough on Titan, then only unidirectional winds are needed to form the linear

dunes. Titan GCMs have predicted bimodal surface winds on Titan, which reverse seasonally towards the south-west or the north-west, with transitional periods of eastward winds near equinoxes (Tokano, 2010; Lora et al., 2015). The bimodal wind regime has also been suggested by Radebaugh et al. (2007). While the observations of different dune types (e.g., linear dunes, star dunes, barchan dunes) suggest a complex wind regime in the equatorial region of Titan (Radebaugh, 2013; Lucas et al., 2014b; Ewing et al., 2015).

In order to understand Titan's climate, it is important to know the wind regime on Titan. However, Cassini was not designed to directly measure low-altitude winds except for the few clouds that have been tracked in the lower atmosphere (Rodriguez et al., 2009, 2011; Brown et al., 2010; Turtle et al., 2011). The Huygens Probe measured winds while it was descending, but it only provides wind information at one location on Titan at one point in time (Tomasko et al., 2005). Thus, dunes remain the primary source for obtaining near-surface wind estimates on Titan. By studying sand transportation and dune formation on Titan, we could better constrain the near-surface wind speed and direction(s) and eventually better understand Titan's atmospheric circulation patterns and climate.

1.1.5 Sand Composition

Instead of silicate sand on terrestrial bodies like Venus, Earth, and Mars, Titan's dunes are likely composed of organics or organics and water ice (McCord et al., 2006; Soderblom et al., 2007; Barnes et al., 2008; Clark et al., 2010; Le Gall et al., 2011; Hirtzig et al., 2013; Rodriguez et al., 2014).

Before Cassini, candidates for Titan sand include the following: 1) weathering (can be aeolian or fluvial) products of bedrock such as water ice or ammonia water ice; 2) pristine or modified photochemically-produced solid organic aerosols from the atmosphere; 3) sand-sized material produced by impact ejecta, which could be a modified mixture of the organic aerosols and the water ice bedrock.

There are a few ways to constrain what actually the Titan dunes are made out of.

From the sand supply point of view, the extent of the sand seas on Titan requires $\sim 10^4$ to 10^5 km^3 of sand sized materials (Lorenz et al., 2006), which is considerably too high if all of the sand particles are impact originated (Lorenz et al., 1995). While photochemistry could produce up to $\sim 10^6$ to 10^7 km^3 of organics over the history of the Solar System (4.5 Gyrs, Yung et al., 1984), only 1% of those need to be solid to form the dunes on Titan. Thus the impact origin of Titan's sand could be ruled out from this point of view. Erosion by the river channels can also be eliminated for a similar reason (Lorenz et al., 2008).

The various modes of Cassini RADAR include SAR, scatterometry, and radiometry, contain physical and electrical properties of the dune materials. Microwave radiometry shows that the surface temperature of the dunes is 3 to 5 K above the average surroundings, suggesting high emissivity (low dielectric constant material and little volume scattering). The scattometry data suggests that the surface of the dunes is smooth (at the wavelength scale of the radar instrument, 2.2 cm), homogenous, and compacted (Elachi et al., 2006;

Janssen et al., 2009; Le Gall et al., 2011). Thus the dunes should be composed of fine grained materials, and based on the possible sources on Titan, the material could be either organic solids, water ice, or a combination of the two.

The dielectric constant (or relative permittivity ϵ) of the dune materials obtained by RADAR is around 1.5 to 2.5 (Elachi et al., 2005; Paganelli et al., 2007, 2008; Janssen et al., 2009), which is closer to solid hydrocarbons ($\epsilon \sim$1.7–2.5, Paillou et al., 2008) than water ice ($\epsilon\sim$3) or ammonia ice ($\epsilon\sim$4.5). If just considering closely-spaced dune regions with dark interdunes, then the dielectric constant can be further constrained to 1.7 ± 0.5 (Le Gall et al., 2011). This would correspond to an organic-dominated composition with a 20–30% porosity, or a water-ice dominated composition with 65% porosity. The latter is beyond the dune porosity observed on any dunes on Earth (Pye and Tsoar, 2009).

Dunes appear to be dark features not only in radar, but also in ISS (Porco et al., 2005) and VIMS images (Soderblom et al., 2007). The ISS instrument on Cassini images Titan mainly in and near the visible range from 200 to 1100 nm. The VIMS instrument can image Titan's surface at several infrared wavelength ranges that are centered at 0.94, 1.08, 1.27, 1.59, 2.01, 2.69, and 5.00 μm, where Titan's atmosphere is transparent (Brown et al., 2004). VIMS and ISS can only probe the top tens of microns of the surface, and are mainly sensitive to composition and grain size. Dune fields in the RADAR/SAR data are highly correlated with the VIMS "dark brown" spectral units (Figure 1.7, Soderblom et al., 2007, Rodriguez et al., 2014), suggesting that the dunes are mainly composed of complex organics, at least on the top tens of microns of

the surface (Barnes et al., 2007, 2008; Clark et al., 2010; Hirtzig et al., 2013; Solomonidou et al., 2018). Dune fields can occasionally overlap with the “dark blue" unit (Figure 1.7, Soderblom et al., 2007), which is thought be either an enrichment in water ice (Rodriguez et al., 2006) of the dune materials, or the increasing amount of bright interdunes in these particular dunefields (Barnes et al., 2008).

The Titan aerosol analog, so called “tholin", is the solid products of electron discharge and/or photolysis synthesized in terrestrial laboratories with common gases in Titan’s atmosphere such as nitrogen and methane (Sagan and Khare, 1979; Cable et al., 2012). Tholins are a mixture of chemical compounds and are considered to be laboratory produced analogs of Titan’s atmospheric haze, which eventually sediments to the surface. However, the dune materials do not completely match the spectra of laboratory produced tholins; they seem to consist of mainly a much darker material with very low albedo (Soderblom et al., 2007; Hirtzig et al., 2013; Solomonidou et al., 2018). Thus either some sort of chemical or mechanical processes are turning the brighter aerosol grains into the dark saltating sand particles, or the dark dune materials are derived from a different type of photochemically produced materials (Soderblom et al., 2007).

1.1.6 Sand Size

Neither the RADAR nor the VIMS instrument of Cassini can resolve individual sand grains. Thus the current sand size of dunes on Titan is estimated based on the optimum particle size for saltation, which is the particle size where

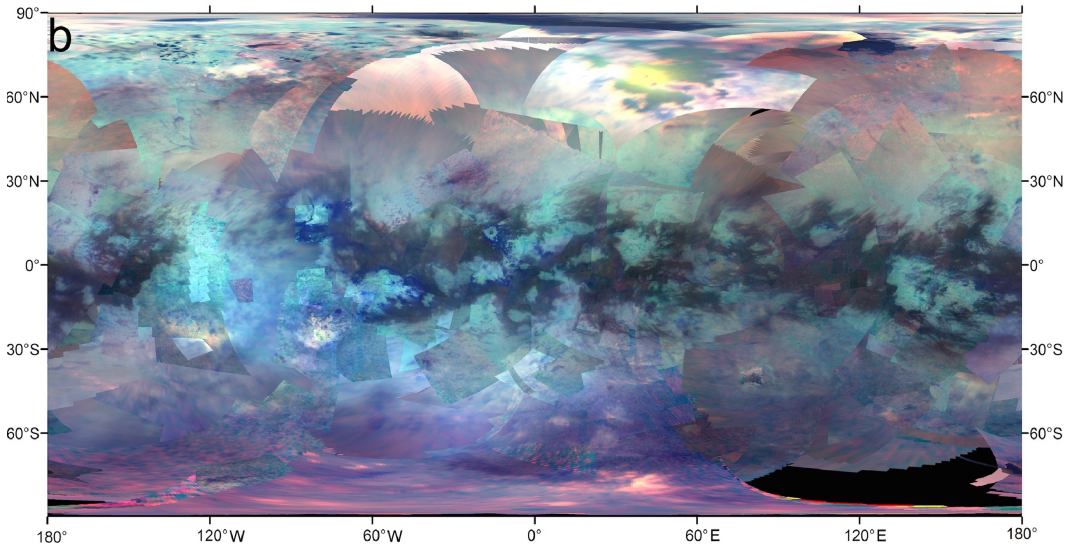

Figure 1.7: The complete VIMS RGB global map with red, green, and blue controlled by the 5.0, 2.0, and 1.28 μm channels (Figure from Le Mouélic et al., 2019). The majority of the dunes appear to be “dark brown", while water ice is “bright blue".

the minimum wind speed is needed to saltate sand particles. Lorenz et al. (1995) estimated the optimum sand size on Titan based on the semi-empirical expressions for threshold wind speed (assuming the same cohesion parameter as Earth sand) of Greeley and Iversen (1985). They found that the optimum sand size on Titan (100–300 μm) is about twice as large as the rest of the terrestrial planets (50–110 μm), because of a combination of lower particle density and gravity on Titan.

Lorenz (2014) suggests that a decreased particle density or increased cohesion between particles could lead to a greater optimum diameter for Titan sand, up to 500–600 μm. Burr et al. (2015) modified the threshold friction speed function using experimental results from the Titan Wind Tunnel and they found an optimum diameter around 200–300 μm.

1.1.7 Sand Formation

The formation of the dune particles on Titan is still a mystery. The observed organic aerosol particles are only about 1 μm in size, while the dune particles are at least 100 μm. The volume of one sand particle is 6 orders of magnitude larger than one aerosol particle, which requires 1 million haze particles to produce one single sand particle. Barnes et al. (2015) proposed four mechanisms for the transformation: sintering, lithification and erosion, flocculation, and evaporation. Each mechanism will lead to a difference in the final sand properties. If the sand particles are produced by sintering, then the composition of the sand particles would match the aerosols. If the sand particles are produced by flocculation or evaporation, the composition of the sand would be similar to either the insoluble or the soluble part of the aerosols in Titan's lakes, respectively.

1.1.8 Comparative Aeolian Processes

Sands and dunes have been studied since Bagnold (1941) on the Earth. Later on aeolian processes were discovered on Mars (Malin & Edgett 2001), Venus (Weitz et al. 1994), Titan (Lorenz et al., 2006), Neptune's moon Triton (Smith et al., 1989), Pluto (Telfer et al., 2018), and possibly Comet 67P/Churyumov-Gerasimenko (Thomas et al., 2015). Even though all these planetary bodies have very diverse gravity, atmospheric density, transporting materials, and circulation patterns, the resultant landforms are inherently similar. The existence of aeolian landforms implies that the surface must have 1) a sufficient supply of sand; 2) winds of sufficient velocity to move the sand; and 3) winds

that blow long enough for bedforms to form and evolve (Diniega et al., 2017). Greeley and Iversen (1985) first compared the geological wind processes on Earth, Mars, Venus, and Titan and they concluded that aeolian processes could happen all the four planetary bodies.

Titan's dunes are formed in a dense atmosphere with lower gravity and lower temperature than the terrestrial planets, and dune particles are probably composed of organics/water ice rather than silicate or basalt rock as on terrestrial planets. Table 1.1 summarizes the environmental conditions and transporting materials on planetary bodies with possible aeolian features. Aeolian bedforms on other planetary bodies enable us to test Earth-based physical models against a range of environmental and planetary conditions, from near vacuum on Comet 67P to 92 bar on Venus, from negligible gravity on Comet 67P/ChuryumovâĂŞGerasimenko to Earth like gravity, from extreme coldness on icy bodies such as Pluto, Triton, and Comet 67P to blistering hot on Venus. By understanding how these different environmental and material parameters contribute to the physics of aeolian landform formation, a more general and a more rigoriously physics-based model of aeolian transport can be constructed, relative to what is often only empirical in current models. We can also have more information about the surfaces of these planetary bodies, such as near surface circulation, material formation and transportation, and even habitability. Figure 1.8 shows the threshold wind speed predicted for these different planetary bodies with Earth-based models (Pähtz and Durán, 2016).

Data obtained by Cassini-Huygens show that the dunes are mainly found

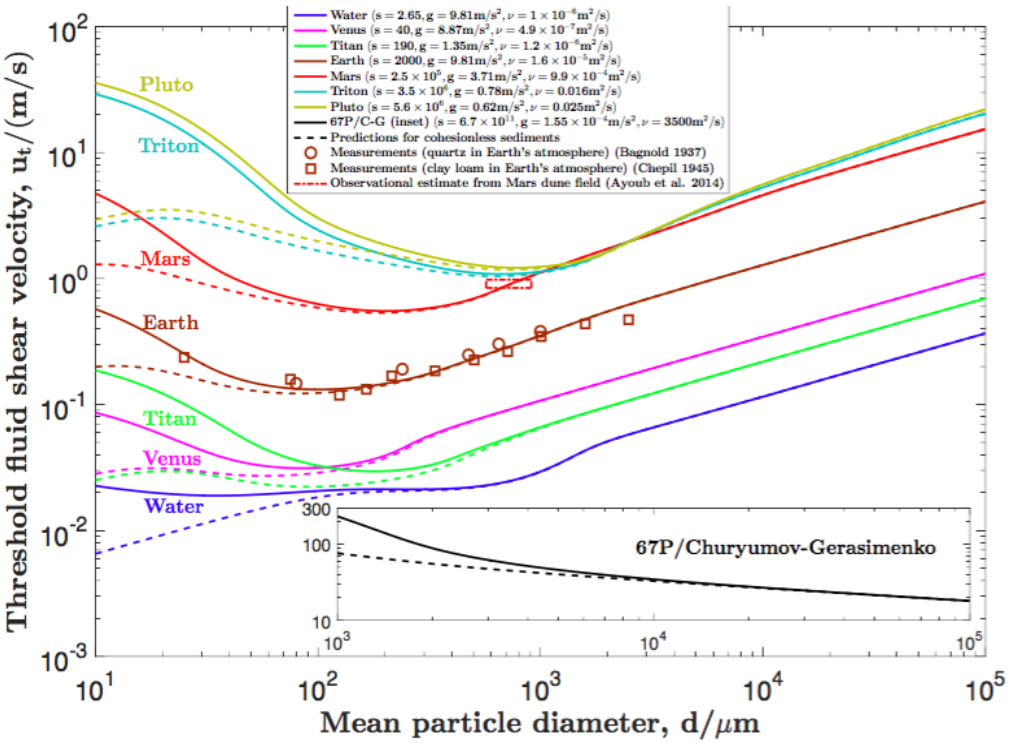

Figure 1.8: The fluid threshold wind speed in various planetary environments for cohesive sediments (solid lines) and cohesion-free sediments (dashed lines). The symbols resemble measurements in Earth's atmosphere and observation estimate on Mars (Figure from Pähtz and Durán, 2016).

Planetary Body	Gravity (m/s^2)	Density of Material ρ_p (kg/m^3)	Atmospheric Density ρ_a (kg/m^3)	Atmospheric Viscosity (Pa·s)	Surface Temp. (K)	Surface Pressure (bar)
Venus	8.9	3000 basalt	65	3.27×10^{-2}	735	92
Earth	9.8	2650 quartz	1.2	1.85×10^{-5}	300	1
Mars	3.7	3000 basalt	0.015	1.30×10^{-5}	227	0.0061
Titan	1.4	500–1400 organics	5.1	6.25×10^{-6}	94	1.5
Triton	0.78	500–1400 organics	$\sim 9 \times 10^{-5}$	$\sim 2 \times 10^{-6}$	35	variable
Pluto	0.62	900 methane ice	$\sim 9 \times 10^{-5}$	$\sim 2 \times 10^{-6}$	44	variable
Comet 67P	5×10^{-4}	950 water ice?	variable	variable	variable	near vacuum

Table 1.1: Environmental conditions for planetary bodies with possible aeolian features.

within $\pm 30^\circ$ latitudes and cover 10–20% of the entire surface, exceeding dune coverage on Earth (4%, Lancaster, 1995; Bourke et al., 2010), Mars (0.06%, Fenton and Hayward, 2010), and Venus (0.004%, Bourke et al., 2010). On Earth, longitudinal dunes comprise 50–70% of the total dunes (Bagnold, 1941; Lancaster, 1982; Lancaster, 1995). On Mars, longitudinal dunes are rare (e.g., Lee and Thomas, 1995; Edgett et al., 2000), while Titan's dunes are almost solely longitudinal dunes (>95%).

1.2 Dune Formation Theory

1.2.1 Saltation

The movement of sand and dust can be divided into different modes based on the particle size and wind speed (Figure 1.9). Small particles like dust (<70–80 μm) are hard to lift through direct wind shear because the interparticle

cohesion between small particles is larger than the exerted aerodynamic lift and drag forces. However, once they are perturbed or mobilized by other particles and are lifted off the surface, they are more susceptible to atmospheric turbulence. Because of their small terminal velocity, small particles will tend to enter into the “suspension" mode (short term for 20–70 μm particles or long term for $<$20 μm particles).

When the wind stress increases enough to lift sand-sized particles (typically several hundreds of μm) from a loose sand surface, the uplifted particles will go through a *saltation* process (in latin *'saltare'* means leap or spring, Bagnold, 1941): particles will follow a ballistic trajectory and hop along the surface to eject new saltating particles into the fluid, while the original particles will hop several times at the surface, which is called ‘reptation’ (Anderson, 1987; Andreotti, 2004). The initiated particles usually hit nearly parallel to the surface, but the newly saltated particles will rebound at 40°, thus this saltation process efficiently transforms or transports horizontal momentum from fluid drag to vertical momentum. The number of newly saltated particles will grow exponentially (Durán et al., 2011) and slow fluid speed (Bagnold, 1936). The reduced fluid speed then reduces the concentration of particles (Owen, 1964) until finally a steady-state saltation process is achieved.

The large sand particles (typically $>$500 μm) are hard to mobilize by wind because of their large mass. However, they can be perturbed by the saltating particles and enter the “reptation" or the “creep" mode. Here I will focus on the sand-sized particles between 70 μm and 500 μm in the saltation mode, because they are the main dune-forming materials and saltation is the main

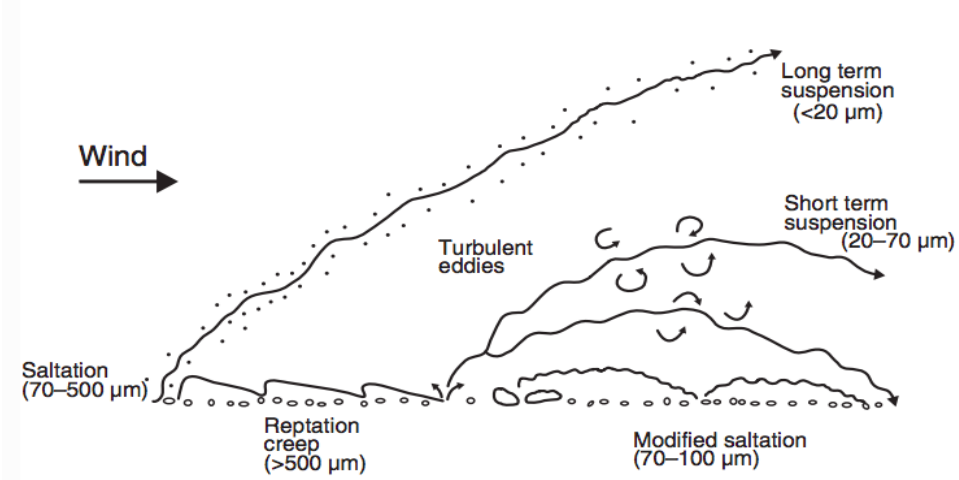

Figure 1.9: Different modes of aeolian transport (Figure from Nickling and McKenna Neuman 2009).

process governing large aeolian bedforms.

Two different threshold speeds govern the saltation process. The first is called fluid or static threshold, which governs the initiation of saltation. It is the lowest wind speed required to lift the particles from the surface. The other one is called the impact threshold, which is the minimum speed required to maintain the saltation process. On Earth and Mars, the impact thresholds are 0.8 and 0.1 of the fluid threshold (Bagnold, 1937; Kok, 2010), respectively, since the transfer of momentum to the sand surface is more efficient than direct fluid drag. While on Venus and Titan, the ratio of atmospheric density over particle density is much larger than on Earth or Mars, making the impact to fluid threshold ratio greater than 1 (Kok et al., 2012). Thus fluid drag maintains saltation on Venus and Titan.

The fluid threshold can be derived from the force balance on a stable surface particle sitting on two other particles. When the moments of the

aerodynamic drag force (F_d) and the fluid lift force (F_l) exceed the moments of the gravitational force (F_g) and the interparticle force (F_i) (Greeley and Iversen, 1985, Shao and Lu, 2000), the surface particle can be lifted by the flow with a threshold wind speed u_{*ft}. The moment balance can be written as:

$$r_d F_d \approx r_g(F_g - F_l) + r_i F_i, \tag{1.1}$$

where r_d, r_g and r_i are proportional to particle diameter (D_p), see Figure 1.10. The effective gravitational force including buoyancy can be expressed as:

$$F_g = \frac{\pi}{6}(\rho_p - \rho_a) g {D_p}^3, \tag{1.2}$$

where g is the gravitational acceleration, ρ_p and ρ_a are respectively the material and fluid density. The aerodynamic drag force is given by:

$$F_d = K_d \rho_a {D_p}^2 {u_*}^2, \tag{1.3}$$

where K_d is a dimensionless coefficient that is a function of the particle's friction Reynolds number (Re_*), where,

$$R_* = \rho_a u_* D_p / \mu,$$

and μ is the dynamic viscosity and $\nu = \mu/\rho$ is the kinematic viscosity.

Combing Equations 1.1-1.3, the fluid threshold can be derived as:

$$u_{*ft} = A_{ft} \sqrt{\frac{\rho_p - \rho_a}{\rho_a} g D_p} \tag{1.4}$$

where A_{ft} is a function of fluid drag force, and is usually taken to be $\sim$0.10 (Bagnold, 1941). A_{ft} is a function of interparticle forces and the Reynolds

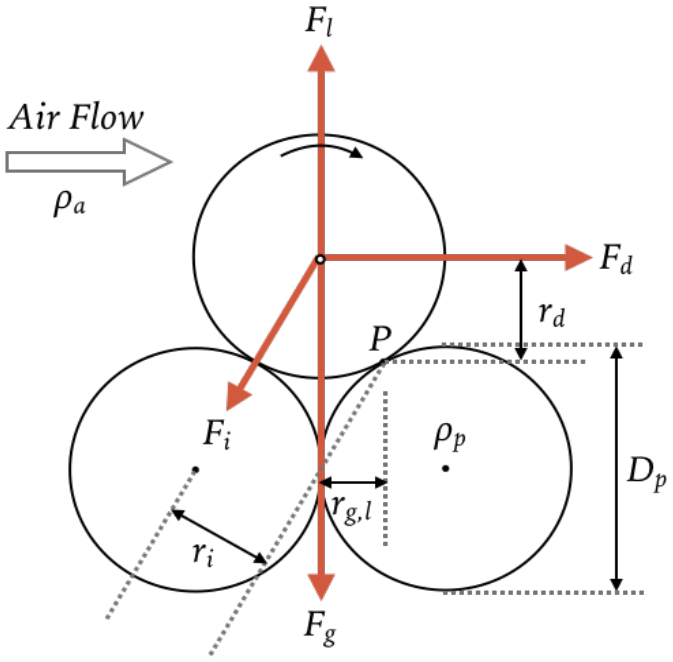

Figure 1.10: Forces acting on a stable particle resting on other two particles (Adapted from Shao and Lu, 2000), including the aerodynamic drag force (F_d), the fluid lift force (F_l), the gravitational force (F_g), and the interparticle force (F_i). The associated moment arm lengths (r_d, r_g and r_i) are marked.

number of the fluid (Bagnold, 1941; Shao and Lu, 2000).

In the following section, other semi-empirical expressions of fluid threshold will be illustrated and compared. The equations will be discussed in terms of various parameters that contribute to the final values, including particle size and density, and the various interparticle forces such as van der Waals forces and electrostatic forces.

1.2.2 Semi-empirical Equations for Fluid Threshold

Combining wind tunnel data and Equation 1.4, and accounting for the lift force and the interparticle forces, Iversen and White (1982) presented a set of

equations for A_{ft} in terms of different Reynolds number regimes (R_{*t}):

$$A_{ft} = 0.2\sqrt{\frac{(1 + 0.006/\rho_p g {D_p}^{2.5})}{1 + 2.5R_{*t}}}, 0.03 \leq R_{*t} \leq 0.3,$$

$$A_{ft} = 0.129\sqrt{\frac{(1 + 0.006/\rho_p g {D_p}^{2.5})}{1.928{R_{*t}}^{0.092} - 1}}, 0.3 \leq R_{*t} \leq 10, \tag{1.5}$$

$$A_{ft} = 0.120\sqrt{1 + 0.006/\rho_p g {D_p}^{2.5}}(1 - 0.0858e^{-0.0671(R_{*t}-10)}), 0.3 \leq R_{*t} \leq 10,$$

where

$$R_{*t} = \rho_a u_{*ft} D_p / \mu.$$

Shao and Lu (2000) simplified the above equations by scaling the interparticle forces with particle diameter, and the fluid threshold can be expressed as:

$$u_{*ft} = A_N\sqrt{\frac{\rho_p - \rho_a}{\rho_a} g D_p + \frac{\gamma}{\rho_a D_p}} \tag{1.6}$$

where $A_N = 0.111$, close to the value in Equation 1.4. The parameter γ scales with the magnitude of the interparticle forces, and can vary from 1.65×10^{-4} N·m^{-1} to 5.00×10^{-4} N·m^{-1} for typical terrestrial sand.

Burr et al. (2015) compared Titan wind tunnel data to both the Iversen and White (1982) and Shao and Lu (2000) fluid threshold models. They found that the threshold wind speed derived from the models underestimated the threshold wind speed derived from the TWT by 40%-50%. They thus proposed that, for Titan conditions, a density ratio term $\delta(\rho_p/\rho)$ should be considered in both models:

$$u_{*ft} = A_1\sqrt{(\frac{1 + A_4 I_p/\rho_p g {D_p}^3}{f({Re_t}^* + \delta(\rho_p/\rho)})\frac{\rho_p g D_p}{\rho}}. \tag{1.7}$$

This new equation also fits the Venus wind tunnel data, and they conclude that a density ratio term has to be considered if the atmospheric density cannot be ignored compared to the material density (Marshall and Greeley, 1992; Burr et al., 2015).

1.2.3 Particle Size and Density

The fluid threshold speed and optimum particle size (size with the lowest threshold speed) based on a variety of models and particle densities are listed in Table 1.2. The modified Iversen and White (1982) and Shao and Lu (2000) models with the density ratio term proposed by Burr et al., (2015) are also listed.

Simple nitriles and organics have densities that range from 700–900 kg/m^3 (Raulin, 1987), while PAHs (polycyclic aromatic hydrocarbons) have densities about 1150–1270 kg/m^3 (Sagan et al., 1993). The densities were measured at room temperature, but the materials only contract 1–2% at 90 K, leading to only 5% increase in density (Lorenz et al., 2014). Thus the estimated Titan particle density usually has a range from 400–1500 kg/m^3. The lower limit is the particle density when porosity is included, because in Earth simulated experiments, the produced tholin particles are usually porous (Carrasco et al., 2012) and it is consistent with theoretical analysis of the porosity of Titan's surface materials (Mousis and Schmitt, 2008). Recent laboratory experiments show that the Titan tholins have an density range of around 500?1400 kg/m^3 (Hörst and Tolbert, 2014; Imanaka et al., 2012; He et al., 2017).

Figure 1.11 shows that a change in particle density does not significantly

Model	particle size (μm)	friction speed (m/s)	ρ_p (kg/m^3)
Greeley and Iversen (1985)	180	0.04	1900
Lorenz et al. (1995)	250	0.04	1000
Kok et al. (2012)	250	0.04	1000
Modified I-W with density ratio	206	0.053	1000
Modified S-L with density ratio	272	0.053	1000

Table 1.2: Friction speed using different particle density and the derived optimum particle size.

change the threshold wind speed profile. The two threshold wind speed curves for materials with particle densities of 500 and 1000 kg/m^3 do not start diverging from each other until particle size reaches about 100 μm. There is also a shift towards higher optimum particle size ($\sim$500–600 μm) for the lower density case.

1.3 Interparticle forces

A change in interparticle forces will lead to noticeable changes in the threshold wind speed curve, as shown in Figure 1.11. By using the two limits of interparticle force parameter γ in Equation 1.6 (1.65×10^{-4} N·m^{-1} and 5.00×10^{-4} N·m^{-1}), the two curves deviate from each other significantly for particles smaller than 1000 μm. An accurate characterization of the interparticle forces will greatly enhance the threshold wind speed models, especially if the sediments are different from typical Earth silicate sand.

Typical interparticle forces acting between sand and dust particles include van der Waals forces, capillary forces, and electrostatic forces. In general, all the above forces are attractive between the same material, so sometimes these forces are collectively called cohesion, which includes all the attractive forces

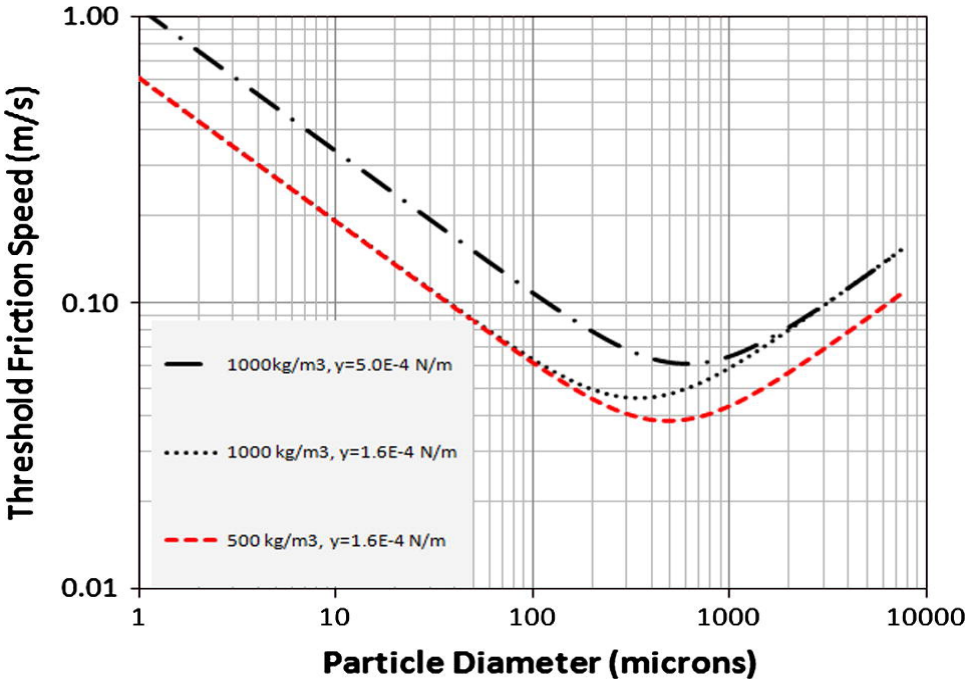

Figure 1.11: Comparison of saltation threshold on Titan with the material density ρ_p and cohesion coefficient changed (From from Lorenz et al., 2014).

between the same material. However, between two different materials, not all interparticle forces are attractive. For example, van der Waals forces can be negative between two foreign molecules. But only the attractive part of the interparticle forces are called adhesion, which includes all the attractive forces between two different materials.

1.3.1 Van der Waals Forces

Van der Waals forces are defined as the sum of the attractive or repulsive forces between neutral atoms and molecules, excluding forces between covalent bonds, ionic bonds, or charged molecules. The van der Waals forces are electrostatic in nature and arise from the interaction of permanent or transient electric dipoles. A dipole in an atom or molecule results in a separation

between negative and positive charges, and it can be described by a dipole moment (**p**):

$$\mathbf{p} = q\mathbf{d}, \tag{1.8}$$

where q is the electronic charge, **d** is the displacement vector pointing from the negative charge to the positive charge. The dipole moment has a unit of Debye (D), and 1 D = 3.336 $\times$ 10^{-30} C·m, which corresponds to two unit charges separated by $\sim$0.02 nm.

The van der Waals forces can be subdivided into three main types: 1) force between two permanent dipoles (Keesom force); 2) force between a permanent dipole and a corresponding induced dipole (Debye force); 3) force between two instantaneously induced dipoles (London dispersion force, London, 1937).

The Lennard-Jones (L-J) potential (Lennard-Jones, 1931) is often used to model van der Waals forces as a function of distance between two atoms or molecules:

$$U(r) = -A/r^6 + B/r^{12}, \tag{1.9}$$

where A and B are two constants and r is the distance between the atoms or the molecules. The van der Waals potential energy of attraction grows as the inverse distance to the sixth power and the repulsion grows as the 12^{th} power. The van der Waals force function F(r) is related to the potential energy by F(r)=$-$dU(r)/dr. Typical van der Waals potential energy and force function curves between two atoms are shown in Figure 1.12.

For macroscopic objects like sand and dust, Equation 1.9 does not apply because a sand or dust particle is not a single atom or molecule. However, the interaction potential may be mathematically integrated to derive a force

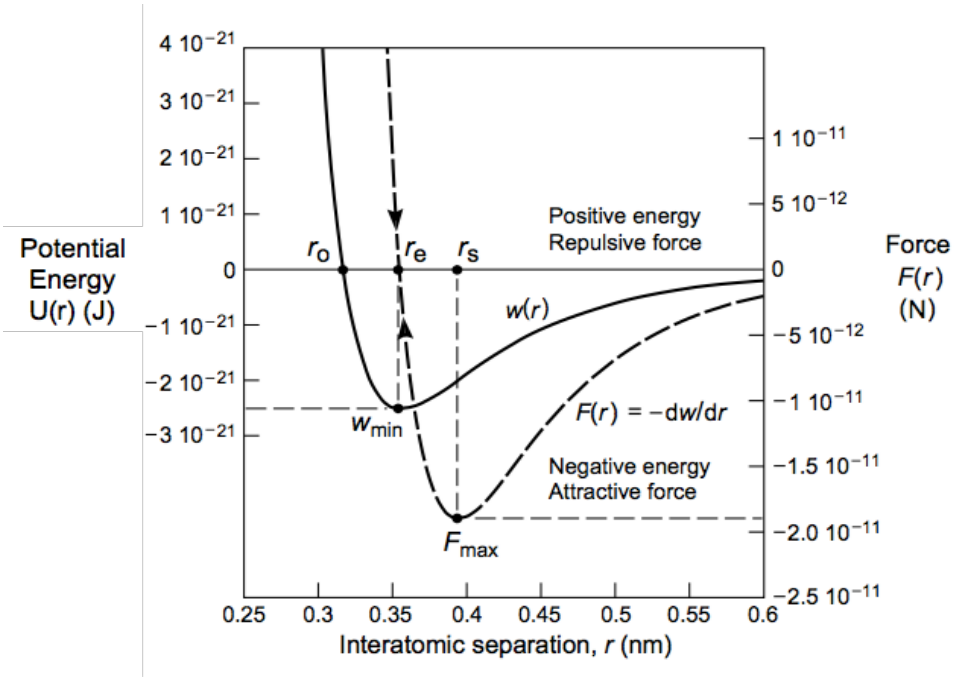

Figure 1.12: L-J potential energy U(r) for typical van der Waals forces and the resulting force function F(r) between two atoms ($A=10^{-77}$ J·m^6 and $B=10^{-134}$ J·m^{12} in Equation 1.9, Figure from Israelachvili, 2011). The separation r_e is called the equilibrium separation, where the potential energy is minimum and the force is zero, r_s is the maximum pull-off force between the two atoms, and r_0 is where potential energy is zero.

function for macroscopic objects. The net integrated force function between a sphere of radius R and a flat surface with distance D is:

$$F(D) = -\pi^2 A\rho^2 R/6D^2 = -\frac{A_H R}{6D^2}, \tag{1.10}$$

where A is the constant in Equation 1.9, ρ is the number density of atoms in the macroscopic particle, and A_H is known as the Hamaker constant (Hamaker, 1937). The Hamaker constant is material dependent and is found to be between $\sim 10^{-19}$–10^{-20} J for most materials (Israelachvili, 2011).

A more sophisticated model that further includes the many-body interactions between the dipoles is called the Liftshitz theory, and the resulting Hamaker constant becomes a complex function related to the complex dielectric function of the particles and the media in between (Liftshitz, 1956).

Another way to write Equation 1.10 between a sphere (radius R) and a flat surface is by using the Derjaguin approximation (Derjaguin, 1934):

$$F(D) = 2\pi R U(D), \tag{1.11}$$

where U(D) is the interaction energy function. The above equation applies when separation distance D between the sphere and the surface is much less than the radius of the sphere R. When the two surfaces are in contact (D=σ), the interaction energy U(σ) can be associated with the surface energy (γ) of the material:

$$U(\sigma) = -2\gamma.$$

The Derjaguin approximation at D=σ thus becomes:

$$F(\sigma) = F_{ad} = -4\pi R\gamma, \tag{1.12}$$

which gives the adhesion force F_{ad} between the two spheres in terms of their surface energy γ. The Derjaguin approximation (which is part of the so-called DMT model by Derjaguin, Muller, and Toporov, 1975) is helpful because it converts mechanical force measurements (adhesion forces) into thermodynamic properties such as interfacial energies and surface energies.

Equation 1.12, from the DMT model, assumes that the two contacting macroscopic objects are both rigid, while real particles are usually not completely rigid and would deform elastically upon contact. The contacting mechanics between elastic surfaces was first described by Johnson, Kendall and Roberts (1971), also called the JKR model. The JKR model gives the adhesion force between a sphere with radius R and a flat surface as:

$$F_{ad} = -3\pi R\gamma. \tag{1.13}$$

The JKR and DMT models are both extreme cases within a spectrum of parameter space that spans from small, rigid materials (for DMT) to big and soft materials (for JKR). Thus a dimensionless parameter called the elasticity parameter (λ) was later developed to help determine which model to use (Giri et al., 2001):

$$\lambda = \frac{2.06}{\xi_0}\left(\frac{R\gamma^2}{\pi K}\right)^{1/3}, \tag{1.14}$$

where ξ_0 is the equilibrium interatomic distance and is set to be 0.16 nm. K is the reduced elastic modulus and is related to the elastic moduli (E_1 and E_2)

and Poisson's ratios (ν_1 and ν_2) for the two contacting materials by:

$$\frac{1}{K} = \frac{3}{4}[\frac{1-\nu_1^2}{E_1} + \frac{1-\nu_2^2}{E_2}].$$

The JKR model is most appropriate when λ >5, while the DMT model applies when λ <0.1. For 0.1< λ <5, an intermediate model that incorporates long-range and short-range interactions in both JKR and DMT models, called the Maugis-Dugdale model (Maugis, 1992) can be used.

1.3.2 Capillary Forces

In a humid atmosphere, vapor could condense onto the surface of materials, forming a capillary meniscus between two contacting surfaces. On Earth, the vapor is water, while on Titan, the vapors are mainly hydrocarbons like methane. The capillary meniscus will typically pull the two contacting surfaces together, producing stronger adhesion compared to dry conditions where only solid-solid van der Waals attractive forces dominate.

Capillary forces between a sphere with radius R and a flat surface at contact is given by:

$$F_{ad} = 4\pi R\gamma_L cos\theta. \tag{1.15}$$

Note that the above equation for capillary forces does not vary with humidity, Fisher & Israelachvili (1981) and Christenson (1988) verified that once a molecular layer of liquid is present on the contacting surfaces, Equation 1.15 holds for capillary forces.

1.3.3 Electrostatic Forces

Electrostatic forces may arise by moving granular particles through contact and frictional charging (tribocharging). Most natural sand and dust are insulators that do not contain free charge carriers, but triboelectric charging can happen between those inert and chemically identical particles with the same contact potential (Lowell and Truscott, 1986; Kok and Lacks, 2009). Blowing sand and dust can also induce electric fields (Schimidt et al., 1998; Merrison, 2012; Merrison et al., 2012). Electrostatic forces can reduce the saltation threshold and promote sand transportation (Rasmussen et al., 2009). This effect is more prominent on Titan than on Earth and Mars due to the low gravity. Meanwhile, macroscopic electric fields will make the saltation threshold higher (von Holstein-Rathlou et al., 2012). The charging of particles is strongest for conditions with low humidity. Merrison (2012) measured a 50 μC/kg charge rate for snow and Dragan et al. (2011) found a 15 μC/kg charge for acrylic granules.

Once particles become charged, they can maintain that charge for a long time on Titan because of the high resistivity of hydrocarbon vapors on Titan's surface (Lorenz et al., 2014). Thus particle charging and the resulting charging effect on aggregation of particles could be more important on Titan than on Earth. Harper et al. (2017) performed tribocharging on a few Earth and Titan sand analogs and they found a higher maximum mass-to-charge ratio for Titan than Earth, which indicates electrostatic forces could potentially promote aggregation of particles and increase the saltation threshold on Titan.

1.3.4 Real Cohesion and Adhesion

The actual magnitude of cohesion and adhesion between large particles is often overestimated by adhesion theories such as JKR and DMT (for dry contacts) and liquid bridge theory for capillary forces (for wet contacts). The discrepancy was attributed to various imperfections of actual surfaces–the existence of micro-asperities (small-scale roughness) and deviations from theoretical geometry could decrease the actual cohesion/adhesion by orders of magnitude (Schaeffer et al., 1995; Persson, 2000). For dry contacts, the actual cohesion/adhesion is almost always below the JKR and DMT predictions. While the capillary forces can reach their theoretical magnitude only when the thickness of the adsorbed liquid films approach the average size of the asperities (Jones et al., 2002; Butt, 2008).

So far, there is no general mathematical treatment that can incorporate the full spectrum of roughness into adhesion models. Even though a few experimental and modeling results suggest that adhesion force would decrease exponentially with root-mean-square (RMS) roughness σ (Benz et al., 2006; Yang et al., 2008; Parson et al., 2014):

$$F_{ad}(\sigma) = F_{ad}(0)e^{-\sigma/\sigma_0}, \tag{1.16}$$

$F_{ad}(0)$ is the adhesion between smooth surfaces (where σ=0).

1.4 Outstanding Questions for Titan Dunes

With the help of Cassini's observational data of Titan, the geomorphology and spatial extent Titan's dunes have been investigated, placing constraints on sand properties and wind regimes. Recent Titan Wind Tunnel (TWT) experiments simulated Titan's atmospheric environment on Earth (by achieving the same kinematic viscosity as Titan) and found a higher than terrestrial model predicted threshold wind speed (Burr et al., 2015). However, the formation and composition of Titan sand remains unknown. Furthermore, interparticle forces like cohesion forces and electrostatic forces and other material properties are not constrained in the TWT experiments. Thus my goal is to study the following questions:

- How is dune formation affected by different environmental conditions and transporting material properties on Titan compared to Earth?
- How does the organic sand on Titan behave compared to silicate sand on terrestrial bodies (Earth, Venus and Mars) in terms of its material properties (density, interparticle forces including cohesion and electrostatic forces, and mechanical properties)?
- What is the origin and evolution of the organic sand particles on Titan?

In Chapter 2, I studied the effect of adsorbed liquid on threshold wind speed for the materials used in the TWT, and possibly for organics on Titan. The materials used in the TWT experiments were exposed to the ambient atmosphere during the setup of the test bed and can result in water adsorption

onto the particles. Through gravimetric analysis, I found that the commonly used low density wind tunnel materials, like walnut shells, adsorb >6% of water by weight % at equilibrium, while quartz sand adsorbs <1% of water. However, even with this high water content (w), the measured fluid thresholds with 'dry' (w_{dry}=1.72%) and 'wet' (w_{wet}=7.2%) walnut shells in the TWT are less than 5% different. This suggests humidity has negligible effect on fluid thresholds for low density materials with water content w<7.2%. I found that determination of water content can provide insight into the sensitivity of threshold wind speed to relative humidity for a given material. This could be applied for organic sand on Titan, where methane is the dominant vapor. Laboratory studies show that tholin (produced in a different lab) can at most adsorb 0.3% methane by mass (Curtis et al., 2008). Thus I suggested that the effect of methane vapor on the threshold wind speed of Titan's organic sand could be similar to that of water vapor on quartz sand. With increasing methane RH, the threshold wind speed for Titan's organic sand will increase accordingly. Finally, using environmental parameters for Titan and properties of methane, I modeled the effect of methane relative humidity on threshold wind speed on Titan. This work was published in *Icarus* as Yu et al., (2017a).

In Chapter 3, I measured the surface energy and interparticle cohesion forces between Titan aerosol analogs (tholin). The terrestrial threshold wind speed models (e.g. Shao and Lu, 2000) suggest that interparticle force is highly dependent on material properties and is a crucial parameter in determining threshold wind speed. On Titan, the sand composition is completely different from Earth's sand, and the interparticle forces between Titan organic sand

analogs have never been characterized before. In the TWT, low density materials with unknown interparticle forces are used (Burr et al., 2015) and it is unknown if they reflect the correct interparticle forces that are present for sediments on Titan. I used atomic force microscopy (AFM) to directly measure the cohesion forces between Titan aerosol analog (“tholin") particles and between walnut shell particles, a low density material used in the TWT. The result shows that cohesion between Titan sand is much larger than between walnut shell particles and silicate sand on Earth. This indicates that stronger wind is needed to blow sand on Titan than previously thought (Burr et al., 2015) and Titan sand could be formed by strong coagulation between aerosols. This work was published in *Journal of Geophysical Research (Planets)* as Yu et al., (2017b).

In Chapter 4, I investigated the mechanical properties of Earth and Titan related sand analogs. The origin of Titan sand has been a puzzle. There have been competing theories on whether the small aerosol particles grow on their own (“dry" mechanism) or whether they need liquid hydrocarbons to facilitate the growth (“wet" mechanism). However, most of the liquid hydrocarbon reservoirs are located in the polar regions of Titan, which suggests that if the Titan sand particles are made with the “wet" mechanism, they have to be transported for long distances before they can reach the equatorial regions and form the dunes there. I used a novel technique called nanoindentation to address this question, by measuring mechanical properties of thin films of tholin and other Titan sand analog materials. My results show that tholin is much softer and much more brittle than even the softest sand on Earth. I

thus concluded that the organic sand on Titan sand should be derived close to where it is located and thus is probably formed by the “dry" mechanism. This work was published in *Journal of Geophysical Research (Planets)* as Yu et al. (2018).

Chapter 2

The Effect of Adsorbed Liquid and Material Density on Saltation Threshold: Insight from Laboratory and Wind Tunnel Experiments

2.1 Introduction

Aeolian processes are fundamental in modifying the surfaces of all solid bodies in the Solar System with permanent or ephemeral atmospheres, including Earth, Venus, Mars, Saturn's moon Titan (Greeley and Iversen, 1985), Neptune's moon Triton (Smith et al., 1989), Pluto (Stern et al., 2015), and the comet 67P/Churyumov-Gerasimenko (Thomas et al., 2015). Studying aeolian features on planetary bodies enhances our understanding of near-surface winds, including the minimum wind speed to initiate saltation, wind direction, sediment flux, dune migration rates, and landscape modification. This information also provides input data and tests for global circulation predictions, leading to more powerful and accurate models. These models can then be run for

different conditions providing insight into past or future climates.

Threshold wind speed is a fundamental parameter for understanding how and under what conditions wind detaches particles from the surface. Boundary layer wind tunnels serve as powerful laboratories for the study of aeolian processes, including threshold wind speed. Boundary layer tunnels were first used by Bagnold (1941), who pioneered the study of the minimum wind speed needed to initiate saltation on Earth. To test whether the parameters for quantifying threshold wind speed on Earth were also appropriate for Venusian and Martian conditions, the Martian Surface Wind Tunnel (MARSWIT) and Venus Wind Tunnel (VWT, now refurbished to the Titan Wind Tunnel, TWT) were built. The MARSWIT simulates the atmospheric pressure on Mars (4.0–8.7 mb) with both martian atmosphere (CO_2) and dry air (Greeley et al., 1976, 1977, 1980). To simulate the weight of the grains under the lower gravity of Mars, low density materials like walnut shells have been used (Greeley et al., 1976). The VWT achieved the same atmospheric density as on Venus using CO_2, and employed quartz sand as sediment (Greeley et al., 1984a, b).

Cassini spacecraft data show extensive linear dunes covering 35% of equatorial regions ($\pm 30°$) of Titan (Lorenz et al., 2006; Radebaugh et al., 2008). The dune materials are likely dominated by radar-dark (wavelength 2.17 cm) organic materials deposited from the atmosphere, with some minor water ice (McCord et al., 2006; Soderblom et al., 2007; Barnes et al., 2008; Clark et al., 2010; Le Gall et al., 2011; Hirtzig et al., 2013; Rodriguez et al., 2014). Global circulation models and measurements from the Huygens Doppler Wind Experiment show the dominant surface transporting winds are weak winds with

speed less than 1 m/s (see e.g., Bird et al., 2005; Tokano, 2010) that are not enough the form the dunes on Titan. In order to address this mystery, as well as to quantify the threshold wind speed and to study other aeolian processes on Titan, the TWT was built (Burr et al., 2015a,b).

The robustness of wind tunnel experiments depends both on the degree of control of environmental conditions (e.g., pressure, relative humidity) and an understanding of experimental materials. The TWT simulates certain properties of Titan's near-surface atmosphere by using high pressure air (12.5 bar) to achieve the same Reynolds number (Re*) as on Titan. The Reynolds number is the ratio of inertial to viscous forces (Re*=u*D_p/ν, where u* is the threshold friction wind speed, D_p is particle size, and ν is kinematic viscosity); this dimensionless number characterizes whether flow is laminar ($Re^* \ll 1$) or turbulent ($Re^* \gg 1$). Titan has a surface temperature of 94 K, a surface pressure of 1.5 bar (Lindal et al., 1983, Fulchignoni et al., 2005), and an estimated atmospheric kinematic viscosity that is only about 1/12th of Earth (Burr et al., 2015a, Extended Data Table 1). The TWT at 12.5 bars and room temperature achieves the same value for kinematic viscosity (6.25×10^{-6} Pa·s) as on the surface of Titan. Low density materials have been used in threshold experiments in the TWT to compensate for Titan's low gravity, which is about $1/7^{th}$ that of Earth ($\sim$ 1.4 m/s^2). In the case of TWT experiments, a range of particle sizes and densities have been utilized to measure a wide span of potential conditions over which threshold can occur, thereby allowing extrapolation to the very low weight materials on Titan (Burr et al., 2015a).

The threshold wind speed is a function of the force balance of gravity (F_g),

aerodynamic lift (F_l), aerodynamic drag (F_d), and interparticle forces (F_i), as shown in Fig. 1. F_g is dependent on mass which, in turn, is proportional to material density. For relatively heavy materials like quartz, the density determination is straight forward. However, for low density materials, most of which are porous and irregular, density values can vary considerably depending on the density definition used (see Section 3.1). The density values used in literature for low density materials (Greeley et al., 1976, 1977, 1980, Burr et al., 2015a) are usually taken from manufacturer labels, which usually do not specify a specific density definition. Thus it is necessary to reevaluate the data from these manufacturer labels.

Interparticle forces consist of van der Waals, cohesion, and electrostatic forces. Van der Waals forces describe the dipole-dipole interactions between neutral molecules. Cohesion forces are the attraction forces between particles with condensed liquid on them. Electrostatic forces are the attraction or repulsion forces between charged particles or particles with different surface potential. On Earth, where water is abundant, cohesion forces are much larger than van der Waals and electrostatic forces (McKenna Neuman et al., 2003). On Titan, electrostatic forces likely dominate the interparticle forces (see discussion in Lorenz 2014, Burr et al., 2015a), and the same may be true on other planetary bodies where liquid water is not abundant, such as Mars, Venus, Triton, Pluto, and Comet 67P. On Titan, cohesion between liquid ethane or methane could also be important (Lorenz 2014). The surface tensions (γ_s) of liquid methane and ethane at Titan's surface temperature and pressure are only about 15–20 mN/m (Baidakov et al. 2013) and are lower than water at

25°C on Earth (γ_s=72 mN/m). Thus the cohesion force for liquid methane and ethane on Titan should be lower than the cohesion for water on Earth given the same relative humidity for their respective surface temperatures.

Using the TWT, Burr et al. (2015a) found that the experimental saltation threshold wind speeds are 50% higher than the model predictions of Iversen and White (1982) and Shao and Lu (2000). The inclusion in these models of a density ratio term (Iversen et al., 1976) with the very low density ratio (sediment density over atmospheric density) for Titan conditions caused the models to fit the TWT experimental data. Ongoing work includes using higher pressures in the TWT (15 and 20 bar) to further study the effect of the density ratio on threshold (Nield et al., 2016). Lower pressures are also used (1, 3, and 8 bar) to simulate possible past Titan conditions (possible past pressure as low as 0.7 bar, Charnay et al., 2014, Bridges et al., 2015).

The models used in the previous TWT work and many other wind tunnel experiments did not specify interparticle forces for different materials. The experiments also did not dry the materials, which were exposed to ambient atmosphere with relative humidity (RH) ranging from 45 to 65%. During the TWT runs, the air used in the wind tunnel had an RH of 20 to 35% in the current experimental regime. Thus the interparticle forces were likely dominated by cohesion forces because the electrostatic charges dissipate very quickly when RH is greater than 5% (Bunker et al., 2007). In order to correctly simulate aeolian processes on Titan, where electrostatic forces are predicted to dominate the interparticle forces (Lorenz 2014, Burr et al., 2015a), a quantitative understanding of interparticle forces is therefore necessary. To accurately

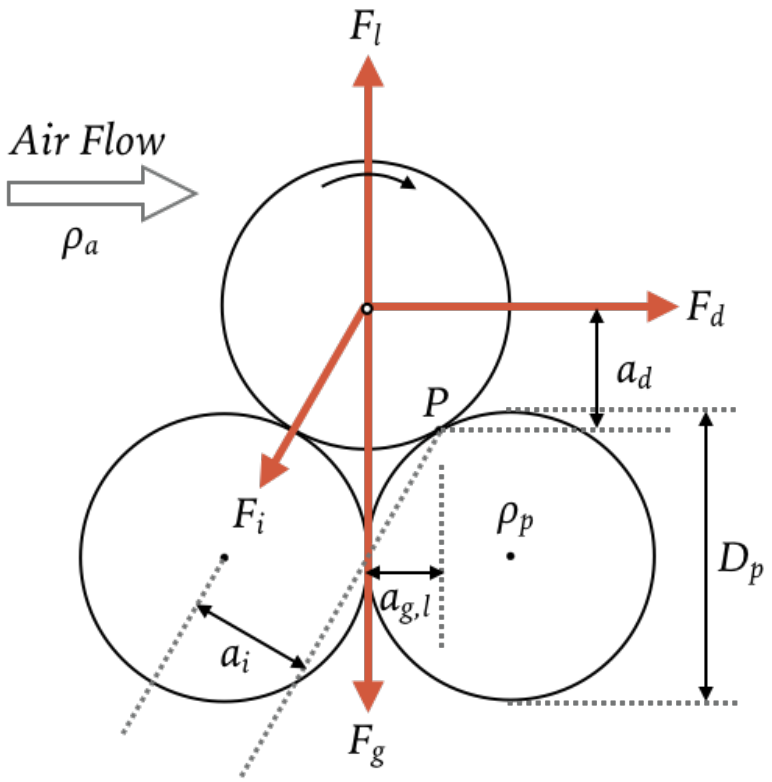

Figure 2.1: Forces acting on a particle stacked on two particles in airstream of density ρ_a (after Shao and Lu, 2000 and Kok et al., 2012). The particle density, ρ_p, and the particle size, D_p are the same for all three particles. The forces include gravity (F_g), the aerodynamic lift (F_l), the aerodynamic drag (F_d), and interparticle forces (F_i). The moment arm lengths a_g, a_l, a_d, and a_i correspond to F_g, F_l, F_d, and F_i, respectively.

translate the TWT results to Titan conditions where liquid water is absent, we need to assess the effect of water present in Earth-based experiments on interparticle forces. Because of their low densities, which are used to provide some compensation for low extraterrestrial gravitational accelerations, the materials commonly used as analog sediments in Martian or Titan wind tunnel simulations are particularly susceptible to interparticle forces, highlighting the importance of this issue for understanding planetary aeolian processes.

Table 2.1: Summary of variables.

Variable Symbols	Description	Unit
u*	threshold friction wind speed	m/s
D_p	particle diameter	m
ρ_a	air density	kg/m^3
ρ_p	particle density	kg/m^3
μ	dynamic viscosity	kg/(m·s)
ν	kinematic viscosity, μ/ρ_a	m^2/s
Re*	Reynolds number, u^*D_p/ν	-
g	gravity	m/s^2
RH	relative humidity	% by pressure
w	water content	% by mass
w′	initiation water content	% by mass

Previous studies of the effect of relative humidity on threshold which focused on Earth are reviewed below (Section 2). In Section 3.1, we summarize the common materials used in planetary wind tunnels and their basic properties according to the literature. The experimental methods are introduced in Section 3.2–3.4. We measured the density of materials in use in planetary wind tunnels (Section 4.1) and their gravimetric water content and Earth atmospheric equilibration timescales (Section 4.2). To further understand the effect of liquid on threshold, we measured the surface water content of the materials (Section 4.3). In Section 4.4, the threshold results of TWT experiments for wet and dry low density materials are shown. The implications for the threshold wind speed and entrainment of particles on Titan are discussed in Section 5.

2.2 Previous studies of the effect of water on threshold

Bagnold (1941) used the balance of gravity and aerodynamic drag to derive the threshold friction wind speed for dry sand:

$$u_b^* = A\sqrt{\frac{\rho_p - \rho_a}{\rho_a} g d} \tag{2.1}$$

where A is a function of Reynolds number Re* and interparticle forces. When Re*>3.5 (when particles are beyond the viscous sublayer and are more susceptible to fluid drag), A is found to be a constant, with A=0.1 in air and A=0.2 in water, ρ_p and ρ_a are the density of the particle and atmosphere, respectively, and d is the mean aerodynamic particle diameter. This function is only appropriate for dry sand particles over 200 μm; for smaller sediments, interparticle forces become more significant compared to the weight of the particles.

Belly (1964) conducted the first wind tunnel experiments on the effect of humidity on threshold using 400 μm sand, and found that,

$$u_w^* = u_b^*(1.8 + 0.6 \log w) = u_b^*(1 + \frac{1}{2}\frac{\mathrm{RH}}{100}), \tag{2.2}$$

where u_w^* stands for threshold for wet sand, u_b^* is the expression in Equation 2.1, w is the water content in percent by mass, and RH is the relative humidity in percent by pressure. When RH or water content increases, the threshold will increase accordingly. The results of Belly (1964) are shown in Fig. 2.2 (threshold RH) and Fig. 2.3 (threshold water content).

Iversen et al. (1976), Iversen and White (1982), and Greeley and Iversen

(1985) added interparticle forces and aerodynamic lift into the force balance and expanded the threshold model to small grains <200 μm. Their model is a piecewise function in three Reynolds number regimes. On the basis of a more explicit expression of interparticle forces, Shao and Lu (2000) simplified the model of Greeley and Iversen (1985) to a single equation:

$$u_{sl}^{*} = \sqrt{f(Re^{*})(\frac{\rho_p - \rho_a}{\rho_a} g d + \frac{\gamma}{\rho_a d})}, \tag{2.3}$$

with f(Re*) approximately equal to 0.0123, and γ between 1.65×10^{-4} N/m and 5×10^{-4} N/m. This threshold model is for loosely packed dry materials.

McKenna Neuman (2003) and McKenna Neuman and Sanderson (2008) slightly modified Shao and Lu's (2000) model for potentially humid or high/low temperature environments:

$$u_{w}^{*} = \sqrt{f(Re^{*})(\frac{\rho_p - \rho_a}{\rho_a} g d + \frac{\gamma'}{\rho_a d^2})}, \tag{2.4}$$

where

$$\gamma' = \frac{6}{\pi}\frac{a_i}{a_l} F_i, \tag{2.5}$$

and

$$F_i = \beta_c d + |\Psi| A_c. \tag{2.6}$$

The term a_i/a_l is the ratio of the moment arm lengths of interparticle and lift forces (see Fig. 2.1). The term $\beta_c d$ expresses the electrostatic and van der Waals forces. The term $|\Psi| A_c$ describes the effect of cohesion. Ψ is the matric potential (also called Laplace pressure, Δ_p) that describes the pressure difference caused by surface tension, and it can be expressed by the Kelvin

equation,

$$\Psi = (\frac{RT}{V_l})\ln(\frac{\mathrm{RH}}{100}), \tag{2.7}$$

where R=8.314 J mol^{-1}K^{-1} is the ideal gas constant for dry air, T is temperature in K, and V_l is the molar volume of the liquid (for water, V_l=1.8$\times$10^{-5} m^3 mol^{-1}). A_c is the total contact area of adsorbed water films between particles and is approximated in McKenna Neuman and Sanderson (2008) as,

$$A_c = \delta\pi kd(\delta/\delta_0)^n. \tag{2.8}$$

δ_0 is the thickness for a monolayer of adsorbed water, and δ is the water film thickness,

$$\delta = (\frac{H}{6\pi\Psi})^{1/3}, \tag{2.9}$$

and H is the Hamaker constant, an interaction parameter for adhesive surfaces (-1.9$\times$10^{-19} J, Iwamatsu and Horii, 1996; Tuller and Or, 2005). k is a dimensionless number describing the surface roughness ($\sim$ 10^{-4}–10^{-5}), and the power n varies between 6–8, depending on the surface roughness and particle packing arrangement. Both k and n are determined by fitting the experimental data to the model. Thus threshold wind speed is a function of matric potential Ψ. The introduction of matric potential is useful for both humid coastal areas and cold regions (McKenna Neuman and Nicklings, 1989, data shown in Fig. 2.3) since it incorporates two variables, temperature and relative humidity, into one single variable. However, its applicability to low density materials has never been tested. Based on Equation (4), the results for the threshold RH variation are shown in Fig. 2.2 for 125 μm (k=2.1$\times$10^{-4}, n=6.1) and 210 μm quartz sand (k=2.1$\times$10^{-4}, n=5.0). Note that compared to

slope of the threshold RH variation for 400 μm sand (Belly, 1964), the slope for 125 μm and 210 μm is lower, while it should be higher for smaller sediments according to Equation 2.4. This discrepancy may be due to the use of different threshold definitions (Fecan et al., 1999); Belly (1964) defined threshold as the point when bed movement is fully sustained, while McKenna Neuman and Sanderson (2008) defined it as the initiation of bed movement.

Fecan et al. (1999) and Ravi et al. (2004, 2006) further investigated the effect of humidity on soils with different amounts of clay. They argued that with the clay component in soil, the matric potential of McKenna Neuman and Nicklings (1989) for sand was no longer applicable because clay has much stronger adsorption forces to bond a layer of water film than quartz sand. Fecan et al. (1999) combined previous studies (Belly, 1964; Bisal and Hsieh, 1966; McKenna Neuman and Nickling, 1989; Saleh and Fryrear, 1995; Chen et al., 1996) and found an empirical formula for threshold as a function of gravimetric water content:

$$\begin{aligned} &\frac{u_w^*}{u_d^*} = 1 \text{ when } w < w' \\ &\frac{u_w^*}{u_d^*} = [1 + 1.21(w - w')^{0.68}]^{0.5} \text{ when } w > w' \\ &w' = 0.0014(\%\text{clay})^2 + 0.17(\%\text{clay}) \end{aligned} \tag{2.10}$$

where w is the water content per mass, and u_w^* and u_d^* respectively correspond to wet and dry threshold wind speeds. The result is shown in Fig. 2.3, and can be compared with the data and fitting of Belly (1964).

Fecan et al. (1999) defined an initiation water content w', where they

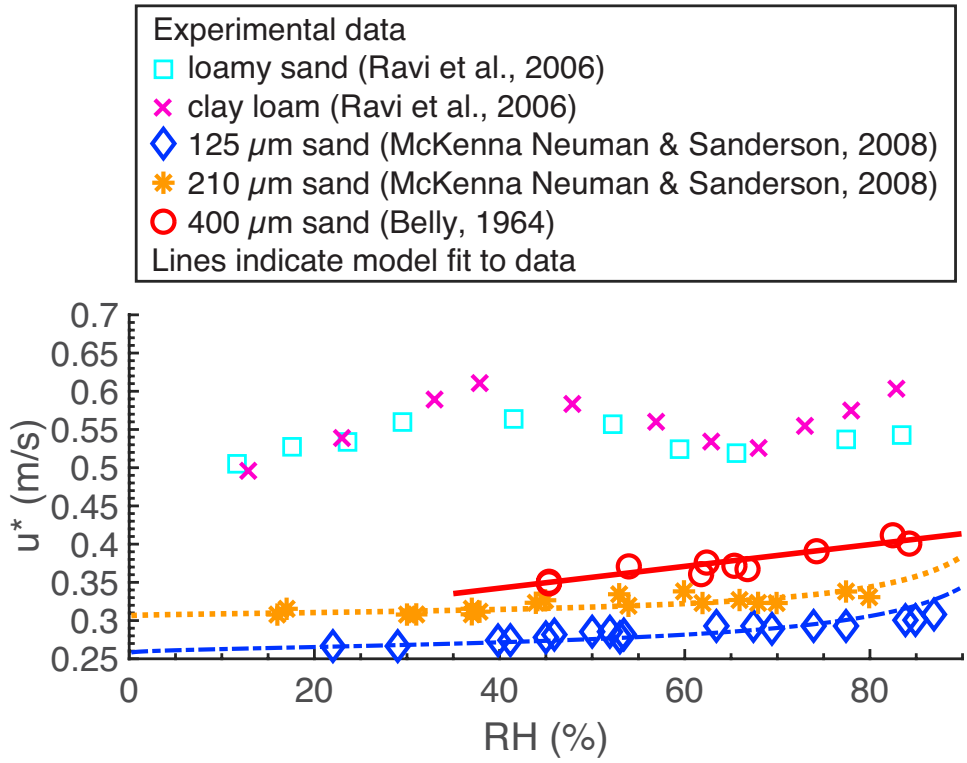

Figure 2.2: Threshold friction wind speed (u*) variation with relative humidity (RH). The symbols represent experimental data for: (1) 400 μm sand (Belly, 1964); (2) 125 μm sand (McKenna Neuman and Sanderson, 2008); (3) 210 μm sand (McKenna Neuman and Sanderson, 2008); (4) loamy sand with 8% soil clay content (Ravi et al., 2006); (5) clay loam with 31% soil clay content (Ravi et al., 2006). The lines show model fits to the data: (1) 400 μm sand using Equation (2); (2) 125 μm sand using Equation (4); (3) 210 μm sand using Equation (4).

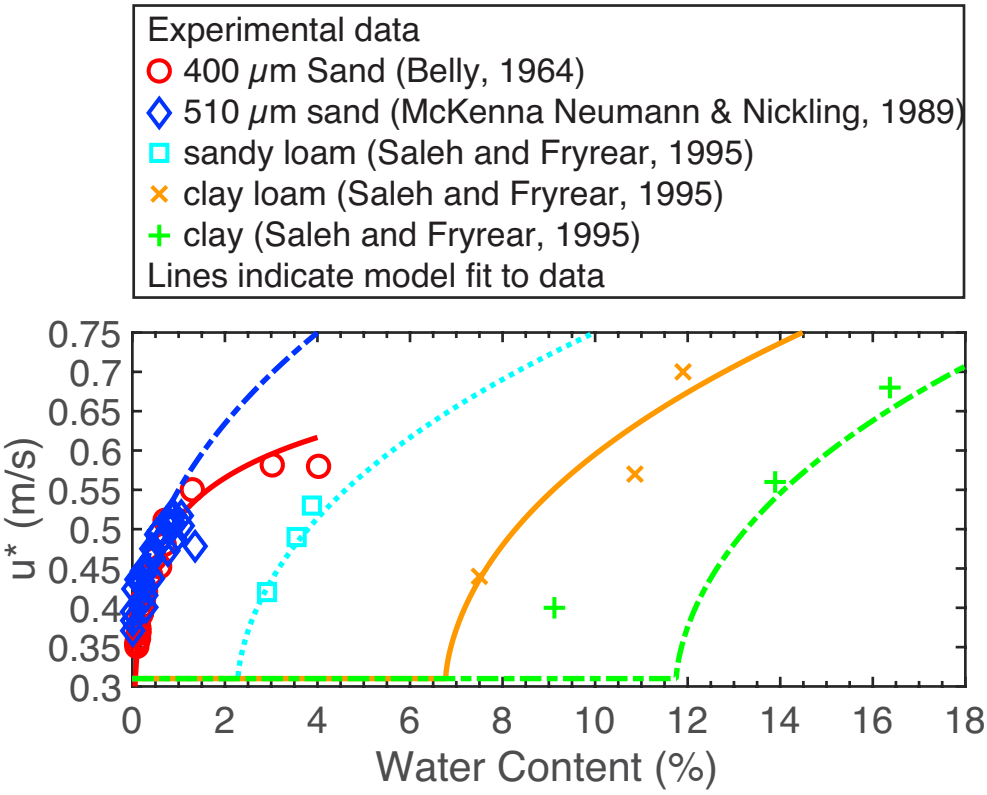

Figure 2.3: Shown here is the threshold friction wind speed (u*) variation with water content. The symbols represent experimental data for: (1) 400 μm sand (Belly, 1964); (2) 510 μm sand (McKenna Neuman and Nickling, 1989); (3) sandy loam with 12.2 % soil clay content (Saleh and Fryrear, 1995); (4) clay loam with 31.7 % soil clay content (Saleh and Fryrear, 1995); (5) clay with 49.2% soil clay content (Saleh and Fryrear, 1995). The lines show model fit to the data: (1) 400 μm sand using Equation (2); (2) 510 μm sand using Equation (10); (3) sandy loam using Equation (10); (4) clay loam using Equation (10); (5) clay using Equation (10).

showed that once the water content of soil exceeds w', the threshold increases with increasing water content in soil. However, wind tunnel runs with clay and sandy loam under a range of humidities found different results. Ravi et al. (2006) found threshold increases with increasing RH only when RH is less than 40% or greater than 65%. When RH is between 40% and 65%, threshold decreased with increasing RH. The wind tunnel results data from Ravi et al. (2006) for two kinds of soil (different clay content) are shown in Fig. 2.2. They explain the results as follows: 1) for low RH (RH<40%), an adsorption layer covers the particle (which happens only for soil with a clay component) and the cohesion forces are dominated by the adsorption forces; 2) for high RH (RH>65%), water condenses and forms liquid bridges between particles and the cohesion forces are mainly the capillary forces between liquid bridges; 3) for RH in between 40% and 65%, a transition between the adsorption forces and capillary forces occurs, resulting in lower interparticle forces (see Equation 2.11 below). They thus modified the interparticle forces F_i (Equation 2.6) in McKenna-Neuman (2003) by modifying the total contact area A_c to describe the transition region (45%<RH<65%):

$$A_c = \pi\left(\frac{w'}{\rho_w \sigma} - \frac{y}{2}\right)d \tag{2.11}$$

where w' is the soil moisture content, ρ_w is the water density, and y is the distance between the two contacting sphere particles. Because w' varies as $c\,|\Psi|^{-b}$, and b<1, the total cohesion $|\Psi| A_c$ is proportional to $|\Psi|^{1-b}$, and thus when RH increases, the cohesion forces decrease, leading to decreasing threshold wind speed.

Overall, previous studies of the effect of water on the threshold wind speeds agree that for coarse-grained materials, the more water the materials have, the higher the threshold. That is, when RH or water content of sand increases, the interparticle cohesion between the particles increases, leading to a higher threshold. However, for sand with clay components, the threshold decreases with an increase in RH when RH is between 45% and 60%, although it is still larger than threshold in dry conditions with dry materials (Ravi et al., 2006, see Fig. 2.2). Thus, we should expect a higher threshold for low density materials when RH is high or when materials are not dried and thus have a high water content.

2.3 Methods

2.3.1 Materials

Special care must be taken for planetary wind tunnels to reproduce relevant environmental conditions. As described in the previous section and shown in Table 2.2, there are several major planetary conditions that affect aeolian transportation: 1) transporting materials, 2) gravity, 3) atmospheric density, 4) atmospheric viscosity, and 5) density ratio.

The materials transported by wind on inner Solar System terrestrial planets (Earth, Venus, and Mars) are mainly from silicate rock, with Earth sediments dominated by quartz sand and Venus and Mars sediments are mainly mafic basaltic sand. For materials that have been used in the TWT, both quartz sand (including white silica sand and beach sand from Cemexusa) and basaltic sand (acquired from Pisgah Crater) are easy to acquire and resemble the real aeolian

sediments for Earth, Mars, and Venus. On the other hand, for icy worlds in the outer solar system, including Titan, Triton, and Pluto, the sediments are mainly organics. Analogs to those organic materials can be made in the laboratory ('tholins', Sagan et al., 1979 and Cable et al., 2012), but low yields and toxic composition means that they are not ideal for wind tunnel experiments, for which larger quantities are required ($\sim$ 3000 cm^3 for TWT). Tholins may also behave differently at room temperature than under Titan conditions. Laboratory experiments indicate that Titan tholins have an effective density (ρ_{eff}) of 500–1100 kg/m^3 (Hörst and Tolbert, 2013) and material density (ρ_m) of 1300–1400 kg/m^3 (Imanaka et al., 2012). Effective density and material density are related by a shape and porosity factor (S). When the particles are perfect spheres without pores (S=1), the effective density and material density are equal; irregularities and porosity both decrease S (Hörst and Tolbert, 2013). Here we use these two measurements to estimate the maximum and minimum values of the material density on icy bodies, including Titan.

To investigate aeolian planetary processes in an Earth laboratory, we have to use materials with lower densities to compensate for the higher gravity on Earth. For example, on Mars the material transported is basaltic sand with density of 3000 kg/m^3, but since Martian gravity is only about 3/8ths that of Earth, previous experiments have used lower density material (1100 kg/m^3) to simulate the weight of the materials as transported on Mars. Table 2.2 shows the density for equivalent weight aeolian materials on other planetary bodies. Low density materials that have been used in previous wind tunnel experiments (Greeley et al., 1980; Burr et al., 2015a) and which are investigated

here are walnut shells (from Eco-shell, Inc), gas chromatograph packing materials made from flux calcined diatomite (GC tan, Johns-Manville), iced tea powder (4C Totally Light), instant coffee (Foodhold U.S.A., LLC), activated charcoal (Sigma-Aldrich), and glass bubbles (3M).

To extend the previous work into threshold conditions on Titan (Burr et al., 2015a), we include additional materials with different densities. These additional materials include non-acid washed and acid washed glass beads (Mo-Sci Corporation, Sigma-Aldrich, 2500 kg/m^3), gas chromatograph packing materials made from calcined diatomite (GC pink, Johns-Manville, 2150 kg/m^3), and chromite (Reade Advanced Materials, 4000 kg/m^3). The materials investigated in this work include all the previously and currently used TWT materials (Greeley et al., 1980; Burr et al., 2015a). The materials are summarized in Table 2.3 in order of decreasing literature density values. The materials investigated in this study are the same batches (except iced tea powder and instant coffee) as the ones at the TWT, thus having the same size range as well as composition.

Table 2.2: Summary of planetary conditions. Values for Venus, Earth, Mars, and Titan are adopted from Burr et al. (2015b). For Triton and Pluto, atmospheric density values are derived using the ideal gas law, and surface temperature and pressure are adopted from Smith et al. (1989) and Gladstone et al. (2016), respectively. The atmospheric viscosity for Triton and Pluto is calculated by using gas type and temperature at http://www.lmnoeng.com.

Planetary Body	Density of Material ρ_p (kg/m^3)	Gravity (m/s^2)	Density of Equivalent Weight Material on Earth (kg/m^3)	Atmospheric Density ρ_a (kg/m^3)	Atmospheric Viscosity (Pa·s)	Density Ratio (ρ_p/ρ_a)
Venus	3000 basalt	8.9	2724	65	3.27×10^{-2}	46
Earth	2650	9.8	2650	1.2	1.85×10^{-5}	2.2×10^{3}

Table 2.3: Summary of material properties. GC indicates Gas Chromatograph packing materials. GC tan is calcined diatomite: according to Burr et al. (2015a), it a has different color compared to GC pink. For the literature density values, chromite, basalt, quartz sand, beach sand, and glass beads are standard values. Density of the GC pink, GC tan, activated charcoal, and glass bubbles were provided by the manufacturer. Density of walnut shells is originated from Greeley et al. 1980. Density of iced tea and instant coffee comes from FAO/INFOODS Density Database.

Material Name	Density in Literature (kg/m^3)	Size Range (μm)
Chromite	4000	212–250; 250–300
Basalt	3000	150–250; 250–500; 707–1000
Quartz Sand	2650	106–125; 125–150; 150–175; 175–212; 212–250
Beach Sand	2650	500–600; 600–700; 707–833; 833–1000
Glass Beads	2500	150–180 (non-acid washed); 150–180 (acid washed); 180–212; 500–600
GC pink	2150	125–150
GC tan	1300	150–175
Walnut Shells	1100	125–150; 150–175; 175–250; 500–600; 707–833; 833–1000
Iced Tea Powder	1030	N/A
Activated Charcoal	400	250–300; 425–500; 600–707
Instant Coffee	250	N/A
Glass Bubbles	100–140	30–115

	quartz					
Mars	3000 basalt	3.7	1132	0.015	1.30×10^{-5}	2×10^{5}
Titan	500–1400 organics	1.4	71–200	5.1	6.25×10^{-6}	78–294
Triton	500–1400 organics	0.78	40–111	$\sim 9\times10^{-5}$	$\sim 2\times10^{-6}$	$3.1–12.0\times10^{6}$
Pluto	900 methane ice	0.62	31–89 31–89	$\sim 9\times10^{-5}$	$\sim 2\times10^{-6}$	$3.1–12.0\times10^{6}$

2.3.2 Density Measurements

Measuring particle density requires a series of careful measurements. Mass is straightforward to obtain with an analytical balance. For this work, the mass of the materials was measured by an analytical balance (Satorius Entris 224-1S), with standard deviation of 0.1 mg.

The particle volume is more difficult to measure, because of a number of different definitions of density. Fig. 2.4 compares three densities: the bulk density (ρ_b), particle density (ρ_p), and material density (ρ_m). Bulk density has the smallest value, as the bulk volume includes: 1) volume of the solid material, 2) closed internal voids, 3) open pores of particles, and 4) interparticle voids. The volume defined in particle density (ρ_p) includes the volume of the solid material and the volume of the internal closed pores, whereas the material volume (ρ_m) only includes the solid material volume. The particle density can be smaller or equal to the material density, depending on porosity. When the particles have internal pores, the particle density is always smaller than the material density (Fig. 2.4). Conversely, when particles have no pores, the particle density is equal to the material density (Webb, 2001, also see Fig. 2.4).

Here we used an AccPyc II 1340 Automatic Gas (Helium) Pycnometer to measure the volume of the materials. The principle of the pycnometer is the gas displacement method and is illustrated in Fig. 2.5. Helium gas is first admitted into an empty compartment with calibrated volume V_{empty}, until it equilibrates with a certain pressure (Fig. 2.5(b)). The samples are sealed in a second calibrated cup with volume V_{cup}. After the pressure is stable in

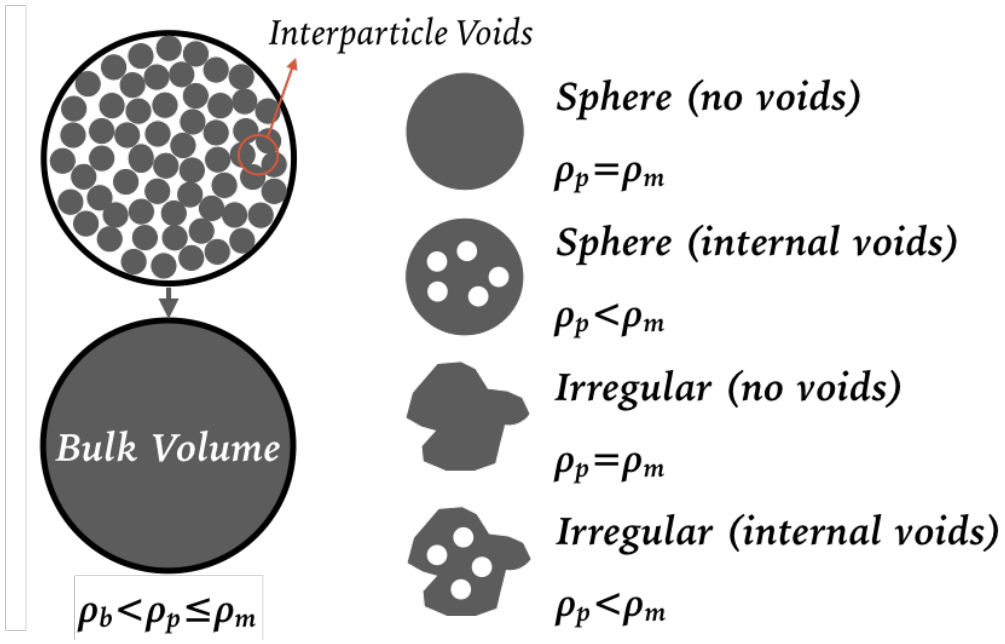

Figure 2.4: Comparison of different densities: bulk density (ρ_b), particle density (ρ_p), and material density (ρ_m), adapted from Webb (2001) and Hörst and Tolbert (2013).

the empty compartment (P_0), the helium gas is discharged from the empty compartment to the cup with the samples. The helium gas fills the spaces within the sample as small as ~3 Å rapidly, and the final equlibrated pressure in the system is recorded as P_{final} (Fig. 2.5). Using the ideal gas law:

$$P_0 V_{\text{empty}} = P_{\text{final}}(V_{\text{empty}} + V_{\text{cup}} - V_{\text{sample}}), \tag{2.12}$$

the pycnometer calculates the volume of the sample, V_{sample}. The volume of the materials (V) and the standard deviation are given automatically by the pycnometer after 10 purges and 20 runs with the materials.

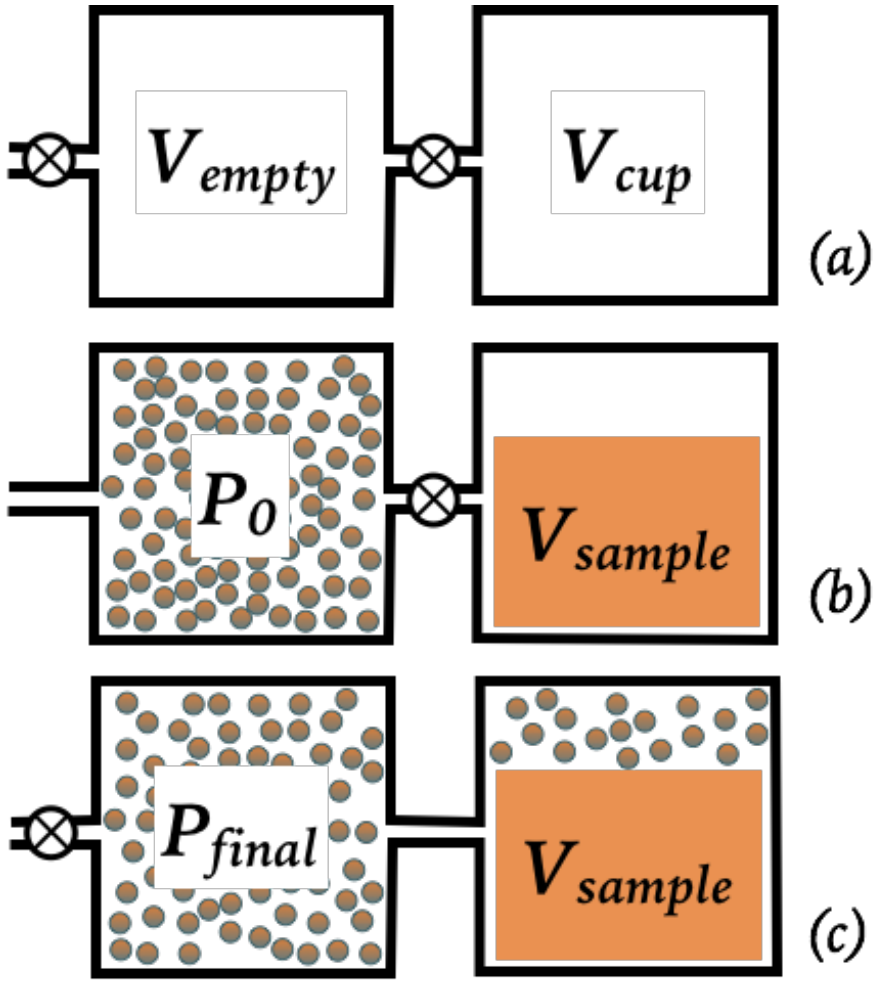

$$P_0 V_{empty} = P_{final}(V_{empty} + V_{cup} - V_{sample})$$

Figure 2.5: Pycnometer work flow and the ideal gas law used to calculate the volume of the sample (V_{sample}).

2.3.3 Gravimetric Water Content Measurements

We determine the water content of the materials by gravimetric measurements. The Relative Humidity (RH) and temperature in laboratory were recorded using a digital hygrometer (Dwyer Instrument) with 0–100% RH range (accuracy of $\pm$2%) and $-$30–85°C (accuracy $\pm$ 0.5°C). The materials were put in an aluminum foil boat during the measurement. To eliminate the water adsorption of the aluminum foil, we put the foil in a 120°C oven (Lab Safety Supply Model No.32EZ28, temperature accuracy $\pm$1°C at 100°C) for 24 hours, and weighed it immediately after removal (m'_{dry}). The weight of the aluminum foil boat increases over time until equilibrating with water moisture in the atmosphere (m'_{wet}), usually in about 10 minutes. Thus, the amount of water adsorption on the aluminum foil is:

$$\Delta m' = m'_{wet} - m'_{dry} \tag{2.13}$$

After the equilibration of the aluminum foil boat, we laid a thin layer of materials on the bottom of the boat. The materials and the boat were then dried together in the 120°C oven for 24 hours. A lower temperature (105 °C) was tried to bake the materials, but it didn't change the overall results. After drying, they were weighed again immediately (m_{dry}). Then we left the materials in air to let them equilibrate, weighing them every 0.5–5 minutes. When the weight of the materials no longer changed with time, we recorded this final weight (m_{wet}), ambient RH, temperature, and the time the materials took to equilibrate (t_{eq}). The final water content of the materials after they

equilibrate (at a given RH and temperature) is given by:

$$u(\%) = \frac{m_{wet} - m_{dry} - \Delta m^{'}}{m_{dry} - m^{'}_{dry}}. \tag{2.14}$$

2.3.4 Thermogravimetric (TGA) Measurements

Since many of the low density materials we used are porous, water is both adsorbed on the surface and absorbed in the interior of the particles. The surface water affects threshold by increasing interparticle cohesion, whereas the interior water changes the density of the materials. Therefore it is important to differentiate between surface and internal water. Surface and internal water are released at different temperatures and can be separated using thermogravimetric analysis (TGA). The samples, weighing 10–50 mg, were placed in an aluminum crucible and then loaded into a Mettler TGA/SDTA851e purged with nitrogen. The samples were heated from 25.0 to 600.0°C at a rate of 10.00°C/min. A slower heating rate (5.00°C/min) was tested on a walnut shell sample, but it did not change the overall results. The RH during the experiment was measured by the RH probe described in Section 2.3.

2.3.5 Titan Wind Tunnel Experiments Using 'Wet' and 'Dry' Sediments

To experimentally investigate the effect of water adsorption on threshold, we ran a set of experiments in the TWT at a range of pressures as a comparison study of walnut shells (size 125–150 μm) that were either subject to drying ('dry') or were in equilibrium with the ambient humidity at 1 bar ('wet'). The small end of the sediment size (125–150 μ m) was chosen for the 'wet' and 'dry'

runs because smaller particles are more sensitive to interparticle force change than larger particles with greater gravitational forces. To measure their water content, the 'wet' walnut shells were analyzed after the TWT run following the method described in Section 3.3, using a different analytical balance (A&D HR-120 with standard deviation of 0.1 mg) and oven (VWR Economy Vacuum Oven Model 1400E, temperature accuracy $\pm$3.5°C at 100°C).

To prepare the 'dry' walnut shells, we put the materials needed for a TWT run (approximately 3000 cm^3) in a 120°C oven for 24 hrs. Then we transferred all the materials into a desiccator (Lab Safety Supply, I.D. 300mm) with desiccant (Carolina, Silica Gel, Indicating Beads, Laboratory Grade) in preparation for the TWT experiment. While we set the bed for the TWT experiment (see Extended Data Figure 2 in Burr et al. 2015a), the materials were exposed to ambient air for 40 minutes. We chose the walnut shells for this experiment because their equilibration timescale, as discussed in Section 4.2, is longer than the time required to set the bed. The procedure for conducting experiments in the TWT can be found in Burr et al. (2015a). For the experiments presented here, the pressures in the TWT were 1, 3, 8, 12.5, 15, and 20 bars. The freestream wind speed was converted from dynamic pressure collected by pitot tubes in the TWT (for details, see Methods in Burr et al., 2015a; the only change is that the current TWT has the fixed pitot tube in the test section to collect dynamic pressure, instead of at the back of wind tunnel as described in Burr et al., 2015a).

2.4 Results and Discussion

2.4.1 Particle density measurement of wind tunnel materials

The particle density measurements show that for materials with densities over 2000 kg/m^3 (chromite, basalt, quartz sand, beach sand, glass beads, and GC pink), the measured densities are very close to the densities reported in the literature (see Table 2.4). However, for material densities less than 2000 kg/m^3 (GC tan, walnut shells, instant coffee, activated charcoal, iced tea powder, and glass bubbles), the measured densities differ from those in the literature or as provided by the manufacturer (see Table 2.5). Thus here we can divide the materials into two groups, high density and low density materials, where the division between low density and high density materials is 2000 kg/m^3.

The discrepancy between the particle density measured by the helium gas pycnomter and the density reported in the literature or by the manufacturer could be attributed to the different density definitions. The helium gas in the pycnometer can rapidly fill the open pores of the materials, thus the pycnometer measures the particle density (ρ_p<ρ_m if the particles have closed internal pores, or $\rho_p = \rho_m$ if the particles have no internal pores). The density reported in the literature may be bulk density given by the manufacturer, as it is with activated charcoal, iced tea powder, instant coffee, and GC tan (calcined diatomite). The density used for walnut shells in the literature is 1100 kg/m^3 (Greeley et al., 1980; Burr et al., 2015a), whereas the density measured by pycnometer gives 1400 kg/m^3. One possible explanation is that the densities given by the manufacturer are defined in other ways or are not

measured precisely. The density measured for the high density materials are likely closer to the literature value because those materials generally have no internal voids. However, the 'density' used in the TWT data analysis depends also on the porosity, surface area, size, and shape of the particles. Therefore, this value should fall between the bulk density and the material density, but probably closer to the material density because the wind can penetrate the interparticle voids.

Table 2.4: Summary of densities of high density wind tunnel materials (literature density greater than 2000 kg/m^3) in literature and measured by the pycnometer, with standard deviation in the measurements.

Material Name	Size Range (μm)	Density in Literature (kg/m^3)	Updated Density (kg/m^3)	Standard Deviation (kg/m^3)
Chromite	212–250	4000	4524.7	1.1
	250–300		4518.8	1.1
Basalt	150–250	3000	2841.4	1.1
	250–500		2882.8	2.0
	707–1000		2919.0	1.0
Quartz Sand	175–212	2650	2656.4	1.2
Beach Sand	500–600	2650	2631.2	2.2
	600–707		2639.0	0.8
	707–833		2634.3	1.2
	833–1000		2632.3	1.1
Glass Beads	150–180 (non-acid washed)	2500	2481.1	0.4
	150–180 (acid-washed)		2420.2	0.6
	180–212		2634.3	1.2
	500–600		2632.3	1.1
GC pink	125–150	2150	2364.6	2.2

Table 2.5: Summary of the densities of low density wind tunnel materials (literature density less than 2000 kg/m^3) in the literature and measured by the pycnometer, with standard deviation in the measurements.

Material	Size Range μm	Density in Literature (kg/m^3)	Updated Density (kg/m^3)	Standard Deviation (kg/m^3)
GC tan	150–175	1300	2006.1	5.0
Walnut Shells	125–150	1100	1426.5	1.0
	150–175		1419.1	0.9
	175–250		1418.8	1.0
	500–600		1415.4	2.6
	707–833		1407.2	2.7
	833–1000		1411.8	1.7
Iced Tea Powder	N/A	1030	1423.5	1.3
Activated Charcoal	250–300	400	1932.4	6.9
	425–500		1896.7	15.9
	600–707		1881.8	12.5
Instant Coffee	N/A	250	1473.9	1.2
Glass Bubbles	30–115	100–140	140.1	0.6

2.4.2 Water content and equilibration timescales of wind tunnel materials

The gravimetric measurements allow us to classify the materials by water content. As shown in Fig. 2.6, the materials can be divided into 2 groups: 1) materials with low water content (<1%), including all materials with literature densities over 2000 kg/m^3 (high density materials) and glass bubbles and 2) materials with high water content (>6%), including materials with literature densities less than 2000 kg/m^3 (low density materials), except glass bubbles. For the equilibration timescales shown in Fig. 2.7, we can classify the materials in the same way: low water content materials have a short equilibration time, usually less than 1 hr, while high water content materials have a long

equilibration time, over 6 hrs. For the same kind of material, both the water content and equilibration timescales show no apparent size dependence (Fig. 2.6 and Fig. 2.7).

One possible explanation for the high water content of low density materials is the combination of being hydrophilic and having large surface area-to-volume ratios, whereas the high density materials generally have smaller surface area-to-volume ratios and are hydrophobic. Glass bubbles are the exception; they are low density but they also have low water content ($\sim$0.05%) and short equilibration time ($\sim$15 min) like high density materials. This is because they are designed to have low surface-area-to-volume ratio and are hydrophobic.

In Fig. 2.8 we present the equilibration curves of two typical wind tunnel materials, quartz sand (low water content, high density) and walnut shells (high water content, low density). The walnut shells have much higher water content and equilibrate more slowly than quartz sand. In the first 10 minutes when quartz sand is approaching equilibrium, the walnut shells adsorb much more water by weight compared to quartz sand in the same time period. This correlation indicates water content and equilibration timescales are related. The long equilibration time for the low density materials also indicates that these materials cannot be dried quickly by circulating dry air in the wind tunnel. However, a short exposure time to air for the low density materials will not increase the water content to the equilibrium state.

We used the natural variation of humidity in the laboratory (15–60%) to see how water content varies as a function of RH. There is a linear relationship

between RH and water content for some of the materials shown in Table 2.6, including basalt, beach sand, walnut shells, activated charcoal, GC tan, iced tea powder, and instant coffee. They all have R^2 values greater than 0.8 for a linear relationship. These linear relationships could be used to estimate water content of materials when only RH is recorded. For chromite, glass beads, quartz sand, GC pink, and glass bubbles, the coefficients of determination R^2 for the linear relationships are only between 0.3–0.6. There may be a linear relationship between RH and water content for these materials as well, but the relationship is difficult to measure without a more precise analytical balance because of the low water content of these materials.

2.4.3 Surface and internal water of wind tunnel materials

As discussed in Section 3.4, surface water can change the interparticle cohesion and affect the threshold. The surface water measurements from TGA are listed in Table 2.7.

For materials with less than 0.2% water content, the mass loss was below the limit of detection for the TGA. Thus for high density materials like basalt, quartz sand, beach sand, and chromite, the surface and internal water content cannot be detected using the TGA. However, the high density materials are not porous or hydrophilic, thus the surface water content should equal the total water content, which we measured by gravimetric analysis.

For the low density materials like walnut shells, iced tea powder, and instant coffee, we can only get partial information from TGA, because thermal reactions will occur for these materials at high temperature. Generally, the

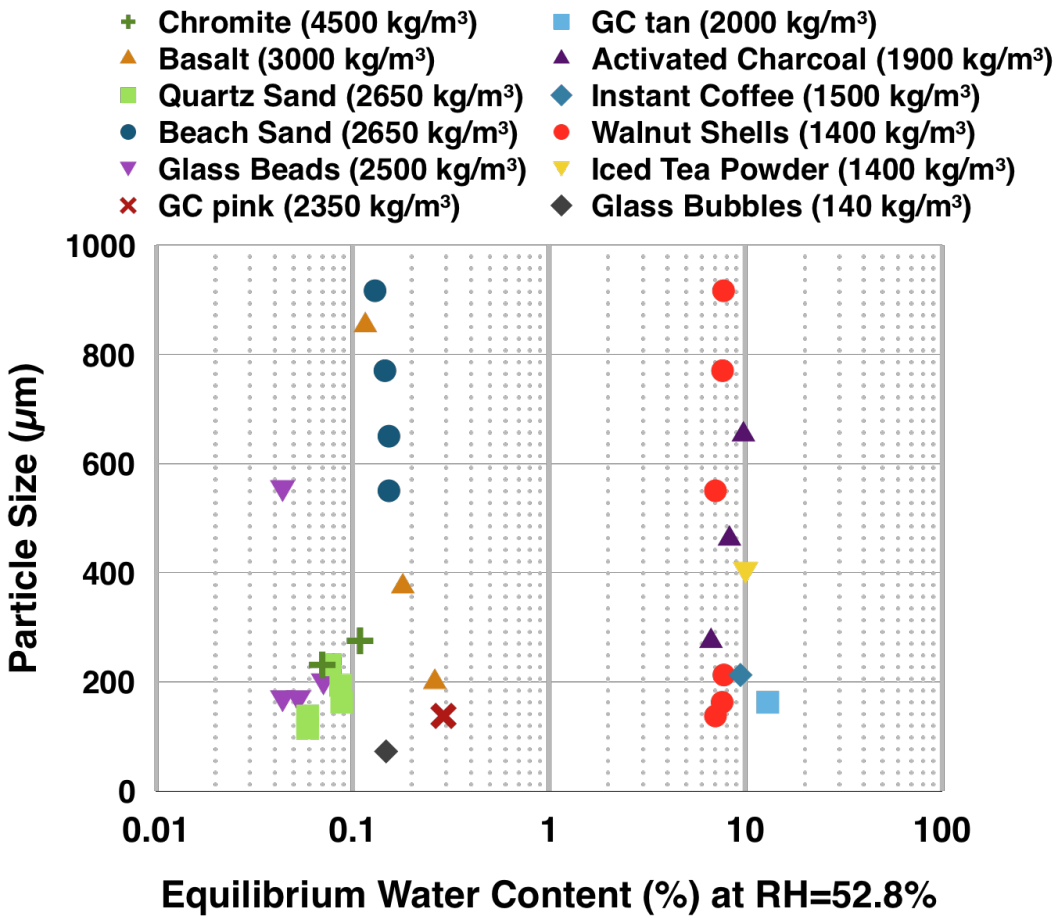

Figure 2.6: Water content of wind tunnel materials of different sizes at the same RH (RH=52.8%). Density values for the materials are adopted from the pycnometer measurements in Section 4.1.

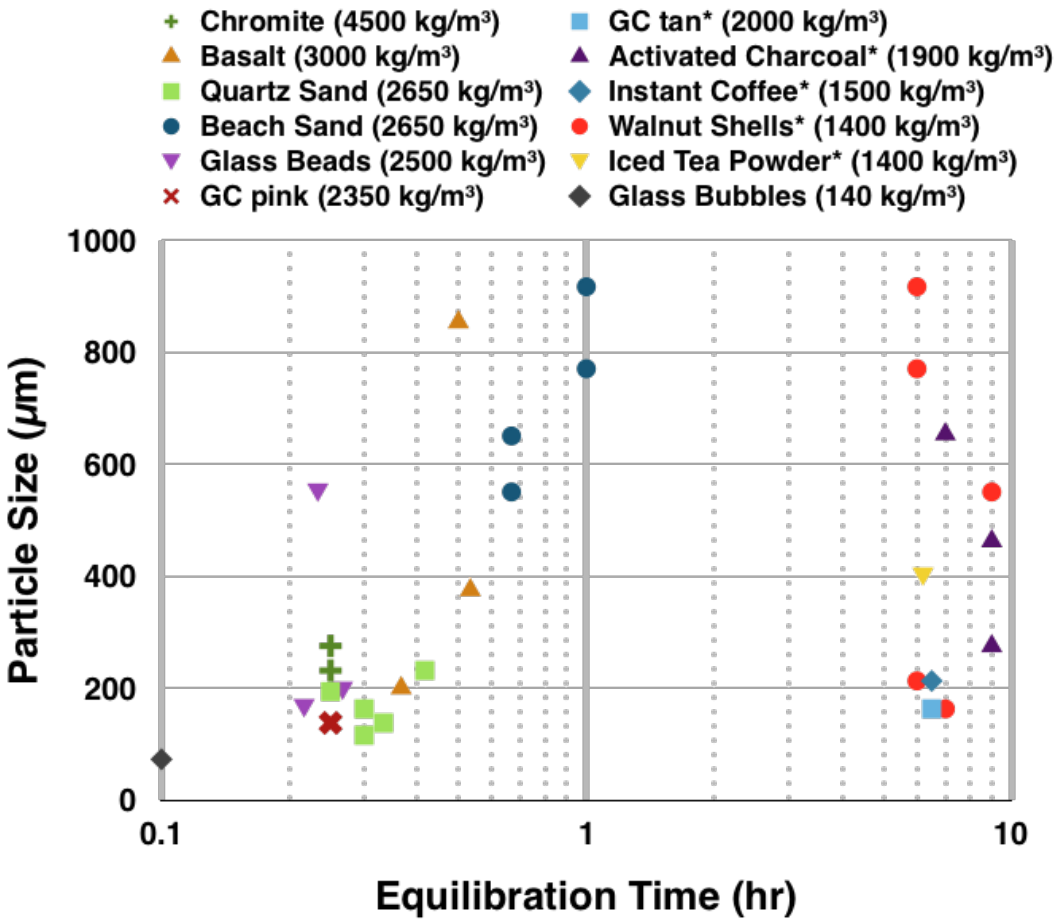

Figure 2.7: Equilibration Timescales of wind tunnel materials of different sizes. For the materials marked with * (GC tan, activated charcoal, instant coffee, walnut shells, and iced tea powder), the equilibrium timescales were long, so that the minimum equilibration timescales are plotted. Density values for the materials are adopted from the pycnometer measurements in Section 4.1.

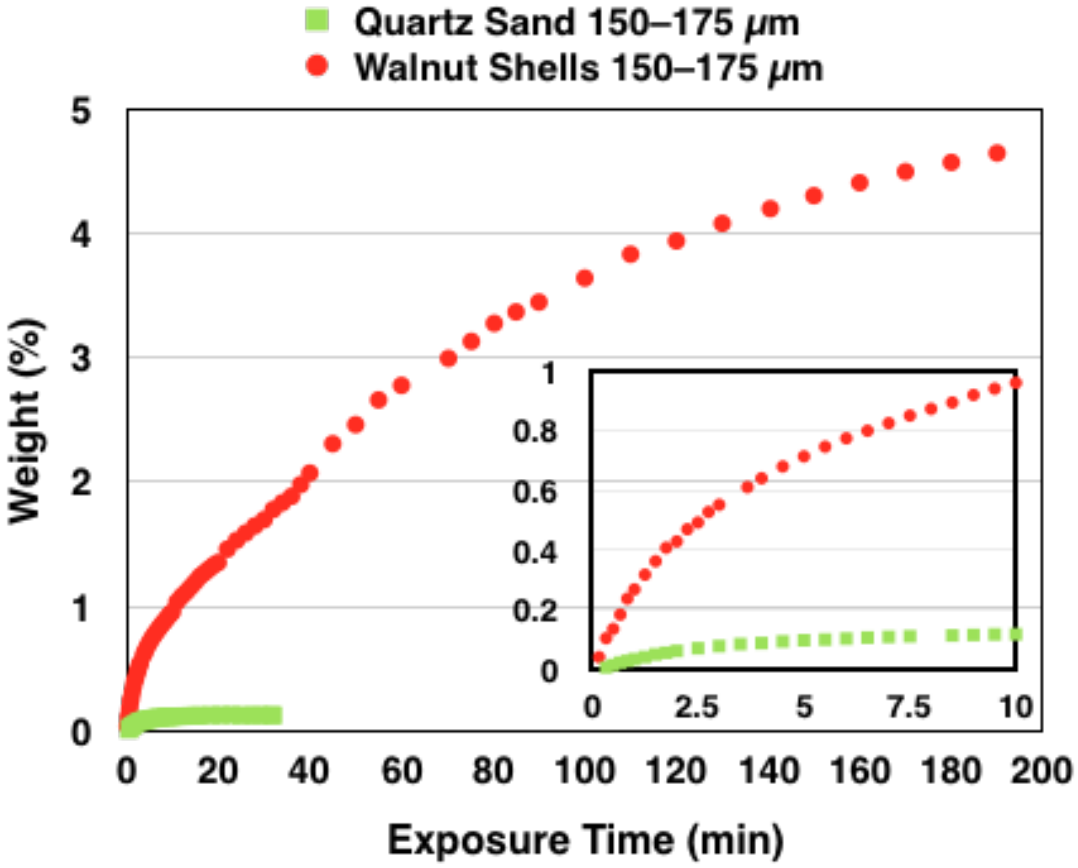

Figure 2.8: Comparison of water content and equilibration process of one low density (walnut shells 150–175 μm) and one high density (quartz sand 150–175 μm) wind tunnel material up to 200 minutes. The inset graph magnifies the comparison in the first 10 minutes.

Table 2.6: Summary of the RH and water content linear relationship of the wind tunnel materials, with R^2>0.8. The linear relationship is y=ax+b, where y is the water content by mass and x is the RH in %. R^2 is the coefficient of determination for each linear relationship. Quartz sand (all sizes), GC pink (125–150 μm), and glass bubbles have R^2 values that vary between 0.3–0.6, because their water content is very small ($< 1\%$) compared to other materials and the measured water content values have large deviations.

Material	Size Range (μm)	a	b	R^2
Basalt	150–250	1.93×10^{-3}	1.60×10^{-1}	0.944
	250–500	1.38×10^{-3}	1.06×10^{-1}	0.954
	707–1000	8.70×10^{-4}	6.58×10^{-2}	0.941
Beach Sand	500–600	1.22×10^{-3}	8.62×10^{-2}	0.930
	600–700	1.17×10^{-3}	8.87×10^{-2}	0.935
	707–833	1.15×10^{-3}	8.34×10^{-2}	0.964
	833–1000	1.06×10^{-3}	7.13×10^{-2}	0.953
Walnut Shells	125–150	9.87×10^{-2}	2.07	0.898
	150–175	8.28×10^{-2}	3.26	0.850
	175–250	8.24×10^{-2}	3.41	0.835
	500–600	8.02×10^{-2}	3.28	0.794
	707–833	7.90×10^{-2}	3.58	0.903
	833–1000	8.04×10^{-2}	3.51	0.815
Activated Charcoal	400–841	2.30×10^{-1}	-3.05×10^{-1}	0.946
GC tan	150–175	1.02×10^{-3}	7.88×10^{-2}	0.927
Iced Tea Powder	N/A	1.13×10^{-1}	3.79	0.929
Instant Coffee	N/A	1.13×10^{-1}	4.32	0.875

surface water of a material releases from about 50°C to 150°C, then its internal water starts to release from about 200°C. Walnut shells start to release their internal water from about 175–200°C, but thermal destruction begins around 202°C (Findorák et al., 2016), so we cannot get the internal water content of walnut shells directly from TGA measurement. For iced tea powder, thermal destruction happens at the lowest temperature of all the materials investigated, which is about 150°C. For instant coffee, thermal destruction happens at 175°C. Activated charcoal is stable during the entire heating process until 600°C. From Table 2.7, we can find that surface water occupies over 80% of the total water content for activated charcoal. Even for activated charcoal with extremely high porosity, the surface water still dominates.

The estimated total water content using the linear relationship in Table 2.6 should equal the sum of surface water and internal water. However, it seems clear from this analysis that most of the water measured, if not all, by gravimetric analysis is surface water.

Table 2.7: Separation of surface and internal water from TGA analysis for some of wind tunnel materials. We calculated the estimated water content values using the linear relationship of RH and water content from Table 2.6. The n/a* for basalt, quartz sand, beach sand, and chromite indicates no water was detected for those materials. The n/a† for walnut shells of all sizes, iced tea, and instant coffee indicated other chemical processes take place instead of the water loss process to high temperature, thus we cannot measure the internal water. For iced tea powder, neither the surface nor the internal water can be measured because chemical processes happen at lower temperature. The n/a‡ indicates the estimated water content of quartz sand and chromite at the specific RH are acquired from direct measurements rather than the linear relationships in Table 2.6.

Material Name	Size Range μm	RH (%)	Estimated Total Water Content (%)	Surface Water (%)	Internal Water (%)
Basalt	150–250	40	0.2	n/a*	n/a*
Quartz Sand	212–250	40	0.1 ‡	n/a*	n/a*

Table 2.8: The measured equilibration process of walnut shells 150–175 μm. The four walnut shells samples were baked for 24 hrs in a 120°C oven and then exposed to air (RH$\sim$40%) for 0, 2, 4, and 22 hrs. The surface water was then separated by TGA analysis.

Material	Size Range μm	RH (%)	Exposed Time (hr)	Surface Water (%)
Walnut Shells	150–175	40	0	0.3
		40	2	5.3
		40	4	5.3
		40	22	4.8
Beach Sand	500–600	40	0.1	n/a*	n/a*
Chromite	212–250	40	0.1‡	n/a*	n/a*
Walnut Shells	125–150	30	5.0	5.7	n/a†
	150–175	40	6.6	7.3	n/a†
	175–250	40	6.7	7.1	n/a†
	500–600	40	6.5	7.2	n/a†
	707–833	40	6.7	8.2	n/a†
	833–1000	40	6.7	7.9	n/a†
Activated Charcoal	400–841	30	6.6	4.0	1.0
Iced Tea Powder	N/A	40	8.3	n/a†	n/a†
Instant Coffee	N/A	40	8.8	6.2	n/a†

To understand the equilibration process for low density materials, we exposed dry walnut shells (150–175 μm) to ambient air for different lengths of time, and then measured their surface water content through TGA. The results are shown in Table 2.8. The surface water shows the same value for walnut shells exposed for 2 hours and walnut shells exposed for 4 hours, indicating the surface water equilibrates in 2 hrs or less. The walnut shells exposed for 22 hours have a lower surface water content value, which may have been caused by an RH change during the longer time period.

Overall, we found that water in low density materials is dominated by

surface water, while interior water occupies less than 20% of the total water content. Also, surface water is adsorbed first when dry materials are exposed to ambient air. Because only surface water would affect the interparticle cohesion, we believe for low density materials, a change of the water content of the materials would change their interparticle cohesion, and may affect threshold wind speed.

2.4.4 The effect of water adsorption on threshold wind speed

For the 'wet' walnut shells, the materials sat and were in equilibrium with ambient air (RH varies between 50–60%). The water content of the 'wet' walnut shells before the TWT run was 8.14% and after the TWT was 7.20%, which suggests that the materials were dried by the mixture of air in the TWT due to lower concentration of water vapor (see Section 1). During the TWT run, the RH outside the wind tunnel varied between 50.1% to 51.8%, while the RH inside the wind tunnel varied between 16.7% to 36.5%.

For the 'dry' walnut shells run, after drying and cooling down the sediments, the measured water content was 1.29%. After the bed was prepared and all the TWT runs finished, the water content of the 'dry' walnut shells increased to 1.67%. During this TWT run, the RH outside the wind tunnel varied between 51.6% to 53.7%, while the RH inside the wind tunnel varied between 3.7% to 11.9%. Note that the RH inside the wind tunnel for the 'wet' scenario is larger than the 'dry' scenario. So moisture may come out from the 'wet' walnut shells, thus increasing the RH inside the TWT.

Table 2.9 shows the threshold freestream wind speed for 'wet' and 'dry'

TWT runs at different pressures. The 'wet' thresholds for different pressures are consistently a couple percent larger than the 'dry' thresholds. However, the differences are smaller than the standard deviations of the threshold wind speed for both 'wet' and 'dry' runs.

The reason for the similar 'wet' and 'dry' thresholds may be due to the similar water adsorption behavior of walnut shells to clay minerals. According to the measurements done by Pirayesh et al. (2012), walnut shells consist of 46.6% of holocellulose, 49.1% lignin, and 3.6% ash. Holocelluose is rich in hydroxyl groups, similar to clay minerals (e.g., kaolinite). The free hydroxyl groups of holocelluose can thus adsorb water through hydrogen bonding, creating an adsorption layer covering the particles (Gwon et al., 2010), while lignin cannot adsorb such a layer of water (Nourbakhsh et al., 2011). Thus walnut shells behave like a mixture of 'clay' (hollucellulose) and 'quartz sand' (lignin). Note that clay also has long equilibration timescales and high water content similar to walnut shells (Ravi et al., 2006). Thus we would expect that walnut shells behave similarly to a clay/quartz mixture when subjected to water.

According to Fecan et al., (1999), with clay mixed into quartz sand, threshold does not change when the water content of the materials is below the initiation water content (w'). Threshold will only start to increase with increasing water content when the initiation water content is reached. And with increasing clay content in quartz sand, this initiation water content value is higher. This is caused by the different interparticle cohesion schemes of clay and quartz sand. For quartz sand, the interparticle forces are dominated

by capillary forces, which are of similar magnitude to the gravity and wind drag forces. Thus with increasing water content, the threshold will increase accordingly for quartz sand. While for clay minerals, when the water content is lower than the initiation water content value (w<w'), the interparticle forces are dominated by adsorption forces due to the molecular bonding between the hydroxyl groups in the clay minerals and water. Adsorption forces are much weaker than capillary forces, thus when the water content increases, even though adsorption forces are increasing, the threshold doesn't change significantly. When the initiation water content is reached (w>w'), the cohesion forces start to be dominated by capillary forces and the threshold wind speed begins to increase with increasing water content. Simply substituting the 46.6% holocellulose content as the clay content for walnut shells in Equation 2.10, we get the initiation water content value, w',

$$w' = 0.0014 * 46.6^2 + 0.17 * 46.6 = 11.0 \tag{2.15}$$

When water content of walnut shells is lower than 11.0%, interparticle forces are dominated by adsorption forces, which is much weaker than capillary forces. It is only when it exceeds 11.0%, that the interparticle forces are dominated by capillary forces and the threshold begins to increase with increasing water content. This comparison could explain the similar threshold results for the 'wet' and 'dry' walnut shells with water contents of 1.67% and 7.20%, respectively, as both values are lower than the initiation water content value.

Table 2.9: The threshold freestream wind speed for 'wet' and 'dry' TWT runs at different pressures. The standard deviations were calculated using the procedure in Burr et al. (2015a).

Pressure (bar)	'Wet' Threshold Freestream Wind Speed (m/s)	Standard Deviation (%)	'Dry' Threshold Freestream Wind Speed (m/s)	Standard Deviation (%)	Difference (%)
20	1.62	5.46	1.55	2.89	4.16
15	1.76	5.08	1.71	5.15	2.89
12.5	1.93	3.16	1.89	5.23	2.10
8	2.37	3.55	2.36	3.42	0.38
3	3.48	3.85	3.36	1.88	3.46
1	6.00	2.80	5.92	0.17	1.36

The low density materials are usually chosen to match the weight for the relevant planetary body. However, the low density materials may not have the same interparticle forces compared to the real transporting materials. For example, walnut shells used in both the MARSWIT and TWT are more similar to a clay/quartz mixture in terms of interparticle cohesion forces. GC tan (mixture of clay and other minerals), iced tea powder, and instant coffee are similar in that they all adsorb a layer of molecular bonded water (hygroscopic water) and have high water content and low density such that their interparticle forces should behave like walnut shells. They all have an initiation water content, after which the threshold starts to change with increasing water content (see the left column in Fig 2.9). On Mars, the transporting material is mostly basaltic sand, a high density material, and its interparticle cohesion should be closer to quartz sand. Quartz sand is hydrophobic, so it doesn't form the molecular bonded water layer. Rather, the water on its surface directly contributes to capillary water, as shown on the right column in Fig. 2.9. Thus with increasing water content of quartz sand, threshold increases accordingly.

Clay/Sand Mixture-like Materials	Quartz Sand-like Materials
Clay	Quartz Sand
Walnut Shells	Beach Sand
Iced Tea Powder	Basalt
Instant Coffee	Glass Beads
GC tan	Glass Bubbles

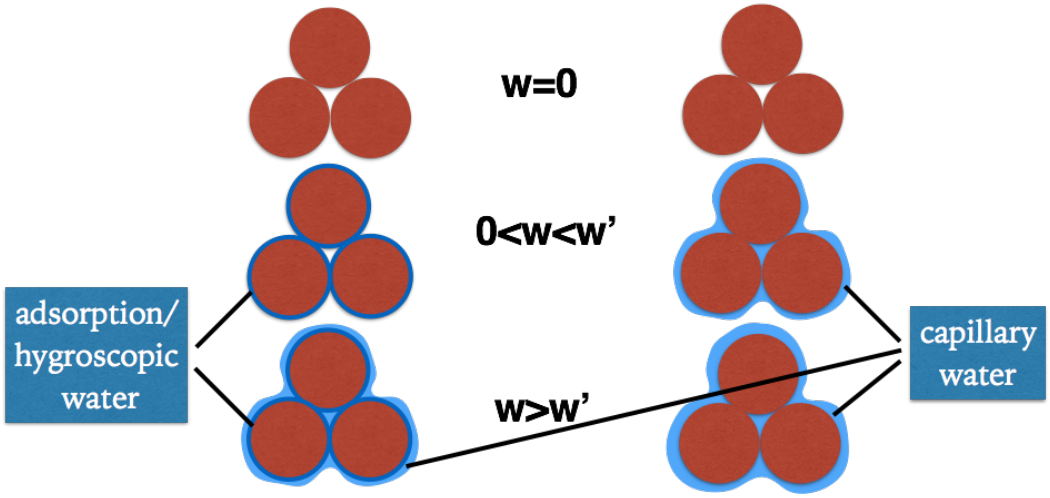

Figure 2.9: Lists of clay/quartz sand mixture-like materials and pure quartz sand-like materials and comparison of their behavior when subjected to water. The dark blue layer is the adsorption/hygroscopic water, while the light blue layer is the capillary water. The w is the water content of the material by mass, and w' is the initiation water content.

For materials with similar interparticle forces to quartz sand, we can use the model of McKenna Neuman and Sanderson (2008) to translate the TWT results to Titan conditions for different RH in the TWT. These materials have low water content and short equilibration timescales, including all high density materials and one low density material, glass bubbles (see Section 4.2). The conversion ratios to convert u^*_{TWT} to u^*_{Titan} for these materials are shown in Fig. 10(a) and Fig. 10(b, blue line). Materials that are similar to a clay/quartz sand mixtures need a certain water content to alter the interparticle forces from adsorption forces to capillary forces. For walnut shells, this initiation water content is predicted in Section 4.4, 11.0%. Using the RH-water content relationship for walnut shells in Table 6, we find that the corresponding initiation RH is about 90%. Since we have never observed such high RH in the TWT, here we only include the density correction (1400 kg/m^3 instead of 1100 kg/m^3), for the conversion ratios in Fig. 2.10(b). For GC tan, the density correction is 2000 kg/m^3 instead of 1300 kg/m^3. Since no size range is provided for iced tea powder and instant coffee, we cannot make a prediction for them. Activated charcoal is hydrophobic, its high water content is mainly attributed to its large surface area, and currently we cannot conclude which group it belongs to.

To correctly simulate different interparticle force regimes, determination of the water content of the materials is very important. If the water content of the material is high (>6%), as is usual for low density materials, the material likely behaves like clay when exposed to water. If the water content of the material is low (<1%), it may behave as quartz sand when exposed to water. Thus the

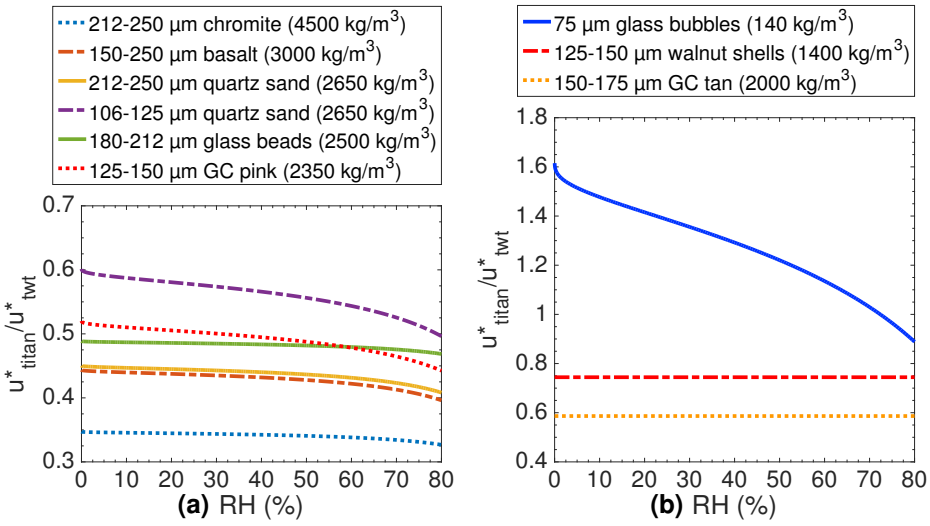

Figure 2.10: Modeled threshold wind speed ratios used for converting the u^*_{TWT} to u^*_{Titan} with variation of RH in the TWT between 0 to 80%, assuming the methane humidity on Titan is 0. (a) For high density materials of different sizes. (b) For part of low density materials, since iced tea powder and instant coffee have unknown size range, we cannot make the theoretical estimation.

determination of water content could not only distinguish the density of the materials, but more importantly, this information may provide insight on the effect of water RH on threshold. This information makes the only exception, glass bubbles (a low density material with a low water content), very useful in simulating both the gravity and interparticle forces of real transporting Titan particles. Although electrostatic forces can make these glass bubbles stick together (thus make them hard to sieve) and further experiments should consider this effect before using them.

2.4.5 The effect of methane humidity on tholins

On Titan, the transported material is dark organic sand (Barnes et al., 2008), with possible methane and ethane moisture affecting its cohesion force (Lorenz 2014). Laboratory studies of the adsorption of methane and ethane on tholins show that at saturation, tholins can adsorb only 0.3% of methane by mass (approximately a monolayer) or a monolayer of ethane (Curtis et al., 2008). As the molecular weights of water (18 g/mol) and methane (16 g/mol) are similar, the methane content of tholins may be close to the water content of quartz (and other high density materials). Thus it is possible that the interparticle cohesion of tholins (subjected to methane moisture) is similar to quartz sand (subjected to water vapor); that is, methane acts as capillary liquid instead of an adsorption liquid. With the increasing relative humidity of methane, or increasing methane content of tholins, the threshold wind speed for tholins or Titan's organic sand will increase accordingly, with no initiation liquid content like clay/quartz mixture or walnut shells (to water vapor).

Table 2.10: Modeling parameters for Titan. Hamaker constant for methane is adopted from Iwamatsu and Horii (1996) and Israelachvili (2011).

Modeling Parameter	Value
Temperature (T)	94 K
Particle Diameter (D_p)	125 μm
Air Density (ρ_a)	5.1 kg/m^3
Particle Density (ρ_p)	950 kg/m^3
Molar Volume of Methane (V_{CH_4})	1.6×10^{-5} m^3/mol
Hamaker Constant for Methane (H)*	-0.5×10^{-19} J
Roughness Dimensionless Number (k)	2.1×10^{-4}
Roughness Power (n)	4.5
f(Re*)	0.024

In the definition of the matric potential Ψ (Equation 2.7), when RH approaches 0, $\Psi \to -\infty$, and when RH is 100%, $\Psi = 0$. Thus when including the matric potential in calculating the thickness of the liquid film (Equation 2.9), the values become extreme when RH is very small or very large (see the solid blue curve in Fig. 2.11). These extreme RH values would also lead to extreme values for the threshold wind speed u*. To avoid this issue, we developed a second model incorporating measurements of methane film thickness on tholins in Curtis et al. (2008), shown as the dash-dot blue curve in Fig. 2.11, with a Langmuir adsorption isotherm fit. This thickness fit has no extreme values for the whole RH range and is more realistic compared to McKenna Neuman and Sanderson (2008). To calculate the total interparticle cohesion force, instead of using Ψ (Equation 2.6) we use another expression of the Laplace pressure Δp to avoid the extremes at RH=0 and RH=100% (Christenson, 1988):

$$\Delta p = \frac{\gamma_s}{r_m} \approx \frac{\gamma_s}{2\delta cos\theta}, \tag{2.16}$$

where γ_s is the surface tension of methane, 15 mN/m (Miquet et al., 2000), δ is thickness of the methane film, and θ is the contact angle between methane and tholins. Here we use cosθ=0.97 (Lavvas et al., 2011).

The results for the computed threshold variation with changing the relative humidity of methane are shown in Fig. 2.11. The solid red curve shows the modeling result of threshold wind speed variation with RH of methane under Titan conditions using the model of McKenna Neuman and Sanderson (2008), and the dash-dot red curve shows the modeling result incorporating the Langmuir model and data of Curtis et al. (2008). The solid red curve displays a more dramatic change with increasing methane RH than the dash-dot red curve; however, for both models, extreme methane humidity causes the threshold wind speed to change by less than 20%, compared to dry conditions (RH=0). This minimal change could be attributed to the lower surface tension of methane compared to water and Titan's low temperature. However, this explanation assumes the geometry, contacting mechanics, and electrostatic forces of Titan's organic sand is similar to Earth quartz, which is not known. Thus further research on these properties of tholins is necessary.

2.5 Conclusion

We measured various properties for low density materials used in planetary wind tunnels that have been missing or incomplete in the literature. The literature-given density of walnut shells, in use since the 1970s, 1100 kg/m^3, is lower than our measurement of 1400 kg/m^3, a difference of 30%. The effect of moisture on low density materials is also very distinct compared

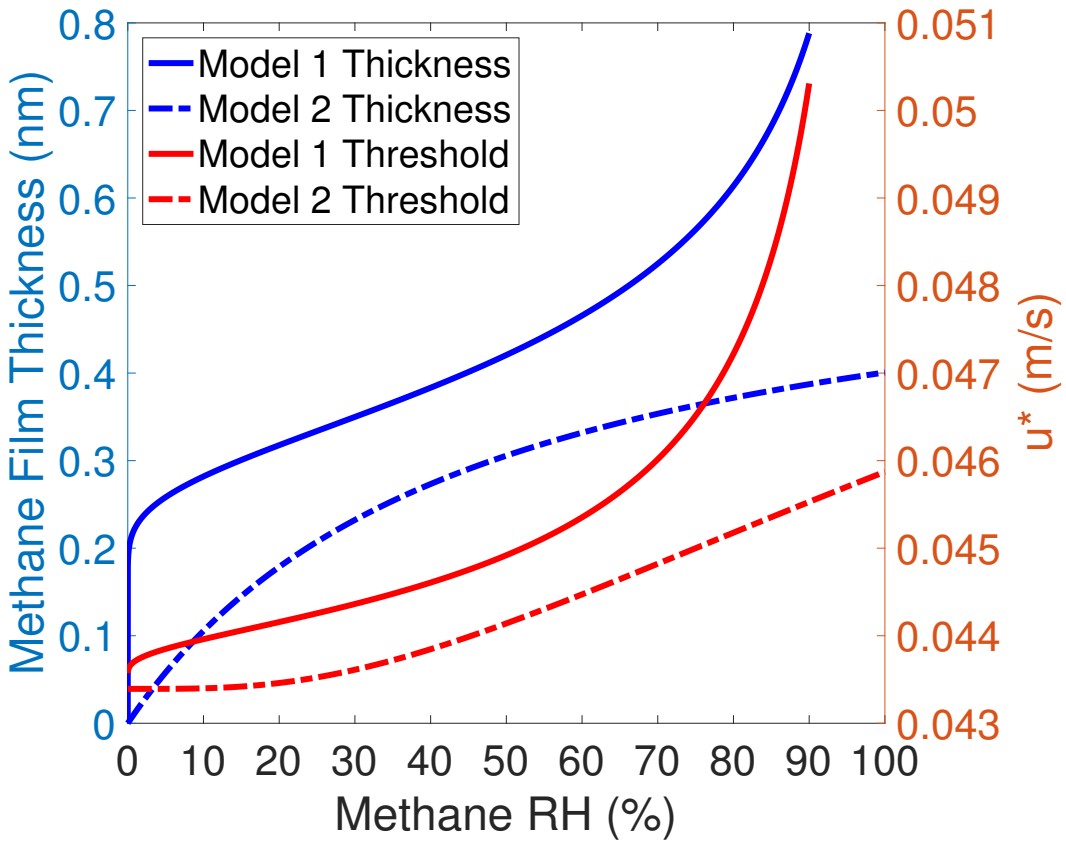

Figure 2.11: Two modeling results are shown of methane film thickness for 'tholins' and the threshold wind speed variation with changing relative humidity of methane. The blue curves shows the result for the methane film thickness and the red curves are the threshold wind speed variation with methane humidity. Model 1 refers to the revised McKenna Neuman and Sanderson (2008) model. As RH approaches 100%, the calculated thickness and threshold approach infinity, so here we only show RH between 0 to 90%. Model 2 shows the thickness and threshold wind speed variation with methane humidity using the data and Langmuir model of Curtis et al. (2008).

to high density materials. Low density materials generally have high water content (>6%) and long equilibration timescales (>6 hrs), while high density materials have low water content (<1%) and short equilibration timescales (<1 hr). The determination of the water content of the material provides insight into the sensitivity of threshold wind speed to RH based on our 'wet' and 'dry' walnut shell TWT runs. The results indicate that threshold is not very sensitive to 'wet' vs 'dry' walnut shells. The materials with high water content tend to behave like a clay/quartz mixture (where adsorption forces dominate below the initiation water content, and then the capillary forces dominate), whereas the materials with low water content are more likely to behave similarly to quartz sand (where capillary forces always dominate). When the interparticle forces are dominated by capillary forces, the threshold increases with increasing water content. Because tholins have a low methane content, we hypothesize that when the real transporting materials on Titan are subjected to methane moisture, they would behave similarly to quartz sand subjected to water.

Chapter 3

Direct Measurement of Interparticle Forces of Titan Aerosol Analogs ('Tholin') Using Atomic Force Microscopy

3.1 Introduction

Aeolian processes are ubiquitous on bodies with atmospheres (both permanent and ephemeral) in the Solar System, including Earth, Venus, Mars, Saturn's moon Titan (Greeley & Iversen, 1985), Neptune's moon Triton (Smith et al., 1989) Pluto (Stern et al., 2015) and the comet 67P/Churyumov-Gerasimenko (Thomas et al., 2015). To understand the origin of aeolian processes on Titan, the initiation of saltation has been investigated by measuring fluid threshold wind speed (the lowest wind speed to initiate saltation) using the Titan Wind Tunnel (TWT) (Burr et al., 2015). Complementary to such investigations, the fluid threshold wind speed can be predicted by deriving the force balance of stationary stacking particles. These forces include: the wind drag and lift

forces, gravity, and interparticle forces (Shao & Lu, 2000). During the TWT experiments, the wind drag and lift forces can be manipulated by changing the wind speed and flow regimes in the wind tunnel. The gravity on Titan can be simulated by using lower density material (density<2000 kg/m^3) in the wind tunnel on Earth. However, the interparticle forces are highly dependent on intrinsic material properties (e.g., surface energies). The low density materials used in the TWT (e.g., walnut shells), may have different interparticle forces compared to the real transporting materials on Titan, which are considered to be made of organics deposited from the atmosphere with minor water ice (McCord et al., 2006; Soderblom et al., 2007; Barnes et al., 2008; Clark et al., 2010; Le Gall et al., 2011; Hirtzig et al., 2013; Rodriguez et al., 2014). Thus measurements of the interparticle forces of both the Titan analog materials and the low density materials used in the TWT are necessary, so that we can correctly translate the TWT results to real Titan conditions.

The formation of dune particles ($\sim$100 μm) on Titan is not well understood. Barnes et al. (2015) proposed several mechanisms for haze particles to transform to sand-sized particles: 1) if the sand particles are produced by sintering or by lithification and erosion, then the composition of the sand particles would match the aerosols; 2) if the sand particles are produced by flocculation, the composition of the sand would be similar to the insoluble part of the aerosols in Titan's lakes; 3) the soluble part of the sand particles could form evaporites and the evaporites could be the sand source, too. However, both laboratory and theoretical studies showed that Titan aerosol analogues ('tholin') have low solubility in non-polar solvents (McKay, 1996; Raulin, 1987;

Coll et al., 1999; Sarker et al., 2003; Carrasco et al., 2009; He & Smith, 2014a), which are the major components of Titan's lakes (Brown et al., 2008). Thus, the soluble part of tholin may be a minor composition of Titan's sand. Measuring the interparticle cohesion of these Titan aerosol analog particles could also provide information about the formation of Titan's sand particles.

The interparticle forces consist of van der Waals force, capillary forces due to condensed liquid, and electrostatic forces. In very humid environments, capillary forces usually dominate over the other forces while in low humidity environments, van der Waals forces (solid-solid interaction) dominate at short-range separation. The long-range electrostatic forces may also play an important role in affecting sediment transportation once the particles are placed in motion, thus affecting the impact threshold (the lowest wind speed to maintain saltation, which is usually lower than fluid threshold) more than the fluid threshold.

Apart from intrinsic material properties, interparticle forces are also controlled by environmental conditions, such as relative humidity (RH) and temperature. On Earth, the relative humidity of water generally increases the interparticle forces through capillary condensation (e.g. Jones et al., 2002), while on Titan, the relative humidity of methane or ethane may affect the interparticle forces as well. Temperature also affects the interparticle forces, especially at temperatures near a substance's melting point; a melted quasi-liquid layer could form capillary bridges at surface asperities (the unevenness of surface). For ice in air, this quasi-liquid layer may disappear at around

$-20°C$ (Petrenko & Whitworth, 1999). Thus near the melting point, the interparticle forces increase with increasing temperature (e.g. Yang et al., 2004; Taylor et al., 2008).

There are a number of models which describe the adhesion between two smooth surfaces (Maugis, 1992). Two limiting equations are often used to describe the adhesion forces between smooth, dry surfaces. The DMT limit (Derjaguin, Muller, & Toporov, 1975) generally applies for hard materials and small contacting radii of curvature, and the JKR limit (Johnson, Kendall, & Roberts, 1971) describes the interparticle adhesion for soft materials and larger contacting radius of curvature. The application of either of the limiting equations depends on the elastic modulus and the surface energy. Here we measured these two material properties for tholin, through contact angle and elastic modulus measurements, thus we can theoretically predict the interparticle forces.

The above theoretical models of interparticle forces usually predict much larger results than found in experimental data. The challenge for these models is the use of over-simplified geometry; actual particles are not usually perfectly round and have asperities to decrease the real contact area. The irregularity and roughness of the particles makes the contact area smaller than if they were perfect molecularly smooth spheres. A number of models have been trying to describe the effect of roughness on adhesion forces (e.g. Greenwood & Williamson, 1966; Rumpf, 1990; Xie, 1997; Cooper et al., 2000; Rabinovich et al., 2000), however, exact predictions for real particles are still difficult. Thus it is still necessary for us to measure the interparticle forces between actual

particles.

The ability of atomic force microscopy (AFM) to measure forces as a function of surface separation enables us to directly measure the particle-surface or particle-particle separation forces at the single particle level; the forces measured are called the adhesion forces (or pull-off forces) (Ducker et al., 1991). A series of particle-surface interactions during one force-distance curve cycle (approach and retract) are shown in Figure 3.1. As the particle approaches the surface, the interaction force increases from zero to attraction between the particle and film. Then the particle may 'jump in' to the surface because of the attraction. As the surfaces are pushed together, a repulsive force will be measured. As the AFM cantilever retracts the particle from the surface, the adhesion forces between the particle and the surface will prevent separation. When the pulling force of the cantilever exceeds the maximum adhesion forces, the particle will 'jump out' from the surface. Thus the adhesion forces are dependent on the depth of this adhesion minimum. The adhesion forces between single particles reflect a combination of interparticle forces whose relative importance depends on environmental conditions and material properties.

The two limiting equations (DMT and JKR limits) to describe adhesion forces and the derivation of saltation threshold is reviewed below (Section 3). The experimental methods are described in Section 4.1–4.5. In Section 5.1, we used the measured intrinsic material properties: contact angles, surface energy, and elastic modulus of tholin to calculate the theoretical adhesion forces between tholin particles. The measured adhesion forces of AFM silicon

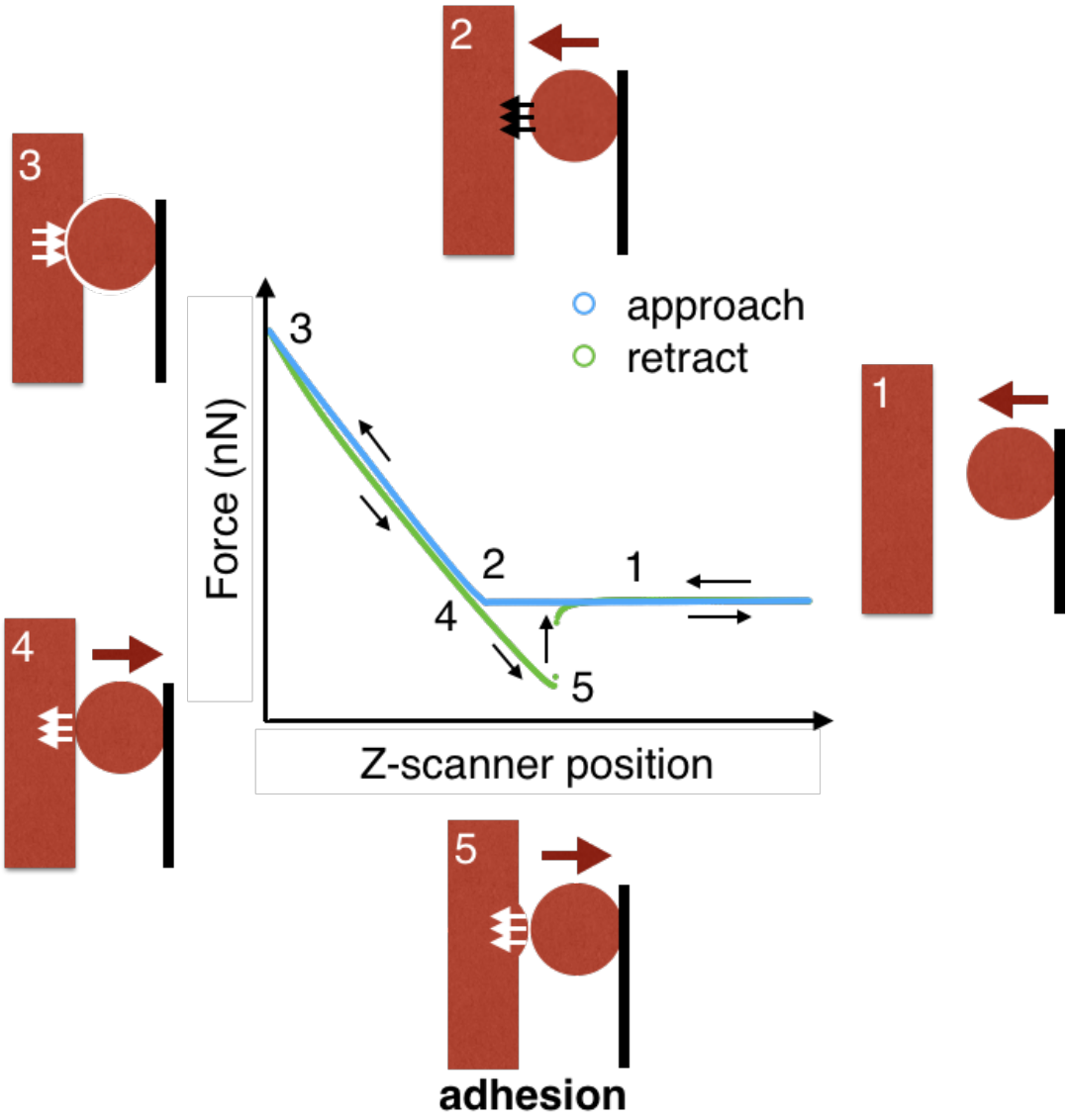

Figure 3.1: A typical force curve between a colloid particle and a smooth surface and the particle-surface interactions during different stages of approach and retraction (figure adapted from Haugstad, 2012). (1) The particle is far away enough from surface that there is no interaction force between the particle and surface. (2) The particle contacts the surface which may be proceeded by a slight short range attractive force (in this force curve the attraction is weak). (3) A repulsive force is measured due to the cantilever deflection and possible indentation/compression of the surfaces. (4) The AFM cantilever is retracted but the particle remains in contact. (5) At the final state of contact, the adhesion forces are equal to the maximum pull-off forces of the cantilever.

tip to several different surfaces are compared in Section 5.2. The results of the adhesion forces measurements for particle-surface and particle-particle interactions are summarized in Section 5.3. To further explore the effect of geometry and environmental conditions on adhesion forces, a tholin coated colloidal particle was used and we measured its adhesion to a flat tholin surface under different relative humidities (Section 5.4).

3.2 Background

Two simple models are often used to describe the solid-solid interaction forces of smooth, contacting surfaces under dry or low humidity conditions. The DMT model (Derjaguin, Muller, & Toporov, 1975) generally applies for hard materials and small contacting radii of curvature, and the interparticle forces can be expressed as:

$$F_{DMT} = 2\pi R^* W_A, \tag{3.1}$$

where R^* is the effective radius of curvature, given by $R^*=(1/R_1+1/R_2)^{-1}$, where R_1 and R_2 are radii of the contacting particles. W_A is the work of adhesion; for two solid surfaces made of the same material in vacuum/dry air,

$$W_A = 2\gamma_s \tag{3.2}$$

where γ_s is surface energy of the solid. On the other hand, the JKR model (Johnson, Kendall, & Roberts, 1971) best describes the interparticle adhesion for soft materials and larger contacting radius of curvature, the interparticle

forces for this model are:

$$F_{JKR} = \frac{3}{2}\pi R^* W_A. \tag{3.3}$$

In order to know which model is appropriate for the system we are investigating, we need to calculate an the elasticity parameter λ to determine which regime applies (Haugstad, 2012):

$$\lambda = \frac{2.06}{\xi_0}\left(\frac{R^*\gamma_s^2}{\pi K^2}\right)^{1/3}, \tag{3.4}$$

where $\frac{1}{K} = \frac{3}{2}\frac{1-\nu^2}{E}$, $\nu = 0.3$ is the poisson ratio, E is the elastic modulus of the material, and ξ_0=0.16 nm is the equilibrium interatomic distance. The DMT model applies when λ <0.1 and the JKR model applies when λ >5. For tholin, neither its surface energy (γ_s) nor its elastic modulus (E) is known, so we cannot predict its interparticle forces under dry conditions. Regardless of which model is applied, the interparticle forces will be a function of particle size and surface energy; thus the uncertainty from the two parameters could strongly affect the calculated theoretical interparticle forces, as well.

The DMT and JKR models only apply for dry or low humidity conditions. At higher RH, when liquid starts to condense on the particles or the surface, the interparticle forces begin to be dominated by capillary forces:

$$F_{capillary} = 4\pi R^* \gamma_L cos\theta, \tag{3.5}$$

where γ_L is the surface energy of the condensed liquid and θ is the contact angle between the liquid and the solid surface.

Shao and Lu (2000) used the balance of gravity ($F_g \propto d^3$), aerodynamic

drag and lift (F_d and F_l both $\propto d^2$), and interparticle forces ($F_i \propto d$) to derive the threshold friction wind speed:

$$u_{sl}^* = \sqrt{f(Re^*)(\frac{\rho_p - \rho_a}{\rho_a} g d + \frac{\gamma}{\rho_a d})}, \tag{3.6}$$

where

$$\gamma = \frac{6}{\pi} \frac{a_i}{a_g} \beta, \tag{3.7}$$

where d is the diameter of the particles, a_i and a_g are the moment arm lengths of the interparticle and gravity forces, respectively. The values of f(Re*) and γ are acquired by fitting the experimental data from Iversen & White (1982), where they used a boundary layer wind tunnel to measure threshold wind speed for various materials of different densities (1100–2650 kg/m^3) and sizes (37–673 μm). They found f(Re*) is approximately 0.0123, and γ is between 1.65–5 N/m (Shao & Lu, 2000). The value of β links to the magnitude of the interparticle forces:

$$F_i = \beta d.$$

Note that the JKR and DMT theories show that β is in the range of $1.5\pi\gamma_s$ and $2\pi\gamma_s$. Roughness will further decrease β. For a 100 μm diameter particle, the interparticle forces are estimated to be on the order of 10 μN ($\beta \sim 10^{-1}$ N/m). However, to fit the experimental threshold wind speed data, Shao and Lu (2000) found out the interparticle forces are only on the order of 10^{-2} μN ($\beta \sim 10^{-4}$ N/m), which is not only several orders smaller than the estimated value (10 μN), but also one order smaller than the measured value for quartz sand ($F_i \approx 0.1$ μN, Corn, 1961).

The interparticle forces used in Shao and Lu (2000)'s model are not specific

for any particular materials, because the model did not link the range of the parameter γ or β (see Equation 3.7) to material properties. This might be particularly problematic for Titan because the transporting materials on Titan are mainly organic and their intrinsic interparticle cohesion (the β parameter) could be very different from silicate materials on Earth for which the models were developed.

3.3 Methods

3.3.1 Samples and Preparation

Tholins were produced by exposing 5% CH_4/N_2 gas mixture to a glow plasma discharge (pressure: 3 Torr, temperature: 100 K), with a 10 sccm flow rate (He et al., 2017). Tholins were deposited: 1) on four mica discs (10 mm diameter), 2) three colloidal probes (AFM cantilevers from sQube with a $\sim$20 μm diameter borosilicate glass sphere attached to the end of the cantilever), and 3) on the wall of the chamber. The tholin films deposited on mica discs are approximately 1 μm thick, and their RMS roughness is $\sim$1 nm. Figure 3.2(a) shows a scanning electron microscopy (SEM) micrograph of one of the tholin-coated colloidal probes. Tholin particles deposited on the chamber wall were collected in a dry N_2, oxygen free glove box. The representative Titan Wind Tunnel materials (walnut shells 125–150 μm), are from the original TWT batches used in Burr et al. (2015) and Yu et al. (2017).

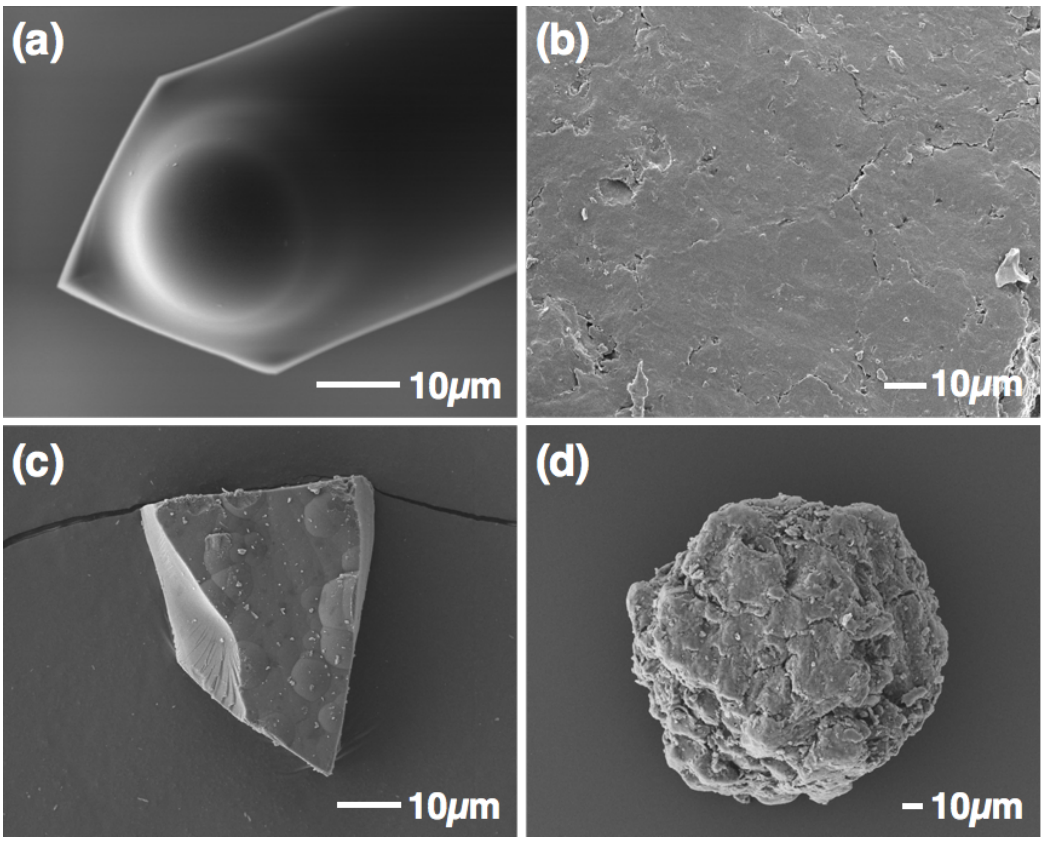

Figure 3.2: SEM images of: (a) a tholin-coated colloidal AFM probe (the coated sphere is about 20 μm in diameter); (b) the flat side of a walnut shell particle (size $\sim$800 μm) for tip–surface and particle-surface interactions; (c) a typical tholin particle (size $\sim$30 μm) used for particle-particle adhesion forces; (d) a typical walnut shell particle (size 125–150 μm) used for particle-particle adhesion forces.

3.3.2 AFM and cantilevers

We used a Bruker Dimension 3100 atomic force microscope. The spring constants of the cantilevers were calibrated by thermal tuning. The spring constant of the regular cantilevers is about 40 N/m and those of the colloidal probes is approximately 2.8 N/m. The sensitivity of the AFM photodiode is measured by indenting a hard surface (cleaved mica sheets, detailed in McGuiggan et al.. 2011).

3.3.3 Elastic Modulus Measurements

We used the AFM as a nanoindenter to measure the stiffness of tholin. We performed two cycles of force-separation curves on a hard surface (silicon, assume no indentation) and on a smooth tholin surface. The z scanner distance (x-axis in Figure 3.1) on the hard surface was subtracted from the z scanner distance on the sample surface to get a force (F)–indentation (δ) curve. The elastic modulus (E) of tholin can then be found as a function of indentation as:

$$E = \frac{3(1-\nu^2)F}{4R^{*1/2}\delta^{3/2}}, \tag{3.8}$$

where ν =0.3 is the Poisson ratio and R* is the radius of the AFM tip ($\sim$10 nm).

3.3.4 Contact Angle Measurements

We performed contact angle measurements on a flat tholin film. We used both a polar (deionized water) and a non-polar (diiodomethane, CH_2I_2) liquids, which usually yields the most reliable surface energy results (Hejda et al.,

2010). We also used heptane as an analog to liquid methane or ethane, since the surface tensions are similar (around 20 mN/m). Contact angles were determined by using a Ramé-Hart goniometer.

When a liquid droplet forms on a flat solid surface in an inert atmosphere, we can balance the three phases (liquid, solid, and air) energies by using the Young-Dupré equation:

$$W_{sl} = \gamma_l(1 + cos\theta), \tag{3.9}$$

where γ_l is the surface energy of the liquid, W_{sl} is the work of adhesion (energy to separate the solid and liquid) of the liquid and solid, and θ is the contact angle between the liquid-air interface and the solid surface. Using the geometric mean method, the work of adhesion W_{sl} can be also approximated as (Owens & Wendt, 1969):

$$W_{sl} = 2(\sqrt{\gamma_s^d \gamma_l^d} + \sqrt{\gamma_s^p \gamma_l^p}), \tag{3.10}$$

where γ_s^d and γ_l^d are solid and liquid dispersion contributions to the surface energy, and γ_s^p and γ_l^p are the solid and liquid polar contributions to the surface energy. When the contact angle measurements are done using two liquids, we have two sets of equations 3.9 and 3.10 to solve for the surface energy of the solid. A similar harmonic mean method developed by Wu (1971) was also used to calculate the surface energy and the results are similar to the geometric mean method.

3.3.5 Adhesion Force Measurements

We performed force-separation curves on four different simple systems to measure adhesion forces, as shown in Figure 3.3. The adhesion force measurements were all done at a scan rate of 1.5 to 2 Hz ($\approx$4 μm/s). There was no change in the measured adhesion forces at rates of 0.5 Hz, 5 Hz, and 10 Hz and there was no change in the measured adhesion forces.

To study tip-flat adhesion, we conducted force distance curve with a bare silicon AFM tip to 1) a flat tholin deposited film, 2) a flat quartz surface (Pelco Quartz Substrate from Ted Pella, Inc), and 3) the flat side of a walnut shell particle (size $\sim$800 μm, see Figure 3.2(b)), as shown in Figure 3.3a.

To study particle-flat and particle-particle cohesion, two kinds of particles were used: a tholin particle ($\sim$30 μm, see Figure 3.2(c)) and a walnut shell particle ($\sim$125–150 μm, see Figure 3.2(d)). They were glued to AFM cantilevers using epoxy resin. Force curve measurements were conducted for these particles to both flat film (for walnut shell, we used the flat side of an 800 μm particle) and particles made of the same material as the glued particle, as shown in Figure 3.3b and 3.3c. For each particle-flat and particle-particle cohesion measurement, 2–4 spots on the film or 2–4 particles on the substrate were chosen randomly and 6–20 pairs of approach-retract force curves were taken.

To study the variation of adhesion forces with different humidities, we performed the measurements using more controlled contact geometry: a colloidal probe coated with tholin was used as the cantilever. Force curves were obtained between the probe and a flat tholin film, as shown in Figure 3.3d.

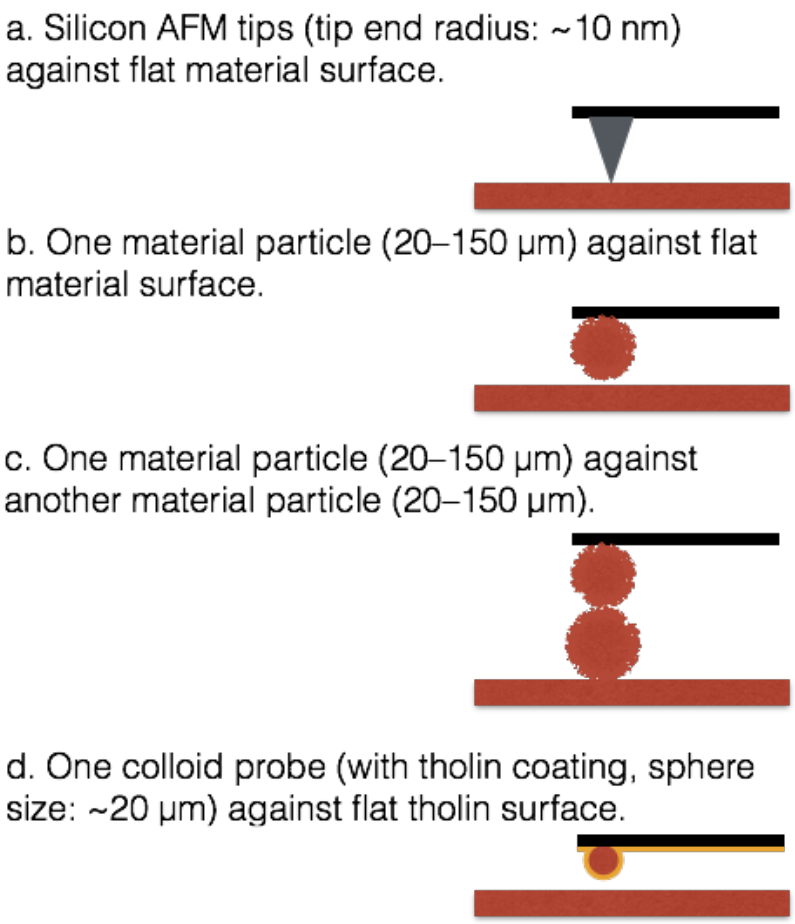

Figure 3.3: The four types of AFM setup used for the adhesion measurements. Figure adapted from Jones et al., (2002).

We also investigated the effect of relative humidity (RH) on adhesion forces for the tholin coated colloidal probe. The measurements were conducted in a controlled RH environment, varying RH from <1% in a dry nitrogen environment to about 40% in ambient air. Relative humidity (RH) and temperature were recorded by a digital hygrometer (Dwyer Instrument), the RH range is 0–100% with an accuracy of $\pm$2%, and the temperature range is $-$30–85°C with an accuracy of $\pm$ 0.5°C.

3.4 Results and Discussion

3.4.1 Intrinsic material properties of tholin and its theoretical adhesion forces

The contact angle measurements show that for water (γ =72.8 mN/m, γ^d =20.0 mN/m, and γ^p =52.8 mN/m) on a flat thin tholin film, the contact angle is 22±5°. While for diiodomethane ($\gamma = \gamma^d$ =50.8 mN/m, γ^p =0 mN/m), the contact angle is 50±5°. Thus we can solve Equations 3.9 and 3.10 for the surface energy of tholin:

$$\gamma_s = \gamma_s^d + \gamma_s^p = (34.3^{+2.7}_{-2.9} + 36.6^{+3.7}_{-3.8})\ mN/m = 70.9^{+4.6}_{-4.8}\ mN/m \tag{3.11}$$

The contact angle between heptane and tholin is less than <5°.

From the indentation part of the force curve, we get an elastic modulus (E) of tholin film of about 3.0±0.7 GPa (Equation 3.8), which is consistent with hard polymers like PMMA and polystyrene (Israelachvili, 2011). Using the measured surface energy of tholin γ_s =$70.9^{+4.6}_{-4.8}$ mN/m and its elastic modulus E, we can calculate the elasticity parameter λ for an AFM tip or a particle with radius R touching a flat tholin surface:

$$\lambda = \frac{2.06}{\zeta_0}\left(\frac{R\gamma_s^2}{\pi K^2}\right)^{1/3} \approx 891 R^{1/3}. \tag{3.12}$$

For the tholin particles investigated in this study (both the particle and the coated colloidal particle), R≈10 μm, thus we get λ ≈19, which makes the JKR model most appropriate for this system. The theoretical adhesion force under

dry conditions for particle-flat surface system can then be calculated as:

$$F = \frac{3}{2}\pi R^* W_A = 6.7 \pm 0.3\ \mu N. \tag{3.13}$$

For two tholins particle of similar size (R≈10 μm), the adhesion force is half of the adhesion force for particle-flat system (3.3±0.2 μN), since the radius R* is halved for this system.

If particles are exposed in humid terrestrial conditions (water, γ_L =72.8 mN/m), the adhesion forces start to become capillary dominated:

$$F = 4\pi R^* \gamma_{water} cos\theta_{water} = 8.5 \pm 0.3\ \mu N \tag{3.14}$$

If the condensed liquid is liquid methane (γ ≈20 mN/m, Baidakov et al., 2013) as on Titan, then the adhesion forces become:

$$F = 4\pi R^* \gamma_{methane} cos\theta_{methane} \approx 2.5\ \mu N, \tag{3.15}$$

here we use the contact angle between tholins and heptane (θ<5°), leading to cosθ =0.996 to 1, which is consistent with the value used in Lavvas et al. (2011), cosθ ∼0.995 between tholin and methane. This value is derived from the experimental results of methane adsorption on tholin films produced in a different laboratory (Curtis et al., 2008).

As RH increases, the particles transition from solid-solid interaction to capillary interactions; there might be a gradual transition for the force (e.g. Christenson, 1988). The capillary condensation that occurs around surface contact sites grow with increasing RH until a liquid film surrounds the macroscopic contact. This transition continues until the capillary meniscus radius

exceeds the asperity size, then the interparticle forces are dominated by capillary forces as shown in Equation 3.5 (McFarlane & Tabor, 1950).

It is interesting to notice that the theoretical interparticle force would actually decrease with increasing liquid methane humidity since the capillary force for liquid methane is lower the van der Waals force under dry conditions. However, if the particles have significant roughness, rather than being perfect spheres, then the van der Waals forces at low humidity would be much smaller. In this case they may be lower than the liquid methane capillary forces, which depend on the capillary radius.

For comparison, the gravity force for the 20 μm size particle is only about 2.9×10^{-6} μN to 8.2×10^{-6} μN on Titan, using the density range from 500–1400 kg/m^3 (Imanaka et al., 2012; Hörst & Tolbert, 2013; He et al., 2017). If the above calculation is done for a tholin particle of radius 100 μm (assuming a perfect smooth sphere, which is almost certainly not true for real sand particles on Titan), the contact force is a huge 67 μN (JKR still applies for tholins of this size), the methane capillary force is 25 μN, while the gravity force is only 2.9×10^{-3} μN to 8.2×10^{-3} μN. Since the gravity forces for the sand particles on Titan are so small, the interparticle forces dominate the movement of particles on Titan.

3.4.2 Tip to Flat Surfaces Adhesion Forces

Shown in Figure 3.4 are three retraction force curves of a silicon tip (tip radius about 10 nm) to three kinds of flat surfaces: quartz, tholin, and the flat side of a walnut shell particle (800 μm). The differences of the adhesion forces are

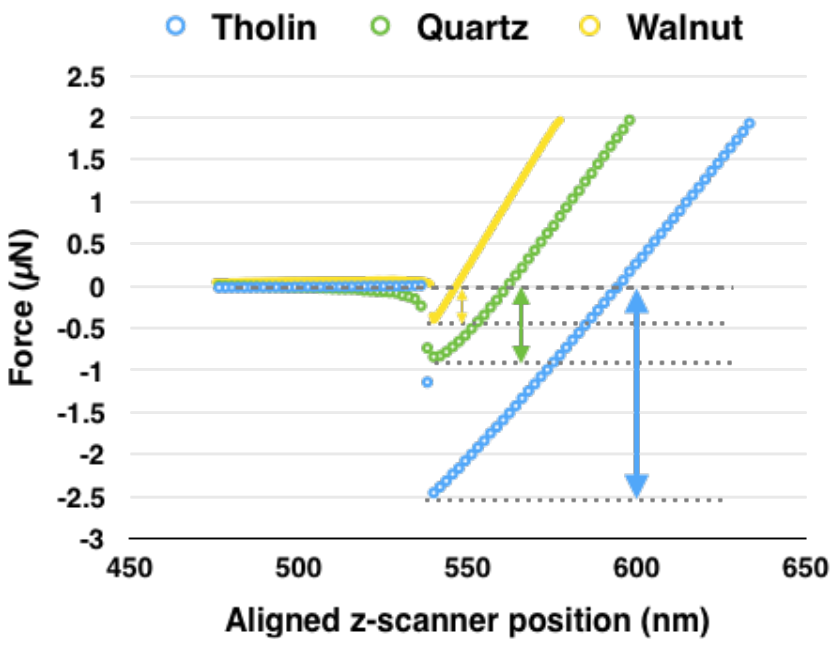

Figure 3.4: Retract force curves of a silicon tip to three different flat films, tholin (blue), quartz (green), and the flat side of a 800 μm walnut shell (yellow). The maximum pull-off forces are given by the forces at the minimum.

stark between these films. Here the adhesion force is smallest between tip and the flat surface of the walnut shells, about 0.3 μN, while the adhesion force between silicon tip and tholin film is almost 10 times larger, about 2.4 μN. The adhesion force between silicon tip and quartz film is in between, about 0.8 μN.

3.4.3 Particle to Particle Adhesion Forces

To directly study interparticle cohesion, we attached tholin and walnut particles to the end of the AFM cantilever. The force curves between particles are more complicated since the particles are usually very rough at both micro- and nano- scales, and are not uniformly spherical. We observed multiple

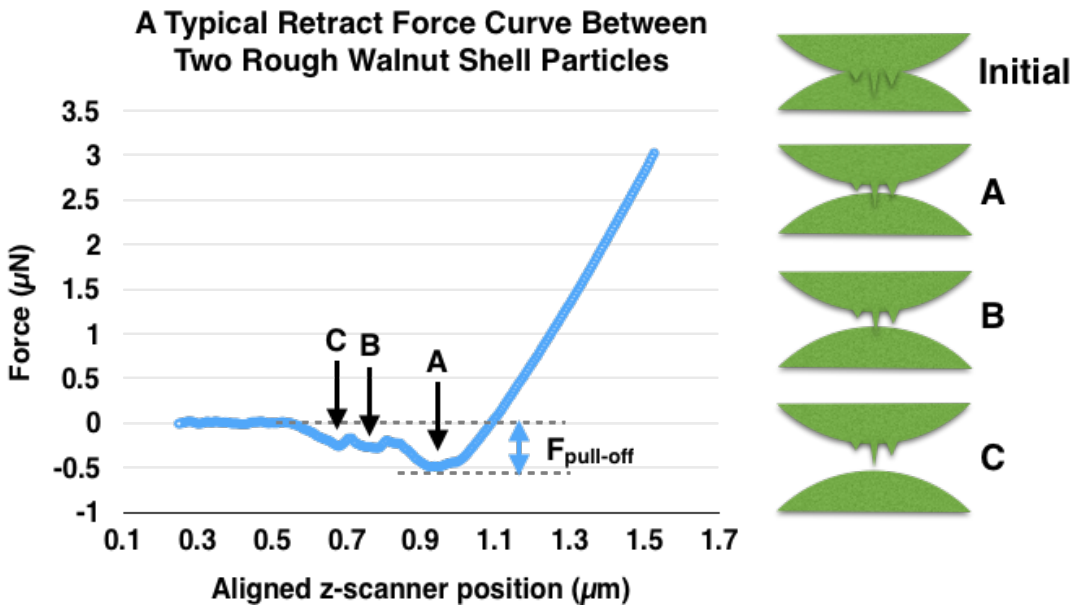

Figure 3.5: On the left is a typical retract force curve between two rough walnut shell particles. Multiple pull-off events (three here in this figure marked as A, B, C) were observed. The total pull-off force is the maximum attraction force ($F_{pull-off}$) shown in the figure. For this specific force curve, $F_{pull-off}$=0.5 μN. On the right is an illustration of the three pull-off events due to three different micro- and nano- scale roughness on the surface.

pull-off events in our experimental data for some of the very rough particles. An example of a retract force curve between two rough walnut shells particles is shown in Figure 3.5. The pull-off force is given by the maximum attraction force as that force is sufficient to pull off all the asperities (Beach et al., 2002). Since we cannot control the surface of the particles used in the wind tunnel, the roughness of the particles will usually lead to high standard deviations in pull-off force measurements because the contact area in every force curve may be different. However, this range of measured values likely represents the actual range of interparticle forces for the wind tunnel experiments.

In Table 3.1 and Figure 3.6 we show the results of particle-particle adhesion forces for walnut shells and tholins. According to JKR and DMT contact mechanics (Johnson, Kendall, & Roberts, 1971; Derjaguin, Muller, & Toporov, 1975), the adhesion forces scale linearly to the particle size. However, measurements show that the smaller 30 μm tholin particles actually show larger adhesion forces (average 0.8$\pm$0.6 μN) compared to the bigger 100 μm walnut shells (average 0.4$\pm$0.1 μN), even under lower humidity (RH$\approx$15% for tholin measurements and RH$\approx$50% for walnut shell measurements). This is likely caused by the combined effect of micro and nano surface roughness (walnut shell particle roughness (RMS)$\approx$ 70 nm vs 20 nm for tholin particles) and surface energy (γ_{tholin} $\approx$70.9 mN/m and $\gamma_{walnut\ shell}$ $\approx$30-50 mN/m, de Meijer et al., 2000). This indicates when calculating the threshold wind speed on Titan, we may need to increase the γ or β values in Equation 3.7 for Titan sand to accommodate its larger interparticle cohesion. We may also need to incorporate the variability of the measured adhesion forces (caused by surface roughness), shown in Figure 3.6 into the threshold model by using a probabilistic distribution of interparticle forces, as suggested by Yang et al. (2004). The large particle-particle adhesion forces of tholin also suggest they are easier to coagulate to form larger particles, and this may provide insight on how the small aerosol particles in Titan's atmosphere are transformed to large sand-sized particles on Titan's surface, if that is indeed the sand formation mechanism. The higher cohesion of tholin particles may also support the alternative formation mechanism of Titan's linear dunes, where Rubin and Hesp (2009) suggests that only unidirectional wind is needed for strong-cohesive sand to form longitudinal dunes.

Table 3.1: Adhesion forces between different particles

.

Particle Name	Size (μm)	Surface	Adhesion (μN)	Std. Dev. (μN)	RH range (%)
Walnut Shell	125	Walnut Shell Particle A	0.3	0.1	50.1–57.0
		Walnut Shell Particle B	0.4	0.1	
Walnut Shell	125	Walnut Shell Film	0.5	0.3	50.1–57.0
Tholin	30	Tholin Particle A	0.6	0.4	14.7–15.9
		Tholin Particle B	0.5	0.1	
		Tholin Particle C	1.5	0.6	
Tholin	30	Tholin Coated Surface	6.7	5.1	14.7–15.9
Tholin Coated Colloid	20	Tholin Coated Surface	2.9	1.2	44.3–50.7
			1.2	0.6	23.8–24.3
Tholin Coated Colloid	20	Tholin Coated Surface N_2 Enclosed–Location 1	2.6	0.1	1.7–1.9
			2.9	0.1	5.9–6.3
			3.1	0.1	10.3–10.5
			3.1	0.1	20.0–20.2
			3.3	0.1	29.8–30.0
			5.0	0.2	35.0–35.3
			5.3	0.3	39.6–40.0
Tholin Coated Colloid	20	Tholin Coated Surface N_2 Enclosed–Location 2	2.2	0.1	0.8–1.0
			3.9	<0.1	5.7–5.9
			3.2	0.1	11.0–11.2
			5.1	0.2	20.2–20.5
			5.1	0.1	30.3–30.6
			6.5	0.2	40.7–40.9

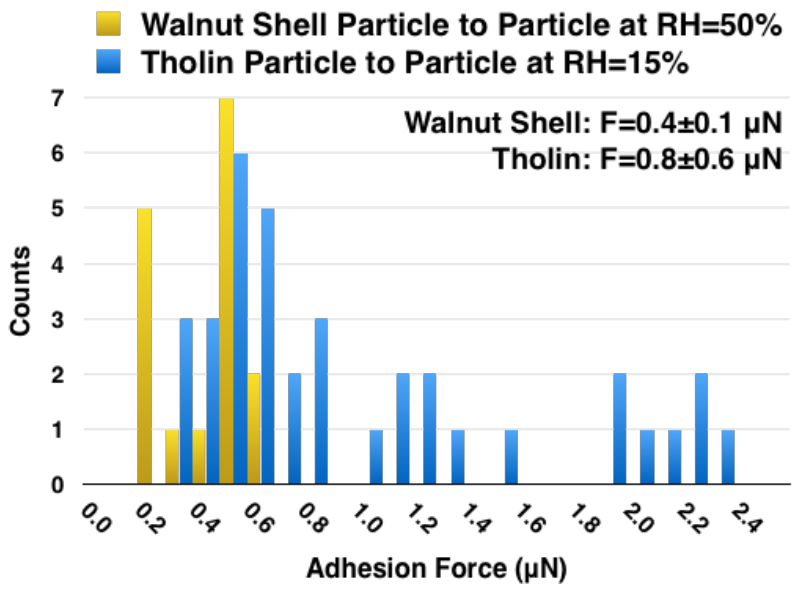

Figure 3.6: Histograms of adhesion forces between walnut shell particles (under RH of about 50%) and tholin particles (under RH of about 15%). Histograms were used to better characterize the range of the measured interparticle forces.

3.4.4 Adhesion Forces of a Tholin Coated Sphere to Flat Tholin Surfaces

To further investigate the effect of humidity on adhesion forces, we changed the AFM experimental setup to the configuration shown in Figure 3.3d. Instead of measuring the interaction between two irregularly shaped tholin particles, we used a tholin-coated spherical particle and a flat tholin film. This allows us to reduce the effect of surface roughness and focus on the effect of RH on adhesion forces.

We first obtain forces curves with the tholin-coated particle on different positions of a tholin film at two different RH values, RH=25% and RH=50%. The distribution of pull-off forces is shown in Figure 3.7 and the values are also summarized in Table 3.1. The standard deviation of the measurements is

generally large, likely due to the differences in surface roughness between the positions. However, even with the measured standard deviation, the adhesion force differences between the two RHs are significant: at RH=50%, the measured adhesion forces are almost double the adhesion forces at RH=25%. This suggests that the adhesion forces between tholin particles are strongly affected by water vapor in air.

Since there is very little water vapor in Titan's atmosphere, we want to know the adhesion forces for tholin under dry conditions. To do that, we enclosed the entire AFM system in a dry nitrogen glove bag and again measured the interaction force between a tholin coated colloidal probe and a tholin surface. We also measured the adhesion forces as the RH was increased, which are shown in Figure 3.8. The adhesion forces are still strong under very low RH (RH<1%), at around 2–2.5 μ N. The forces are lower than the theoretical adhesion forces under dry conditions, 6.7 μN (see Equation 3.13), which is likely due to nanoscale surface roughness on the coated tholin surfaces (roughness (RMS)$\approx$1 nm for tholin film). As RH increases, the adhesion gradually increases until ambient humidity (RH=40–50%). This is consistent with the behavior of a hydrophilic surface (Jones et al., 2002), which can be explained by the existence of abundant polar molecules in tholins (He et al., 2012; He & Smith, 2014b). The theoretical maximum capillary force (Equation 3.14) for water vapor is shown as the dashed line in Figure 3.8; the extended linear fit to the data would reach this force at around RH=70–80%. If we assume the forces would change from pure van der Waals contact force to capillary forces for different liquid methane humidities, similar to water, we can draw

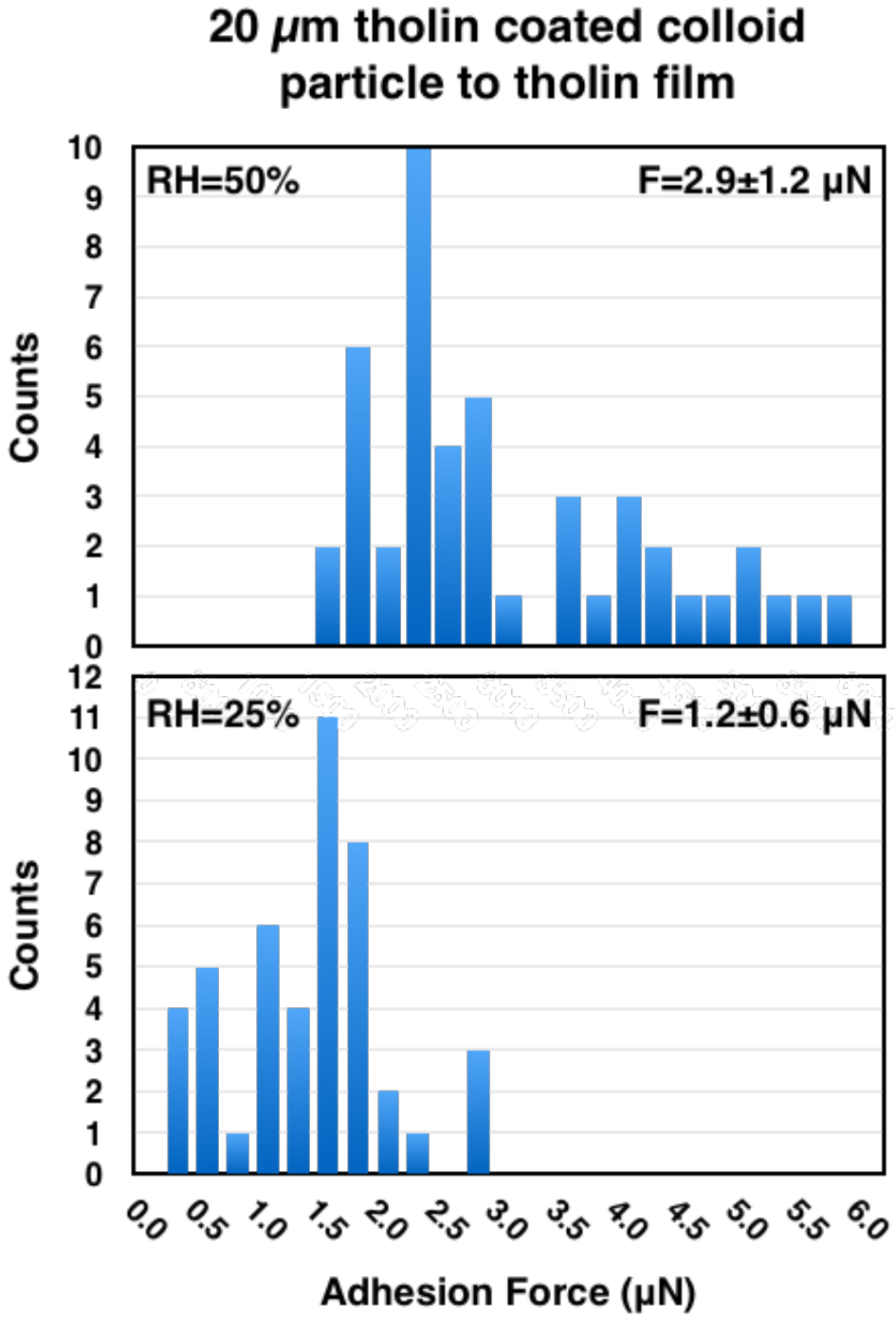

Figure 3.7: Histograms of adhesion forces for tholin coated 20 μm colloid probe to tholin film at RH=50% and 25%.

an imaginary Force–RH trend line for the forces to reach to full capillary forces (liquid methane, Equation 3.15) with liquid methane humidity increasing. As discussed in Section 5.1, because of the surface roughness of real particles, the van der Waals force under dry conditions is lower than theoretical calculations. Thus our results suggest that with increasing liquid methane humidity, the interparticle forces will actually increase. One major limitation on our understanding is that contact forces are strongly affected by surface roughness, and we do not currently know roughness of the sand particles on Titan. Future missions to the surface are required to assess this important parameter.

Temperature may also play a role in adhesion forces. First, as temperature decreases, the surface tension of the liquid decreases, thus decreasing the capillary forces. Second, if the substance is close to its melting point, a quasi-liquid layer could cause additional capillary forces. Then as the temperature decreases away from the melting point, the adhesion forces would drop because the capillary forces decrease or disappear. The measured surface tension of liquid methane is $\sim$20 mN/m at Titan's surface temperature (Baidakov et al., 2013). We used this value to make theoretical predictions of capillary forces for liquid methane (Equation 3.15). Tholin is a stable solid at room temperature ($\sim$300 K), and tholins do not appear to melt to temperatures of at least $\sim$350 K (He & Smith, 2014a). Thus room temperature measurements should not be affected by the potential additional capillary forces formed by the quasi-liquid layers resulting from melting, and the adhesion forces under 94 K should be similar to the forces at room temperature.

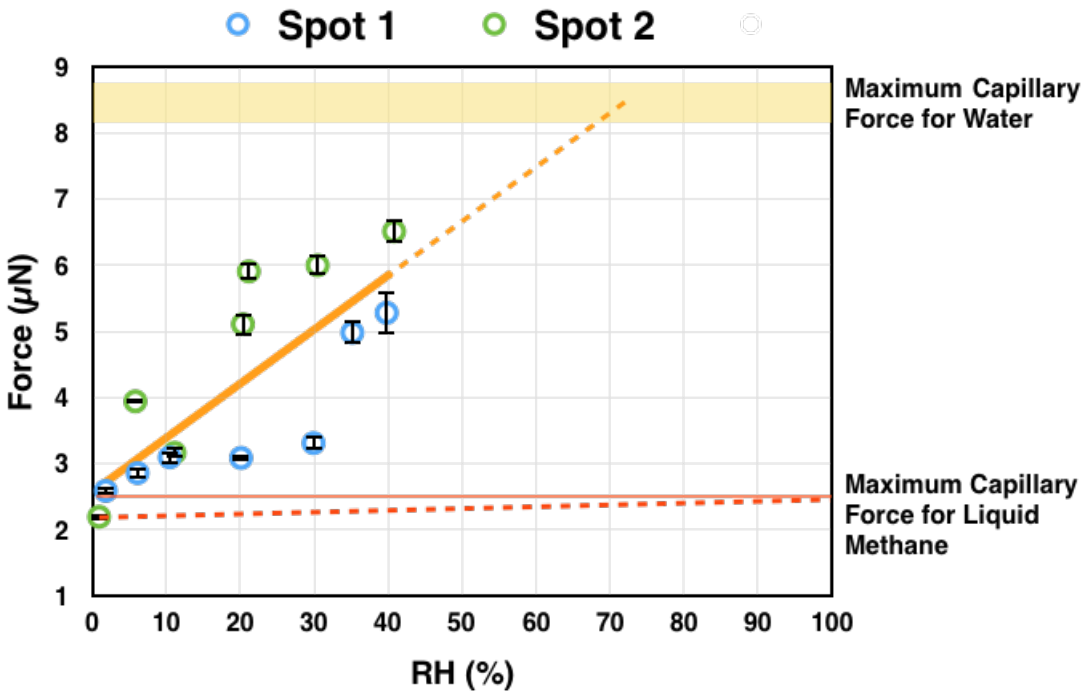

Figure 3.8: Shown here are the adhesion forces vs relative humidity (RH) of water between tholin coated sphere and a flat tholin surface. Blue circles and green circles were obtained at two different locations on the tholin film. The solid orange line shows a linear fit to the data for both locations. The orange stripe corresponds to the theoretical capillary force (including error bars) for water vapor (see Equation 3.14), and the red thin stripe corresponds to the theoretical capillary force for liquid methane vapor (including error bars also, see Equation 3.15). The orange dashed line and the red dashed line show the extrapolated force-RH relationship for water and for liquid methane, respectively.

3.5 Conclusion

This study performed the first direct measurements of adhesion forces between tholin particles. It indicates that the threshold wind speed on Titan could be larger than reported in Burr et al., (2015), since the interparticle forces between tholin particles are much larger than walnut shells used in the TWT. Measurements of the adhesion between a tholin coated colloidal probe and a flat tholin surface show a significant adhesion force even under Titan conditions (with no water vapor), which also indicates that the small Titan aerosol particles ($\sim$1 μm) could coagulate efficiently into larger sand-sized particles. The high cohesiveness of tholin may also support the alternative formation mechanism of Titan's dunes, where only unidirectional wind is required with cohesive sediment to form longitudinal dunes on Titan.

Chapter 4

Where does Titan Sand Come From: Insight from Mechanical Properties of Titan Sand Candidates

4.1 Introduction

Across the Solar System, many planetary worlds have aeolian processes despite the wide variety of environmental conditions present on these bodies. These bodies include: Venus, Earth, Mars (Greeley & Iversen, 1985), Titan (Lorenz et al., 2006), Neptune's moon Triton (Smith et al., 1989), Pluto (Telfer et al., 2018), and possibly comet 67P/Churyumov-Gerasimenko (Thomas et al., 2015). Other than the environmental conditions, the aeolian processes on icy bodies (Titan, Triton, and Pluto) differ from those on terrestrial bodies (Venus, Earth, and Mars) because of the differences in the dune-forming materials. On terrestrial bodies, the materials that get transported are mainly silicate sand (weathering and erosion products of silicate rocks), while the materials that are transported on icy bodies could be different. For example, the wind streaks on Triton are possibly composed of dark complex hydrocarbons (Smith

et al., 1989), the dunes on Pluto are made of methane ice (Telfer et al., 2018), and the ripples and wind tails on comet 67P could be made of organic-rich materials associated with opaque minerals on the surface (Capaccioni et al., 2015). On Titan, the dune-forming materials are most likely organics produced by photochemistry in the atmosphere (Soderblom et al., 2007; Hörst, 2017) or abundant ices that form the crust of Titan. Silicate sand is known to have high resistance to abrasion due to its hardness (Mohs hardness around 6 to 7), which might be the reason that it can be transported for long distances without being abraded to dust (Bagnold, 1941). However for icy bodies like Titan, we do not know the basic mechanical properties of the organic sand or ice on the surface, so we cannot infer its transport capabilities.

Titan's sand particle sizes are first estimated to be around 100–300 μm based on calculation of the optimum particle diameter range that results the minimum threshold wind speed on Titan (Lorenz et al., 2006). Lorenz (2014) suggests that plausibly decreased particle density or increased cohesion between particles could lead to higher optimum diameter up to around 500–600 μm; Yu et al., (2017a) did find the cohesion forces of tholin larger than those of silicate sand and materials used in the Titan Wind Tunnel. Burr et al., (2015) modified the threshold friction speed function using experimental results in the Titan Wind Tunnel and they found an optimum diameter around 200–300 μm. All those previous studies indicate that the size of the Titan sand particles should be on the order of hundreds of microns. So it is a puzzle how the small aerosol particles produced in Titan's atmosphere (up to 1 μm, Tomasko et al., 2005) are transformed into these large, sand-sized particles

on Titan's surface (Soderblom et al., 2007). Barnes et al. (2015) proposed four mechanisms for the transformation: sintering, lithification and erosion, flocculation, and evaporation. The sintering and lithification and erosion mechanisms could happen in subaerial conditions while the flocculation and evaporation need subaqueous environments. However, current lakes and seas on Titan are mainly at high latitudes while the longitudinal dunes are thousands of kilometers away in the equatorial region. Thus, if sand particles on Titan were produced in the current lakes and seas by subaqueous mechanisms, they need to be mechanically strong enough to travel long distances to the equator.

Therefore, it is important to quantify the mechanical behaviors of Titan sand analog materials so that we can better understand the origin of Titan sand particles and their transportation capacities. Laboratory-produced Titan aerosol analogs (so-called "tholins") could be compositionally similar to Titan sand (Barnes et al., 2015; Yu et al., 2017a), but are usually produced in low yields (Cable et al., 2012) and thus are difficult to quantify mechanically using macroscopic approaches. This makes nanoindentation an ideal method to quantify the mechanical behaviors of the thin tholin films. Nanoindentation is a technique that uses small loads (on the order of mN) and small tip size (tip radius on the order of 100 nm), resulting in a nanometer scale indentation area, and is used widely for quantifying mechanical properties of small volumes of materials.

Evaporites are also possible candidate materials for Titan sand (Barnes et al., 2015). Titan's evaporites may be made of acetylene, ethylene or butane

(Cordier et al., 2013, 2016; Singh et al., 2017), however, these materials are not stable solids under room temperatures on Earth, and their solid mechanical properties also have not been measured under low temperatures.

Another possible candidate for Titan sand is water ice. Even though the dune-making materials on Titan appear to be dominated by a spectrally "dark brown" organic unit in Cassini's Visual and Infrared Mapping Spectrometer (VIMS) data, with little water ice "dark blue" spectral signature (Soderblom et al., 2007; Barnes et al., 2008), it cannot be ruled out that the individual sand particles are water ice grains coated with a thin layer of organics because the infrared penetration depth is at most tens of microns (Barnes et al., 2008).

Kuenen (1960) found that various mechanical properties are involved in mechanical abrasion in aeolian and aqueous transport. For relatively soft materials, the dominant abrasion mechanism is "grinding" (where hardness of the material dominates); in this case, a change of grain size or wind speed would not substantially affect the abrasion rate. While for relatively hard materials like quartz, its brittleness makes "chipping" (or "spalling") the dominate mechanical abrasion mechanism under aeolian transport (when impacts dominate over direct fluid drag). "Chipping" of quartz grains slows down with increasing roundness, decreasing grain size, and decreasing wind speeds. While in aqueous transport, where impacts are minimal, quartz erodes very slowly because of its high hardness. Thus it is important to characterize both the mechanical hardness and brittleness of Titan sand analogs, so that we can better assess aeolian versus fluvial transportation on Titan.

The materials and nanoindentation methods are described in Section 2.1–2.2. In Section 3.1, we compare the measured elastic modulus and hardness of various materials. Measured fracture toughness of selected materials are compared in Section 3.2. We discuss the extrapolation of mechanical properties of tholin from room temperature to Titan's surface temperature in Section 4.1. Finally, we list all the possible candidate materials for Titan sand and discuss their capability of transportation on Titan in Section 4.2.

4.2 Methods

4.2.1 Materials and Preparation

We used a variety of analog materials, both lab-created and naturally found, in order to simulate materials being transported on both terrestrial and icy bodies. We used a few natural sands on Earth, including silicate beach sand, carbonate sand, and white gypsum sand as terrestrial sand analogs.

For Titan, we used both the laboratory produced tholin (He et al., 2017) and some simple solid organic materials as analog materials. Tholin was produced using the Planetary HAZE Research (PHAZER) experimental system at Johns Hopkins University, with a 5% CH_4/N_2 cold gas mixture (around 100 K) in a glow plasma discharge chamber (pressure: 3 Torr, flow rate of gas mixture: 10 sccm, He et al., 2017). The produced tholin simulates the aerosol on Titan and is mixture of complex organic compounds.

Different types of simple organics were used to simulate simple atmospheric condensates and /or evaporites on Titan. Titan's evaporites could be made of acetylene, ethylene, or butane (e.g. Cordier et al., 2013). Since

we are measuring the materials under room temperature, we chose the following simple organics since they are stable solids under room temperature. Some of the following organics may exist in Titan's atmosphere and some are identified in tholin samples before. Three polycyclic aromatic hydrocarbons (PAHs) made of different numbers of fused benzene rings are used: naphthalene (two rings, possibly present in Titan's upper atmosphere, Waite et al., 2007), phenanthrene (three rings, its mass peak, ~170 amu, possibly present in Cassini Plasma Spectrometer data, Waite et al., 2007), and coronene (six rings). One polyphenyl, biphenyl, made of two non-fused benzene rings, was also used to compare with naphthalene (two fused benzene rings). Two nitrogen-containing organics, adenine and melamine, both of which have been identified in tholin samples from a different experimental setup (Hörst et al., 2012, He & Smith, 2013, 2014a, b) were used to test the effect of nitrogen inclusion on the mechanical properties of simple organics.

We also investigated analog materials used in planetary wind tunnels (Yu et al., 2017b), including chromite, basalt, quartz sand, glass beads, gas chromatograph packing materials (called GC), activated charcoal, instant coffee, walnut shells, and iced tea powder.

All the above materials are also summarized in Table 4.1.

Tholin was deposited as a thin homogenous film on mica discs (10 mm diameter). The film is very smooth (RMS roughness is ~1 nm, measured by Atomic Force Microscopy, AFM) and has a thickness of approximately 1.3 μm. We also collected tholin particles from the chamber wall in a dry N_2 glove box (O_2<1 ppm, H_2O<1ppm).

The laboratory-produced tholin film is used directly for the measurements. In contrast, the collected tholin particles and other material particles (Table 4.1) needed to be mounted and polished before measurement. The procedure for preparing the particles is as follows: the particles were embedded in an epoxy matrix using a vacuum mounting system in cylinder sample stubs (1.25" diameter). The samples were cured in ambient atmosphere overnight, resulting in a composite of particles in a hardened epoxy matrix. The samples were then polished to obtain a smooth surface for nanoindentation. For water insoluble materials, the samples were polished using a Tegramin-20 Sample Polisher. The finest polishing size was 40 nm using non-drying colloidal silica suspension. For water soluble materials, we used hand polishing; the finest grain size was 3.5 μm with 7000 grit silicon carbide paper.

4.2.2 Nanoindenter and Tips

We used an iNano Nanoindenter (Nanomechanics, Inc.) for the elastic modulus, hardness, and fracture toughness measurements. The instrument has a maximum load of 50 mN, with a load resolution of 3 nN and a displacement resolution of 0.02 nm. A grid of points on the material were indented and each time the instrument recorded a load-displacement curve. During each load–displacement cycle, the applied load will stop increasing when the maximum load or the maximum penetration depth is reached. We performed all the measurements under room temperature, and then estimated the result for tholin under Titan's surface temperature (94 K).

We used a three-sided pyramidal-shaped Berkovich tip, made of single

Table 4.1: Summary of materials used in this study. Basalt is acquired from Pisgah crater and only two major compositions are shown in the table marked with *. Its detailed composition can be found in Friedman (1966). GC indicates gas chromatograph packing materials. GC pink is diatomite, while GC tan is calcined diatomite, it has a different color compared to GC pink (see also Burr et al., 2015; Yu et al., 2017a).

Material Category	Material Name	Structure
Titan sand analogs	Tholin	$C_xH_yN_z$
	Naphthalene ($C_{10}H_8$)	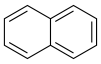
	Biphenyl ($C_{12}H_{10}$)	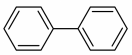
	Phenanthrene ($C_{14}H_{10}$)	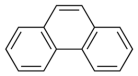
	Coronene ($C_{24}H_{12}$)	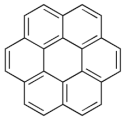
	Adenine ($C_5H_5N_5$)	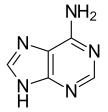
	Melamine ($C_3H_6N_6$)	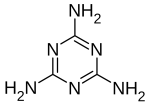
Natural sand	Silicate beach sand	mainly SiO_2
	Carbonate sand	mainly $CaCO_3$
	White gypsum sand	mainly $CaSO_4 \cdot 2H_2O$
Materials used in planetary wind tunnels (e.g., Titan Wind Tunnel, TWT; Martian Surface Wind Tunnel, MARSWIT, etc.)	Chromite	mainly (Fe, Mg, Al)Cr_2O_4
	Basalt	mainly SiO_2, $Al_2O_3^*$
	Quartz sand	mainly SiO_2
	Glass beads	mainly SiO_2
	GC pink	mainly modified SiO_2
	GC tan	
	Activated charcoal	mainly C
	Instant coffee	n/a
	Walnut shells	n/a
	Iced tea powder	n/a

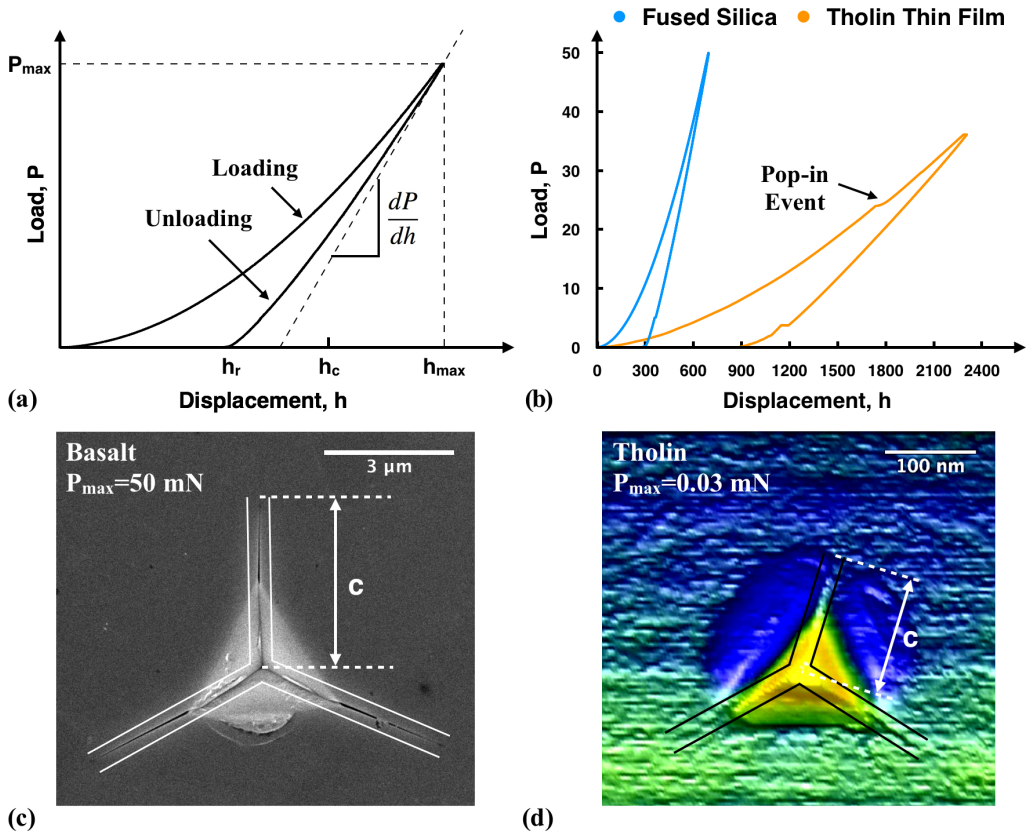

Figure 4.1: (a) A schematic representation of load (P)–indenter displacement (h) curve in a nanoindentation experiment, where P_{max} is the maximum load, h_{max} is the maximum displacement at peak load, h_c is the depth of contact at peak load, and h_r is the residual depth of contact impression after unloading. (b) A comparison between the load–displacement curves of fused silica and tholin thin film with a Berkovich indenter. In the load–displacement curve of tholin, a "pop-in" event occurs during loading indicating a fracture event. (c) An SEM image showing cracks generated on a basalt grain after nanoindentation using a cube-corner tip. The maximum load is 50 mN and the crack length is denoted as c. (d) An AFM topographic image showing cracks generated on a thin tholin film with a maximum load of 0.03 mN using a cube-corner tip, the crack length is denoted as c.

crystal diamond (Micro Star Technologies), for measuring the hardness (H) and Young's modulus (E) of the materials. A schematic representation of a load (P) – displacement (h) curve for measuring elastic modulus and hardness is shown in Figure 4.1(a).

The hardness (H) is given by:

$$H = \frac{P_{\max}}{A},$$

where P_{max} is the peak load and A is the projected area of contact at peak load. For a Berkovich tip, A can be written as:

$$A = 24.56 h_c^2,$$

where h_c is the depth of contact. It is related to the maximum indentation depth h_{max}, the stiffness S, and the maximum load P_{max}:

$$h_c = h_{\max} - \epsilon \frac{P_{\max}}{S},$$

where ϵ is the geometric constant for the indenter; for a Berkovich tip ϵ=0.72 (Oliver & Pharr, 1992).

The reduced elastic modulus, E_r, is related to the stiffness S, which can be obtained from the unloading portion of the load–displacement curve:

$$S = \frac{dP}{dh} = \frac{2}{\sqrt{\pi}} E_r \sqrt{A}.$$

The elastic modulus of the sample (E_s) can then be obtained from the reduced modulus:

$$\frac{1}{E_r} = \frac{1 - {\nu_s}^2}{E_s} + \frac{1 - {\nu_i}^2}{E_i},$$

where E_i is the elastic modulus of the tip, and ν_s and ν_i are the Poisson's ratios of the sample and the tip.

To obtain a higher accuracy of elastic modulus and hardness, we performed dynamic indentation (further described in Oliver & Pharr, 2004) through each load-displacement cycle. A small harmonic oscillation was superimposed on the applied static load so the instrument could continuously measure elastic modulus and hardness as a function of displacement. Here we use the constant-strain-rate (CSR) method by applying a constant loading rate over the applied load, which approximates a constant strain rate of 0.2 s^{-1}.

Before and after a set of measurements for our samples, fused silica, a commonly used nanoindentation reference material (with a Young's modulus of 72 GPa), was tested to calibrate the area function of the tip. The hardness and elastic modulus were calculated by the software using Oliver and Pharr (1992) method based on the calibration data and the load–displacement curves.

Since we use dynamic indentation to obtain elastic modulus and hardness continuously as a function of displacement, the actual modulus and hardness value were taken as the average values over a certain indentation depth range. This depth range depends on the surface effect and the effect of the substrate. Generally the indentation average depth is greater than 50 nm to eliminate the effect on the topmost surface caused predominately by surface roughness. For bulk materials, hardness and elastic modulus are independent of indentation depth so the average depth can be taken for any depth range larger than 50–100 nm. For the tholin thin films (thickness around 1.3 μm) deposited on a hard mica substrate, the substrate effect starts to show up over an indentation

depth of 15% of the film thickness (e.g., Hay & Crawford, 2011), where the modulus and hardness values start to increase with increasing indentation depth. Here the depth range for reporting the modulus and hardness values is selected to optimize the material response of interest and minimize the surface and substrate effects (for tholin, the average depth range is 100–150 nm).

We used a much sharper cube corner tip, which has a higher aspect ratio than a Berkovich shaped tip, for measuring fracture toughness. With a half angle of only 35.3° (compared to 65.3° for a Berkovich tip), the use of a cube-corner tip can significantly reduce the cracking threshold of brittle materials (Harding et al., 1995). It is also made of single crystal diamond (Micro Star Technologies). When brittle materials are indented with the sharp cube-corner tip, radial cracks are generated. We varied the maximum indentation loads from 0.03 to 50 mN to measure the fracture toughness of our samples. After the indentations, we used a Bruker Dimension 3100 AFM or an SEM (scanning electron microscopy, JSM-6700F, JOEL Ltd.) to image the indentation and the associated cracks. An example is shown in Figure 4.1(c). The fracture toughness calculations were developed by Lawn et al., (1980) and Anstis et al., (1981):

$$K = \alpha(\frac{E}{H})^{0.5}(\frac{P_{\max}}{c^{3/2}}),$$

where α is an empirical constant that depends on the geometry of the tip; for a cube-corner tip, α =0.036 (Harding et al., 1995). The crack length, c, can be determined by microscopic imaging methods. The fracture toughness test of the reference material, fused silica, was measured to be 0.58±0.09 MPa·m$^{1/2}$, which is consistent with the literature value (Harding et al., 1995).

When measuring fracture toughness on tholin thin film deposited on mica substrate, if the indentation depth is over 10% of the film thickness, the elastic-plastic deformation zone and crack growth may extend to the substrate and affect the accuracy of measurements (e.g., Krabbe et al., 2014). Thus we indented the film at a load of only 0.03 mN, which results in a maximum indentation depth of $\sim$100 nm, smaller than 10% of the film thickness ($\sim$130 nm). The resulting indentation and cracks are shown in Figure 4.1(d).

4.3 Results

4.3.1 Elastic Modulus and Nanoindentation Hardness

The elastic moduli and nanoindentation hardnesses of all of the materials are shown in Figure 4.2 and Figure 4.3. Tholin film has a Young's modulus of 10.4$\pm$0.5 GPa and hardness of 0.53$\pm$0.03 GPa, and tholin particles have similar values. A comparison of the load-displacement curves for tholin and fused silica (modulus 72.3$\pm$0.2 GPa, hardness 9.5$\pm$0.1 GPa) is shown in Figure 4.1(b). Tholin has smaller maximum indentation load, smaller stiffness, and larger contact area compared to fused silica, which results in smaller hardness and elastic modulus values. However, amorphous organics/polymers (tholin is an amorphous solid, Quirico et al., 2008) usually have moduli in the range of 10^{-3}–10 GPa (Meyers and Chawla, 2009), tholin's elastic modulus is on the high end, indicating its large stiffness among this type of material. This may be caused by cross-linking between molecule chains in tholin similar to network polymers (Dimitrov & Bar-Nun, 2002). The high density of cross-linking makes sliding of molecules difficult, so stretching or breaking of covalent

bonds is necessary to deform tholin.

Even though tholin is very stiff as an organic material, its elastic modulus and hardness are an order of magnitude lower than silicate beach sand (modulus $\sim$100 GPa, hardness $\sim$14 GPa) and basalt (modulus $\sim$100 GPa, hardness $\sim$9 GPa). As a mechanically weak sand on Earth, white gypsum is an example of a material that is not able to transport long distances because of its mechanical weakness and also its high solubility in water (Lorenz & Zimbelman, 2014). However, white gypsum sand has larger stiffness (37 GPa) and hardness (1.5 GPa) than tholin, as is also true for carbonate sand (modulus $\sim$74 GPa, hardness $\sim$3.7 GPa).

It is interesting to note that lots of low density wind tunnel materials have a similar elastic modulus and hardness to tholin, including walnut shells (modulus 7 GPa, hardness 0.3 GPa), GCs (modulus 16 or 9 GPa, hardness 1 or 0.5 GPa), instant coffee (modulus 8 GPa, hardness 0.4 GPa), and activated charcoal (modulus 9 GPa, hardness 0.8 GPa). Even though those materials have very different interparticle forces compared to tholin (Yu et al., 2017a, b). In contrast, the high density wind tunnel materials, quartz sand, chromite, and glass beads, have similar hardness and modulus values to silicate sand.

The PAHs and the polyphenyl we used (naphthalene, biphenyl, coronene, and phenanthrene) all have aromatic rings and are only made of carbon and hydrogen. Their indentation hardness and elastic moduli are all lower than those of tholin. The two nitrogen-containing organics we used (adenine and melamine) have been previously detected in tholin samples (Hörst et al., 2012; He & Smith, 2013, 2014a, b). Adenine has smaller elastic modulus (4.3$\pm$0.7

GPa) and hardness (0.14±0.03 GPa), while melamine has similar hardness and elastic modulus values (modulus 9.0±2.8 GPa, hardness 0.48±0.21 GPa) to tholin. This is probably because there is a larger density of hydrogen bonds in melamine than adenine, which makes the structure stronger (Sakurada & Keisuke, 1975). In addition, melamine can polymerize with agents like formaldehyde and form the one of the strongest network polymers, melamine resins (Jones & Ashby, 2011), so the existence of melamine in tholin would support tholin's highly cross-linked structure.

Previous work suggests that indentation hardness is correlated with elastic modulus (Labonte et al., 2017). Here we fit our nanoindentation hardness and Young's modulus with a power law equation, $H=0.020E^{1.34}$, $R^2=0.95$, shown in Figure 4.4. Using this relationship, we can predict the nanoindentation hardness of a material given its elastic modulus value, and vice versa.

4.3.2 Fracture Toughness

Since fracture toughness requires a highly smooth surface, we are only able to measure it for several selected materials; the results are shown in Figure 4.5. Fracture toughness is an intrinsic material property that describes the resistance of a material to failure. Materials with lower fracture toughness are more brittle. Tholin has a fracture toughness of only 0.036 $MPa{\cdot}m^{1/2}$, which is much lower than the fracture toughness of typical organic/polymeric materials (0.6–5.0 $MPa{\cdot}m^{1/2}$). The pop-in events in the loading portion of the load-displacement curve of tholin (Figure 4.1b) also indicate its brittle nature. The fracture toughness of tholin is also a magnitude lower than quartz sand

(0.89 MPa·$m^{1/2}$) and basalt (0.55 MPa·$m^{1/2}$). Thus, tholin is much more brittle than silicate sand and is more likely to break apart during transportation. This is consistent with tholin's highly cross-linked structure inferred from the elastic modulus and hardness measurements. High-density cross-linking of molecular chains will provide adequate modulus and strength, but will also lead to extreme brittleness (Meyers and Chawla, 2009). Tholin has a larger elastic modulus and smaller fracture toughness compared to a typical network polymer, epoxy (modulus 2.1–5.5 GPa, fracture toughness 0.3–0.6 MPa·$m^{1/2}$, Meyers and Chawla, 2009), this indicates tholin has much more complex cross-linking compared to regular network polymers. The simple organic we tested, phenanthrene, has a higher fracture toughness than tholin but is still much more brittle compared to silicate sand and basalt. We cannot induce cracks in walnut shell particles even with the highest load (50 mN), probably because they are very porous and ductile, so a much higher load is needed to fracture them.

4.4 Discussion

4.4.1 Temperature's Effect

Temperature generally has little effect on the mechanical properties of materials when the temperature is lower than a material's phase transition temperature. Elastic modulus and hardness increase slightly with decreasing temperature. For metals and ceramics, the elastic modulus and hardness increase approximately linearly with decreasing temperature from the melting

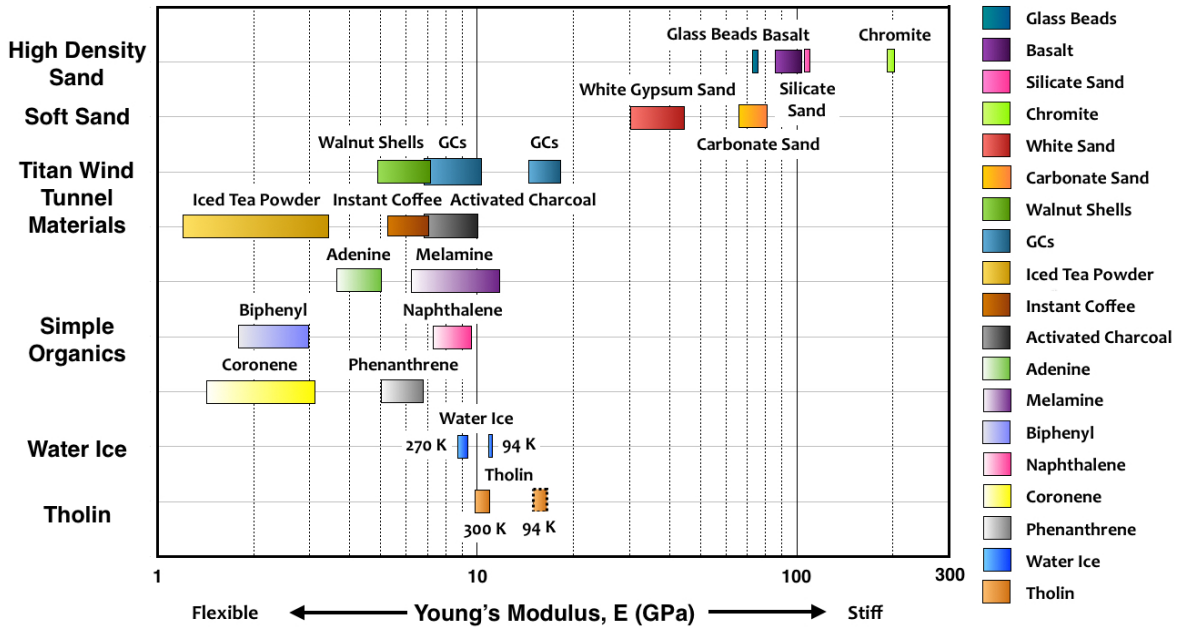

Figure 4.2: Young's modulus plot for all tested materials. The color bar includes the standard deviation from measurements for each material. Here silicate sand includes both quartz sand (a material used in wind tunnel) and natural silicate beach sand. GCs, the gas chromatography packing materials, include both GC pink and GC tan. Each GC is probably a mixture of two substances, so they each have two sets of characteristic elastic modulus values. Materials are grouped into seven categories: 1) high density materials including glass beads, basalt, silicate sand and chromite in the topmost row; 2) white gypsum sand and carbonate sand in the top second row; 3) low density wind tunnel materials, walnut shells, GCs, iced tea powder, instant coffee, and activated charcoal in the third and fourth rows; 4) nitrogen-containing organics, adenine and melamine, in the fifth row; 5) PAHs (napthalene, phenanthrene, and coronene) and the polyphenol (biphenyl) in the sixth and seventh row; 6) water ice in the eighth row, its elastic modulus under 94 K and 270 K was from the polynomial fitting in Proctor (1966); and 7) tholin in the lowest row, its elastic modulus value under ambient environment (300 K) is measured here and the value under 94 K is extrapolated in Section 4.1.

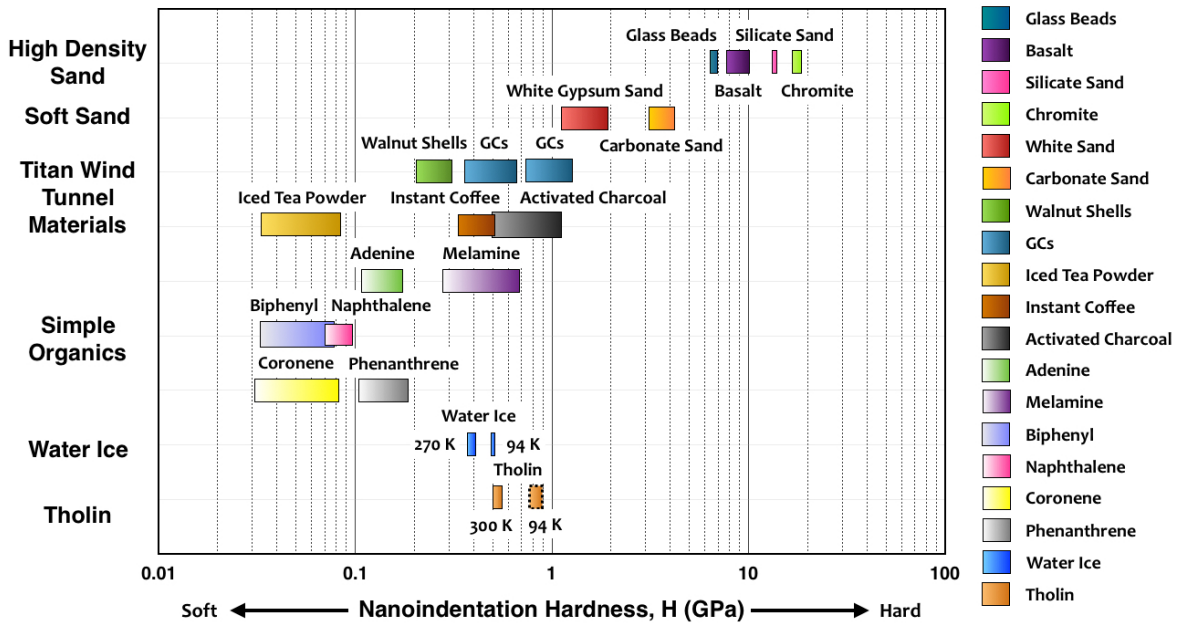

Figure 4.3: Nanoindentation hardness plot for all tested materials. The color bar includes the standard deviations from measurements for each material. GCs have two characteristic hardness values probably because each GC is a mixture of two substances. Other materials are named and grouped in the same way as Figure 4.2. For water ice and tholin at 94 K, their hardness values are predicted by using the nanoindentation hardness–modulus relationship in Figure 4.4.

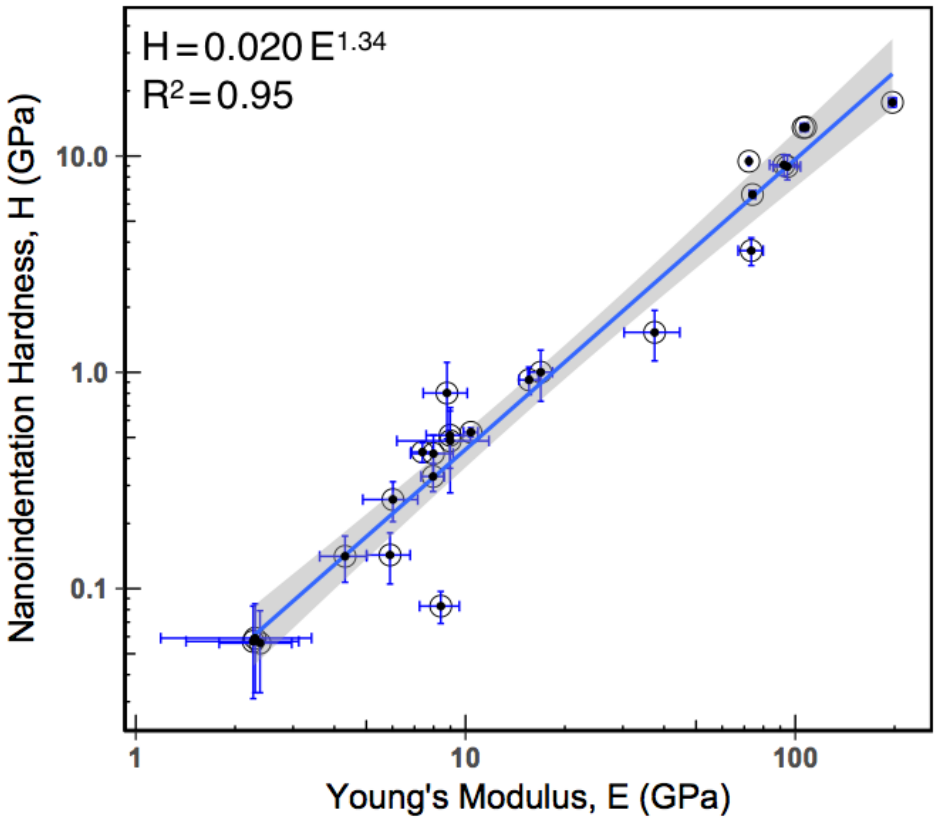

Figure 4.4: Shown here is the logarithmic nanoindentation hardness (H) versus logarithmic elastic modulus (E) values for all test materials and a fitted power law curve (blue line), where $H=0.019E^{1.37}$,$R^2=0.95$. The gray shaded area marks the 95% confidence intervals for the fitting ([0.012; 0.030] and [1.21; 1.47]).

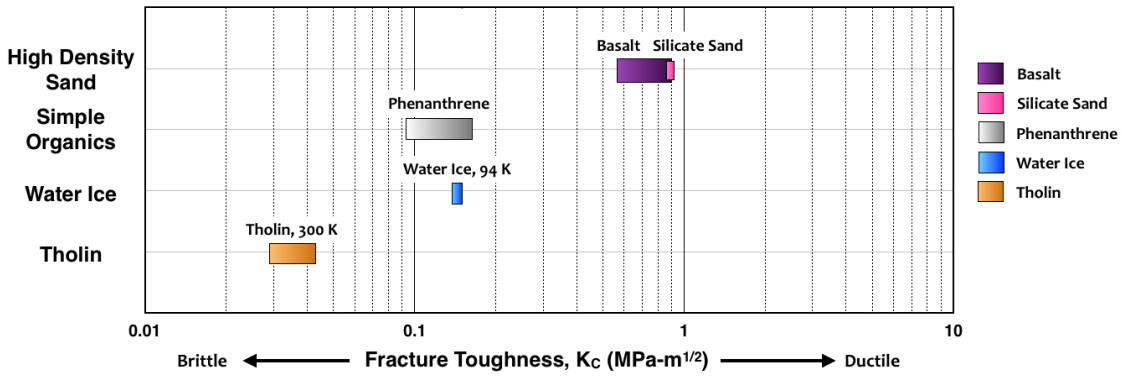

Figure 4.5: Fracture toughness plot for selected materials. The color bar includes the standard deviation values for each material. The selected materials are grouped and named the same as Figure 4.2. The fracture toughness value of water ice was adopted from Litwin et al. (2012).

temperature (T_m) (Courtney, 2000). The relationship can be expressed as:

$$E \cong E_0(1 - 0.5\frac{T}{T_m}), \tag{4.1}$$

where E_0 is the elastic modulus of the material at 0 K. With an elastic modulus value (E) at a given temperature (T), and with the material's melting temperature (T_m), using Equation 4.1, we can calculate E_0 and then estimate elastic modulus at other temperatures. For amorphous polymers, the glassy transition temperature (T_g) is a critical temperature instead of T_m (Courtney, 2000). Below T_g, polymers are in the glassy regime, have relatively high elastic modulus and hardness and are generally brittle. In this regime, Equation 4.1 holds true for most polymers, with T_g replacing T_m. While above T_g, the elastic modulus of polymers can decrease by several (3 to 4) orders of magnitude and they become rubbery, this is called the rubbery regime. Here all the experiments we performed were under room temperature (~300 K) while on Titan the surface temperature is much lower (94 K), so we need to translate

our experimental results to Titan conditions. Tholin is a stable solid at room temperature and it does not melt up to at least ∼350 K (He & Smith, 2014c). According to the fracture toughness test, tholin is very brittle and is unlikely to be in its rubbery regime. Here we use the critical temperature T_g or T_m =350 K for tholin in Equation 4.1. With the measured modulus value at a temperature of ∼300 K, we can estimate the modulus of tholin at 94 K to be around 16 GPa (15.73±0.79 GPa), shown in Figure 4.2. Using the fitted linear relationship between the elastic modulus and the nanoindentation hardness in Figure 4.4, the nanoindentation hardness for tholin at 94 K can be estimated to be around 0.8 GPa (0.83±0.06 GPa), and is then plotted in Figure 4.3. The brittleness of glassy polymers would be higher with decreasing temperature; thus tholin should have an even lower fracture toughness at 94 K, which means it would be even more brittle.

4.4.2 Candidates for Titan Sand

There are a few candidates for Titan sand, tholin-like complex organics formed by photochemistry and then modified on the surface, evaporites formed from evaporation process in Titan's dried lake beds, and water ice bed rock. Here we define a material as a good candidate for Titan sand if it is mechanically strong enough to be transported for long distances. We expect the material to have higher hardness and lower brittleness, so it could resist abrasion and impact and will be less likely to be fragmented to dust.

The composition of Titan sand could be similar to tholin if the sand grains are formed by sintering, lithification and erosion, or flocculation (Barnes et al.,

2015; Yu et al., 2017a). Flocculation needs liquid methane or ethane to facilitate sand formation. If sand came from, or is coming from, the polar regions of Titan, this mechanism needs the sand to be mechanically strong enough to transport from the polar lakes and seas to the equatorial area, where the dunes are observed. However, our measurements show that tholin is a relatively soft and brittle material compared to common silicate sand and even soft sand like white gypsum sand on Earth. Thus, if Titan sand is similar to tholin, it may not be strong enough to be transported from Titan's poles to the equator, which suggests that Titan sand should be derived close to the equatorial regions. Titan sand could still be formed by the flocculation mechanism if it originated from the tropical lakes (e.g. Griffith et al., 2012) rather than the polar lakes.

Soluble components of aerosols in methane and ethane lakes may form evaporites. The proposed evaporite fields include ancient lake beds in Tui Regio or Hotei Regio (Barnes et al., 2005, 2006; MacKenzie et al., 2014), dried lake beds south of Ligeia Mare (Barnes et al., 2011), and a ring of dried lake bed surrounding Ontario Lacus (Barnes et al., 2009). These proposed evaporite fields are all spectrally bright at 5 μm. Evaporites are also possible candidates for Titan sand, but they must be physically or chemically modified to become spectrally dark to fit the dune dark spectra. There is no data for mechanical properties of possible Titan evaporites in the solid state, but the simple organic materials we measured have lower elastic moduli and hardnesses than tholin. This suggests that, for evaporites, if they are simple organics as well, may not be strong enough to be transported from the polar regions (e.g. dried lake beds of Ligeia Mare or the ring of dried lake bed around Ontario Lacus)

to form the equatorial dunes. This does not rule out the possibility that the evaporites could be transported to the equatorial region from the ancient lake beds that are located close to the equator, such as Tui Regio or Hotei Regio..

Another possible candidate for Titan sand is water ice. As Barnes et al., (2008) concluded from VIMS data, water ice cannot be ruled out as a component of Titan sand, since the dark organic sand on Titan could be a result of homogeneously organic-coated water ice grains. On the surface of Titan, water ice is in a hexagonal phase, also known as ice Ih. Proctor (1966) reported measurements of the elastic modulus of monocrystalline ice Ih over a broad temperature range from 40 K to 240 K, with the elastic modulus of ice gradually increasing with decreasing temperature. Using the elastic constants measured by Proctor (1966), we can estimate the elastic modulus of water ice at Titan's surface temperature (94 K) using the method described by Anderson (1963), which is around 11 GPa, shown in Figure 4.2. From the linear correlation of elastic modulus and hardness in Figure 4.4, we can estimate the nanoindentation hardness of water ice under Titan's low temperature to be around 0.5 GPa, shown in Figure 4.3. We can also estimate the elastic modulus and hardness of water ice near its freezing point (270 K), which are surprising only slightly lower than at 94 K (E$\sim$9 GPa and H$\sim$0.4 GPa), shown in Figure 4.2 and 4.3, as well. The fracture toughness of water ice is nearly invariant with changing temperature and is around 0.15 MPa$\cdot$m$^{1/2}$ (Litwin et al., 2012). Water ice has a lower elastic modulus and hardness than tholin, but tholin is more brittle. Thus we cannot interpret which material is a better candidate for Titan sand using only their mechanical properties.

Tholin, the simple organics, and water ice on Titan are all mechanically weak, and they may be unable to be transported long distances on Titan. Thus, formation of the materials through subaqueous mechanisms are not favorable for explaining the equatorial dunes on Titan. Several past studies point out that there is no evidence of sediment transportation from Titan's polar regions all the way to the equator (Charnay et al., 2015; Malaska et al., 2016). Solomonidou et al. (2018) and Brossier et al., (2018) suggest that the source of the dune-forming materials may be close to the equatorial region rather than the higher latitudes. This work supports those studies based on the mechanical weakness of Titan sand candidates. It also indicates that sand on Titan maybe produced near where it is observed.

Our study also provides insight into the transportation capacity of Titan sand in the equatorial area. Barnes et al. (2015) proposed that Titan's sands could be in a global transportation system where sand particles should be able to move thousands of kilometers west to east across the equatorial area. However, our measurements suggest that the 'fresh' Titan sand may not be strong enough to be transported the long distances as suggested by Barnes et al., (2015). Alternatively, the sand on Titan could be ancient and was chemically/physically modified to be stronger than the 'fresh' sand.

4.5 Conclusion

To understand the origin of Titan's sand, we used nanoindentation to study the mechanical properties of several Titan sand analogs, including tholin thin films, a few organics (PAHs, polyphenyls, and nitrogen containing organics),

natural sands on Earth (silicate beach sand, carbonate sand, and white gypsum sand), and some common materials used in the Titan Wind Tunnel (such as walnut shells). Mechanical properties measured include elastic modulus (E, elastic property), hardness (H, plastic property), and fracture toughness (K_c, brittleness, fracture property). Under room temperature, tholin has an elastic modulus of around 10 GPa, nanoindentation hardness of around 0.5 GPa, and fracture toughness of around 0.036 MPa·$m^{1/2}$. Extrapolated to Titan conditions (94 K), tholin's elastic modulus is around 16 GPa, nanoindentation hardness is around 0.8 GPa, and its fracture toughness will be lower than 0.036 MPa·$m^{1/2}$. Compared to common polymers, tholin is very stiff, strong but brittle, which indicates it has much more complex cross-link networks than common network polymers like epoxy resin. Many low density materials used in the Titan Wind Tunnel, such as walnut shells, GCs, instant coffee, and activated charcoal, have similar elastic modulus and hardness values to tholin, which suggests that they are good analogs to Titan sand in terms of their mechanical properties, although their interparticle forces are very different (Yu et al., 2017a).

We define a material to be a good candidate for Titan sand if it is mechanically strong enough (with high hardness and low brittleness) to be transported for long distances without being abraded to dust. However, the elastic modulus and hardness values of natural sand on Earth are an order of magnitude larger than tholin: silicate beach sand has an elastic modulus of over 100 GPa and hardness of around 10 GPa; even the mechanically weak white gypsum sand has a higher elastic modulus and hardness than tholin (E=37 GPa and

H=1.5 GPa). Tholin is also much more brittle than silicate sand: its fracture toughness is an order of magnitude smaller than silicate sand (K_c =0.9 MPa·$m^{1/2}$). This indicates that the organic sand (if it is compositionally similar to tholin) on Titan may not originate from the current lakes and seas on Titan; being soft and brittle, it is not mechanically strong enough to transport from the pole to the equator. The elastic moduli and hardness of the simple organics are all lower than tholin, which indicates evaporites (if they are made of simple organics), may not be good candidates for Titan sand, unless they are physically/chemically modified to be more complex and mechanically stronger. Water ice has similar elastic modulus and hardness values to tholin (E=11 GPa, H=0.5 GPa), but it has a slightly higher fracture toughness (K_c=0.15 MPa·$m^{1/2}$). However, we are unable to determine whether water ice or tholin is a better candidate for Titan sand by only comparing their mechanical properties.

Chapter 5

Discussion and Conclusion

5.1 Threshold Wind Speed on Titan

The Titan Wind Tunnel experiments data suggest a higher than model predicted threshold wind speed on Titan because of the low density ratio (particle density over atmospheric density) on Titan compared to Earth (Burr et al., 2015). The humidity in the TWT cannot be controlled but the extent of humidity (RH$\sim$30%) did not substantially affect the threshold wind speed measurements for low density materials compared to dry conditions (Chapter 2). In Chapter 3, I also directly measured the interparticle forces between walnut shell particles used in the Titan Wind Tunnel and between tholin particles. I found that the tholin particles are stickier than walnut shells particles. This indicates that an even higher threshold wind speed is needed to saltate sand particles on Titan than previously proposed by Burr et al. (2015). A number of Titan GCMs suggest that the model generated circulation patterns are sensitive to the choice of threshold wind speed values (e.g. Tokano, 2010; McDonald et al., 2016). Thus, a more realistic threshold wind speed used in

future GCMs can better constrain wind patterns and climate on Titan.

5.2 Effect of Liquid Humidity on Sand Transport

In Chapter 2, I found that materials with high and low water content might have different interparticle cohesion schemes. For materials with low water content, like quartz sand, the interparticle forces are dominated by capillary forces; as relative humidity (RH)/water content increases, threshold wind speed increases accordingly. However, for low density materials like walnut shells, when the water content (w) is lower than an initiation water content ($w<w'$), the interparticle forces are dominated by very weak adsorption forces. Thus for $w<w'$, as RH increases, the threshold does not substantially change. Once the initiation water content is reached ($w>w'$), capillary forces start to dominate and the threshold starts to increase with increasing RH. Therefore, determination of water content of materials can provide insight into its sensitivity of threshold wind speed to RH.

This result could have further implications for organic sand on Titan, where methane is the dominant vapor form. Laboratory studies show that tholin (produced in a different lab) can at most adsorb 0.3% methane by mass (Curtis et al., 2008). Thus I suggest that the effect of methane vapor on the threshold wind speed of Titan's organic sand could be similar to that of water vapor on quartz sand. With increasing methane RH, the threshold wind speed for Titan's organic sand will increase accordingly, with no initiation liquid content as with walnut shells to water vapor. I also modeled the effect of methane humidity on the threshold wind speed on Titan. I found that even though the

threshold wind speed is sensitive to methane humidity, the overall change is less than 20% (even for methane RH approaching 100%) compared to dry conditions. This minimal change could be attributed to the low surface tension of liquid methane and Titan's low temperature.

The threshold model I developed in Chapter 2 assumes that the geometry, roughness, and surface energy of Titan's organic sand is the same as quartz sand on Earth. In Chapter 3, I directly measured the surface energy of tholin through contact angle measurements, and I found tholin's surface energy is quite high, $\sim$71 mN/m, which could result in higher than previously thought interparticle cohesion under dry conditions. While because of liquid methane's low surface tension, the capillary forces for tholin particles under 'wet' (high methane humidity) conditions on Titan could be smaller than the interparticle cohesion between tholin under dry conditions. Thus, contrary to the effect of water on terrestrial sediments, Titan's sand may be less sticky under increasing methane humidity, which would make it easier to be moved. Note that I assumed that the Titan sand particles are perfect smooth spheres, which may not be the case on Titan. Rough particles usually have much lower interparticle cohesion under dry conditions. Thus the above scenario cannot be confirmed before we find out the actual geometry and roughness of individual sand particles on Titan.

5.3 Dune Formation Wind Orientation

Rubin and Hesp (2009) suggested that the linear dunes on Titan could be formed by unidirectional wind if the sediments are more cohesive than typical

terrestrial quartz sand. In Chapter 3, I found out that the tholin particles have higher interparticle cohesion than between quartz sand on Earth, suggesting that tholin particles may be more cohesive than terrestrial quartz sand (again, assuming the geometry of Titan sand is same as tholin particles produced in laboratory). Thus the unidirectional wind formation mechanism of the Titan dunes could apply on Titan.

5.4 Sand Size

Titan's sand particle sizes were first estimated to be around 100–300 μm based on calculation of the optimum particle diameter range that results the minimum threshold wind speed on Titan (Lorenz et al., 2006). Lorenz (2014) suggests that plausibly decreased particle density or increased cohesion between particles could lead to higher optimum diameter up to around 500–600 μm. While my work in Chapter 3 did find the cohesion forces of tholin larger than those of silicate sand and materials used in the Titan Wind Tunnel.

5.5 Origin of Titan Sand Particles

The origin of Titan sand particles is a mystery. They are mostly likely originated from photochemically-produced organic particles descending from the atmosphere, but the transformation mechanism from the small aerosol particles (up to 1 μm when reaching the surface, Tomasko et al., 2005) or the small condensed simple organic particles to the large sand-sized particles is unknown. The proposed mechanisms (Barnes et al., 2015) include

small-to-big (bottom-up) or big-to-small (top-down) mechanisms, and both processes could happen either under dry conditions or with the facility of liquid hydrocarbons ('wet' transformation). In Chapter 3, I explored whether the small-to-big mechanism such as sintering is viable. I found high cohesion between the tholin particles through AFM measurements, which suggests it could be easier to coagulate small aerosol particles on Titan into bigger particles, making the small-to-big mechanism viable.

In Chapter 4, I explored the possibility of the 'dry' and the 'wet' mechanisms. Titan's dunes are located mainly in the equatorial regions, while most of the hydrocarbon lakes and seas are located in the polar regions of Titan. So if the 'wet' mechanisms are the only ways to make Titan's sand, the sand particles have to be mechanically strong enough to be able to get transported from the poles to the equatorial region without being ground and broken into dust. While if the Titan sand particles are made without using hydrocarbon liquids, then they can be produced everywhere on Titan, including the equatorial region where the dunes are located. The 'wet' transformations require the Titan sand to be mechanically strong while the 'dry' transformations do not. Thus I used a technique called nanoindentation to measure the relevant mechanical properties for a few Titan sand analogs and terrestrial sediments. I found that the Titan sand analogs are all softer, less rigid, and more brittle compared to even the weakest sediments on Earth (white gypsum sand), which suggests the Titan sand may not be strong enough to transport long distances, and the 'wet' transformations may not be viable to produce sand particles on Titan. My result also validates Cassini mapping observations such as Malaska et al.

(2016), Solomonidou et al. (2018), and Brossier et al., (2018) that sediments do not transport all the way from Titan's polar regions to the equator.

5.6 Material Properties of Tholin

In Chapter 3, I measured the surface energy of tholin to be around 71 mN/m, which is higher than common polymers such as polystyrene and polyethylene. In Chapter 4, I measured a few mechanical properties of tholin, including nanoindentation hardness (H$\sim$0.5 GPa), elastic modulus (E$\sim$10 GPa), and fracture toughness ($K_c \sim 0.036 MPa \cdot m^{1/2}$). Tholin is much harder, stiffer, but much more brittle than common polymers, which indicates that it has a higher cross-linked structure than common network polymers.

5.7 Unsolved Mysteries

My work has helped to understand many of the questions I proposed to answer, but a number of questions remain for aeolian processes on Titan. Several major questions are listed here.

- What is Titan's sand actually made of? The simulants that we tested include tholin and some simple organics, but none of these materials are spectrally 'dark' enough the fit the actual dune spectra.
- What is the geometry of individual sand particles on Titan?

- What is the true origin of Titan's organic sand? Is a big-to-small mechanism, such as lithification and erosion, possible to make big sand particles from small aerosol particles?
- Are the undifferentiated plains on Titan related to aeolian processes? If so, how?

5.8 Final Thoughts

The Cassini mission ended in September, 2017, having provided an numerous amount of data from the Saturn system. However, there are still many unanswered questions. Laboratory experiments can be used to continue exploring new possibilities, until a new mission is sent to Titan!

References

Anderson, O. (1963). "A simplified method for calculating the debye temperature from elastic constants". In: *Journal of Physics and Chemistry of Solids* 24, pp. 909–917. DOI: 10.1016/0022-3697(63)90067-2.

Anderson, R. S. (1987). "A theoretical model for aeolian impact ripples". In: *Sedimentology* 34, pp. 943–956. DOI: 10.1111/j.1365-3091.1987.tb00814.x.

Andreotti, B. (2004). "A two-species model of aeolian sand transport". In: *Journal of Fluid Mechanics* 510, pp. 47–70. DOI: 10.1017/S0022112004009073.

Anstis, G. R., P. Chantikul, B. R. Lawn, and D. B. Marshall (1981). "A critical evaluation of indentation techniques for measuring fracture toughness: I, Direct crack measurements". In: *Journal of the American Ceramic Society* 64, pp. 533–538. DOI: 10.1111/j.1151-2916.1981.tb10320.

Bagnold, R. A. (1936). "The Movement of Desert Sand". In: *Proceedings of the Royal Society of London Series A* 157, pp. 594–620. DOI: 10.1098/rspa.1936.0218.

Bagnold, R. A. (1941). *The physics of blown sand and desert dunes.* Methuen, London.

Baidakov, V. G., A. M. Kaverin, and M. N. Khotienkova (2013). "Surface tension of ethane methane solutions: 1. experiment and thermodynamic analysis of the results". In: *Fluid Phase Equilib.* 356, pp. 90–95. DOI: 10.1016/j.fluid.2013.07.008.

Barnes, J. W., R. H. Brown, E. P. Turtle, A. S. McEwen, R. D. Lorenz, M. Janssen, E. L. Schaller, M. E. Brown, B. J. Buratti, C. Sotin, C. Griffith, R. Clark, J. Perry, S. Fussner, J. Barbara, R. West, C. Elachi, A. H. Bouchez, H. G. Roe, K. H. Baines, G. Bellucci, J.-P. Bibring, F. Capaccioni, P. Cerroni, M. Combes, A. Coradini, D. P. Cruikshank, P. Drossart, V. Formisano, R. Jaumann, Y. Langevin, D. L. Matson, T. B. McCord, P. D. Nicholson, and B. Sicardy (2005). "A 5-Micron-Bright Spot on Titan: Evidence for Surface Diversity". In: *Science* 310, pp. 92–95. DOI: 10.1126/science.1117075.

Barnes, J. W., R. H. Brown, J. Radebaugh, B. J. Buratti, C. Sotin, S. Le Mouelic, S. Rodriguez, E. P. Turtle, J. Perry, R. Clark, K. H. Baines, and P. D. Nicholson (2006). "Cassini observations of flow-like features in western Tui Regio, Titan". In: *Geophysical Research Letters* 33, p. L16204. DOI: 10.1029/2006GL026843.

Barnes, J. W., R. H. Brown, L. Soderblom, B. J. Buratti, C. Sotin, S. Rodriguez, S. Le Mouèlic, K. H. Baines, R. Clark, and P. Nicholson (2007). "Global-scale surface spectral variations on Titan seen from Cassini/VIMS". In: *Icarus* 186, pp. 242–258. DOI: 10.1016/j.icarus.2006.08.021.

Barnes, J. W., R. H. Brown, L. Soderblom, C. Sotin, S. Le Mouèlic, S. Rodriguez, R. Jaumann, R. A. Beyer, B. J. Buratti, K. Pitman, K. H. Baines, R. Clark, and P. Nicholson (2008). "Spectroscopy, morphometry, and photoclinometry of Titan's dunefields from Cassini/VIMS". In: *Icarus* 195, pp. 400–414. DOI: 10.1016/j.icarus.2007.12.006.

Barnes, J. W., R. H. Brown, J. M. Soderblom, L. A. Soderblom, R. Jaumann, B. Jackson, S. Le Mouélic, C. Sotin, B. J. Buratti, K. M. Pitman, K. H. Baines, R. N. Clark, P. D. Nicholson, E. P. Turtle, and J. Perry (2009). "Shoreline features of Titan's Ontario Lacus from Cassini/VIMS observations". In: *Icarus* 201, pp. 217–225. DOI: 10.1016/j.icarus.2008.12.028.

Barnes, J. W., J. Bow, J. Schwartz, R. H. Brown, J. M. Soderblom, A. G. Hayes, G. Vixie, S. Le Mouélic, S. Rodriguez, C. Sotin, R. Jaumann, K. Stephan, L. A. Soderblom, R. N. Clark, B. J. Buratti, K. H. Baines, and P. D. Nicholson (2011). "Organic sedimentary deposits in Titan's dry lakebeds: Probable evaporite". In: *Icarus* 216, pp. 136–140. DOI: 10.1016/j.icarus.2011.08.022.

Barnes, J. W., R. D. Lorenz, J. Radebaugh, A. G. Hayes, K. Arnold, and C. Chandler (2015). "Production and global transport of Titan's sand particles". In: *Planetary Science* 4, p. 1. DOI: 10.1186/s13535-015-0004-y.

Beach, E. R., G. W. Tormoen, J. Drelich, and R. Han (2002). "Pull-off Force Measurements between Rough Surfaces by Atomic Force Microscopy". In: *Journal of Colloid and Interface Science* 247, pp. 84–99. DOI: 10.1006/jcis.2001.8126.

Belly, P. Y. (1964). "Sand movement by wind". In: *US Army Corps of Engineering (US-ACE)*.

Bird, M. K., M. Allison, S. W. Asmar, D. H. Atkinson, I. M. Avruch, R. Dutta-Roy, Y. Dzierma, P. Edenhofer, W. M. Folkner, L. I. Gurvits, D. V. Johnston, D. Plettemeier, S. V. Pogrebenko, R. A. Preston, and G. L. Tyler (2005).

"The vertical profile of winds on Titan". In: *Nature* 438, pp. 800–802. DOI: 10.1038/nature04060.

Bisal, F. and J. Hsieh (1966). "Influence of moisture on erodibility of soil by wind". In: *Soil Sci.* 102, pp. 143–146.

Bourke, M. C., N. Lancaster, L. K. Fenton, E. J. R. Parteli, J. R. Zimbelman, and J. Radebaugh (2010). "Extraterrestrial dunes: An introduction to the special issue on planetary dune systems". In: *Geomorphology* 121, pp. 1–14. DOI: 10.1016/j.geomorph.2010.04.007.

Bridges, N., D. M. Burr, J. Marshall, J. K. Smith, J. P. Emery, S. M. Horst, E. Nield, and X. Yu (2015). "New Titan Saltation Threshold Experiments: Investigating Current and Past Climates". In: *AGU Fall Meeting Abstracts*, P12B–05.

Brossier, J. F., S. Rodriguez, T. Cornet, A. Lucas, J. Radebaugh, L. Maltagliati, S. Le Mouélic, A. Solomonidou, A. Coustenis, M. Hirtzig, R. Jaumann, K. Stephan, and C. Sotin (2018). "Geological Evolution of Titan's Equatorial Regions: Possible Nature and Origin of the Dune Material". In: *Journal of Geophysical Research (Planets)* 123, pp. 1089–1112. DOI: 10.1029/2017JE005399.

Brown, R. H., L. A. Soderblom, J. M. Soderblom, R. N. Clark, R. Jaumann, J. W. Barnes, C. Sotin, B. Buratti, K. H. Baines, and P. D. Nicholson (2008). "The identification of liquid ethane in Titan's Ontario Lacus". In: *Nature* 454, pp. 607–610. DOI: 10.1038/nature07100.

Brown, M. E., J. E. Roberts, and E. L. Schaller (2010). "Clouds on Titan during the Cassini prime mission: A complete analysis of the VIMS data". In: *Icarus* 205, pp. 571–580. DOI: 10.1016/j.icarus.2009.08.024.

Brown, R. H., K. H. Baines, G. Bellucci, J.-P. Bibring, B. J. Buratti, F. Capaccioni, P. Cerroni, R. N. Clark, A. Coradini, D. P. Cruikshank, P. Drossart, V. Formisano, R. Jaumann, Y. Langevin, D. L. Matson, T. B. Mccord, V. Mennella, E. Miller, R. M. Nelson, P. D. Nicholson, B. Sicardy, and C. Sotin (2004). "The Cassini Visual and Infrared Mapping Spectrometer (VIMS) Investigation". In: *The Cassini-Huygens Mission*. Ed. by C. T. Russell, p. 111. DOI: 10.1007/1-4020-3874-7_3.

Bunker, M. J., M. C. Davies, M. B. James, and C. J. Roberts (2007). "Direct observation of single particle electrostatic charging by atomic force microscopy". In: *Pharm. Res.* 24, pp. 1165–1169. DOI: 10.1007/s11095-006-9230-z.

Burr, D. M., N. T. Bridges, J. R. Marshall, J. K. Smith, B. R. White, and J. P. Emery (2015a). "Higher-than-predicted saltation threshold wind speeds on Titan". In: *Nature* 517, pp. 60–63. DOI: 10.1038/nature14088.

Burr, D. M., N. T. Bridges, J. K. Smith, J. R. Marshall, B. R. White, and D. A. Williams (2015b). "The titan wind tunnel: a new tool for investigating extraterrestrial aeolian environments". In: *Aeolian Res.* 18, pp. 205–214. DOI: 10.1016/j.aeolia.2015.07.008.

Cable, M. L., s. M. Hörst, R. Hodyss, P. M. Beauchamp, M. A. Smith, and P. A. Willis (2012). "Titan tholins: simulating Titan organic chemistry in the Cassini-Huygens era." In: *Chem. Rev* 3, pp. 1882–1909. DOI: 10.1021/cr200221x.

Capaccioni, F., A. Coradini, G. Filacchione, S. Erard, G. Arnold, P. Drossart, M. C. De Sanctis, D. Bockelee-Morvan, M. T. Capria, F. Tosi, C. Leyrat, B. Schmitt, E. Quirico, P. Cerroni, V. Mennella, A. Raponi, M. Ciarniello, T. McCord, L. Moroz, E. Palomba, E. Ammannito, M. A. Barucci, G. Bellucci, J. Benkhoff, J. P. Bibring, A. Blanco, M. Blecka, R. Carlson, U. Carsenty, L. Colangeli, M. Combes, M. Combi, J. Crovisier, T. Encrenaz, C. Federico, U. Fink, S. Fonti, W. H. Ip, P. Irwin, R. Jaumann, E. Kuehrt, Y. Langevin, G. Magni, S. Mottola, V. Orofino, P. Palumbo, G. Piccioni, U. Schade, F. Taylor, D. Tiphene, G. P. Tozzi, P. Beck, N. Biver, L. Bonal, J.-P. Combe, D. Despan, E. Flamini, S. Fornasier, A. Frigeri, D. Grassi, M. Gudipati, A. Longobardo, K. Markus, F. Merlin, R. Orosei, G. Rinaldi, K. Stephan, M. Cartacci, A. Cicchetti, S. Giuppi, Y. Hello, F. Henry, S. Jacquinod, R. Noschese, G. Peter, R. Politi, J. M. Reess, and A. Semery (2015). "The organic-rich surface of comet 67P/Churyumov-Gerasimenko as seen by VIRTIS/Rosetta". In: *Science* 347.1, aaa0628. DOI: 10.1126/science.aaa0628.

Carrasco, N., I. Schmitz-Afonso, J.-Y. Bonnet, E. Quirico, R. Thissen, O. Dutuit, A. Bagag, O. Laprévote, A. Buch, A. Giulani, G. Adandé, F. Ouni, E. Hadamcik, C. Szopa, and G. Cernogora (2009). "Chemical Characterization of Titan's Tholins: Solubility, Morphology and Molecular Structure Revisited". In: *Journal of Physical Chemistry A* 113, pp. 11195–11203. DOI: 10.1021/jp904735q.

Carrasco, N., T. Gautier, E.-t. Es-sebbar, P. Pernot, and G. Cernogora (2012). "Volatile products controlling Titan's tholins production". In: *Icarus* 219, pp. 230–240. DOI: 10.1016/j.icarus.2012.02.034.

Charnay, B., F. Forget, G. Tobie, C. Sotin, and R. Wordsworth (2014). "Titan's past and future: 3D modeling of a pure nitrogen atmosphere and geological implications". In: *Icarus* 241, pp. 269–279. DOI: 10.1016/j.icarus.2014.07.009.

Charnay, B., E. Barth, S. Rafkin, C. Narteau, S. Lebonnois, S. Rodriguez, S. Courrech Du Pont, and A. Lucas (2015). "Methane storms as a driver

of Titan's dune orientation". In: *Nature Geoscience* 8, pp. 362–366. DOI: 10.1038/ngeo2406.

Chen, W., D. Zhibao, L. Zhenshan, and Y. Zuotao (1996). "Wind tunnel test of the influence of moisture on the erodibility of loessial sandy loam soils by wind". In: *Journal of Arid Environments* 34, pp. 391–402. DOI: 10.1006/jare.1996.0119.

Christenson, H. K. (1988). "Adhesion between surfaces in undersaturated vapors–a reexamination of the influence of meniscus curvature and surface forces". In: *Journal of Colloid and Interface Science* 121, pp. 170–178. DOI: 10.1016/0021-9797(88)90420-1.

Clark, R. N., J. M. Curchin, J. W. Barnes, R. Jaumann, L. Soderblom, D. P. Cruikshank, R. H. Brown, S. Rodriguez, J. Lunine, K. Stephan, T. M. Hoefen, S. Le Mouélic, C. Sotin, K. H. Baines, B. J. Buratti, and P. D. Nicholson (2010). "Detection and mapping of hydrocarbon deposits on Titan". In: *Journal of Geophysical Research (Planets)* 115, E10005. DOI: 10.1029/2009JE003369.

Coates, A. J., F. J. Crary, G. R. Lewis, D. T. Young, J. H. Waite, and E. C. Sittler (2007). "Discovery of heavy negative ions in Titan's ionosphere". In: *Geophysical Research Letters* 34, p. L22103. DOI: 10.1029/2007GL030978.

Coates, A. J., A. Wellbrock, G. R. Lewis, G. H. Jones, D. T. Young, F. J. Crary, and J. H. Waite (2009). "Heavy negative ions in Titan's ionosphere: Altitude and latitude dependence". In: *Planetary and Space Science* 57, pp. 1866–1871. DOI: 10.1016/j.pss.2009.05.009.

Coll, P., D. Coscia, N. Smith, M.-C. Gazeau, S. I. Ramírez, G. Cernogora, G. Israël, and F. Raulin (1999). "Experimental laboratory simulation of Titan's atmosphere: aerosols and gas phase". In: *Planetary and Space Science* 47, pp. 1331–1340. DOI: 10.1016/S0032-0633(99)00054-9.

Cooper, K., N. Ohler, A. Gupta, and S. Beaudoin (2000). "Analysis of Contact Interactions between a Rough Deformable Colloid and a Smooth Substrate". In: *Journal of Colloid and Interface Science* 222, pp. 63–74. DOI: 10.1006/jcis.1999.6561.

Cordier, D., J. W. Barnes, and A. G. Ferreira (2013). "On the chemical composition of Titan's dry lakebed evaporites". In: *Icarus* 226, pp. 1431–1437. DOI: 10.1016/j.icarus.2013.07.026.

Cordier, D., T. Cornet, J. W. Barnes, S. M. MacKenzie, T. Le Bahers, D. Nna-Mvondo, P. Rannou, and A. G. Ferreira (2016). "Structure of Titan's evaporites". In: *Icarus* 270, pp. 41–56. DOI: 10.1016/j.icarus.2015.12.034.

Courtney, T. H. (2005). *Mechanical Behavior of Materials.* Long Grove, IL.: Waveland Press.

Coustenis, A., R. K. Achterberg, B. J. Conrath, D. E. Jennings, A. Marten, D. Gautier, C. A. Nixon, F. M. Flasar, N. A. Teanby, B. Bézard, R. E. Samuelson, R. C. Carlson, E. Lellouch, G. L. Bjoraker, P. N. Romani, F. W. Taylor, P. G. J. Irwin, T. Fouchet, A. Hubert, G. S. Orton, V. G. Kunde, S. Vinatier, J. Mondellini, M. M. Abbas, and R. Courtin (2007). "The composition of Titan's stratosphere from Cassini/CIRS mid-infrared spectra". In: *Icarus* 189, pp. 35–62. DOI: 10.1016/j.icarus.2006.12.022.

Corn, M. (1961). "The adhesion of solid particles to solid surfaces. I. A review". In: *Journal of the Air Pollution Control Association* 11.

Curtis, D. B., C. D. Hatch, C. A. Hasenkopf, O. B. Toon, M. A. Tolbert, C. P. McKay, and B. N. Khare (2008). "Laboratory studies of methane and ethane adsorption and nucleation onto organic particles: Application to Titan's clouds". In: *Icarus* 195, pp. 792–801. DOI: 10.1016/j.icarus.2008.02.003.

Derjaguin, B. (1934). "Untersuchungen über die Reibung und Adhäsion". In: *Colloid & polymer science* 69.

Derjaguin, B. V., V. M. Muller, and Y. P. Toporov (1975). "Effect of contact deformations on the adhesion of particles". In: *Journal of Colloid and Interface Science* 53, pp. 314–326. DOI: 10.1016/0021-9797(75)90018-1.

Dimitrov, V. and A. Bar-Nun (2002). "Aging of Titan's Aerosols". In: *Icarus* 156, pp. 530–538. DOI: 10.1006/icar.2001.6802.

Dragan, C., O. Fati, M. Radu, L. Calin, A. Samuila, and L. Dascalescu (2011). "Tribocharging of mixed granular plastics in a fluidized-bed device." In: *IEEE Transactions on Industry Applications* 47, pp. 1922–1928. DOI: 10.1109/TIA.2011.2156374.

Ducker, W. A., T. J. Senden, and R. M. Pashley (1991). "Direct measurement of colloidal forces using an atomic force microscope". In: *Nature* 353, pp. 239–241. DOI: 10.1038/353239a0.

Durán, O., P. Claudin, and B. Andreotti (2011). "On aeolian transport: Grain-scale interactions, dynamical mechanisms and scaling laws". In: *Aeolian Research* 3, pp. 243–270. DOI: 10.1016/j.aeolia.2011.07.006.

Edgett, K. S. and M. C. Malin (2000). "New views of Mars eolian activity, materials, and surface properties: Three vignettes from the Mars Global Surveyor Mars Orbiter Camera". In: *Journal of Geophysical Research* 105, pp. 1623–1650. DOI: 10.1029/1999JE001152.

Elachi, C., S. Wall, M. Janssen, E. Stofan, R. Lopes, R. Kirk, R. Lorenz, J. Lunine, F. Paganelli, L. Soderblom, C. Wood, L. Wye, H. Zebker, Y. Anderson, S. Ostro, M. Allison, R. Boehmer, P. Callahan, P. Encrenaz, E. Flamini, G. Francescetti, Y. Gim, G. Hamilton, S. Hensley, W. Johnson, K. Kelleher, D.

Muhleman, G. Picardi, F. Posa, L. Roth, R. Seu, S. Shaffer, B. Stiles, S. Vetrella, and R. West (2006). "Titan Radar Mapper observations from Cassini's T_3 fly-by". In: *Nature* 441, pp. 709–713. DOI: 10.1038/nature04786.

Ewing, R. C., A. G. Hayes, and A. Lucas (2015). "Sand dune patterns on Titan controlled by long-term climate cycles". In: *Nature Geoscience* 8, pp. 15–19. DOI: 10.1038/ngeo2323.

Fécan, F., B. Marticorena, and G. Bergametti (1999). "Parametrization of the increase of the aeolian erosion threshold wind friction velocity due to soil moisture for arid and semi-arid areas". In: *Annales Geophysicae* 17, p. 149. DOI: 10.1007/s00585-999-0149-7.

Fenton, L. K. and R. K. Hayward (2010). "Southern high latitude dune fields on Mars: Morphology, aeolian inactivity, and climate change". In: *Geomorphology* 121, pp. 98–121. DOI: 10.1016/j.geomorph.2009.11.006.

Findorák, R., M. Fröhlichová, J. Legemza, and L. Findoráková (2016). "Thermal degradation and kinetic study of sawdusts and walnut shells via thermal analysis". In: *J. Therm. Anal. Calorim.* Pp. 1–6. DOI: 10.1007/s10973-016-5264-6.

Fisher, L. R. and J. N. Israelachvili (1981). "Experimental studies on the applicability of the Kelvin equation to highly curved concave menisci". In: *Journal of Colloid and Interface Science* 80, pp. 528–541. DOI: 10.1016/0021-9797(81)90212-5.

Folkner, W. M., S. W. Asmar, J. S. Border, G. W. Franklin, S. G. Finley, J. Gorelik, D. V. Johnston, V. V. Kerzhanovich, S. T. Lowe, R. A. Preston, M. K. Bird, R. Dutta-Roy, M. Allison, D. H. Atkinson, P. Edenhofer, D. Plettemeier, and G. L. Tyler (2006). "Winds on Titan from ground-based tracking of the Huygens probe". In: *Journal of Geophysical Research (Planets)* 111, E07S02. DOI: 10.1029/2005JE002649.

Friedman, J. D. (1966). *Composition of basalt flow samples at Pisgah Crater, California (Technical Report NASA-20). Geological Survey: In Natural Resources Program*. Tech. rep.

Friedson, A. J., R. A. West, E. H. Wilson, F. Oyafuso, and G. S. Orton (2009). "A global climate model of Titan's atmosphere and surface". In: *Planetary and Space Science* 57, pp. 1931–1949. DOI: 10.1016/j.pss.2009.05.006.

Fryberger, S. G. and G. Dean (1979). *Dune forms and wind regime.* In: McKee, E.D. (Ed.), A Study of Global Sand Seas, 1052. U.S. Geol. Surv. Prof. Pap., pp. 137-169.

Fulchignoni, M., F. Ferri, F. Angrilli, A. J. Ball, A. Bar-Nun, M. A. Barucci, C. Bettanini, G. Bianchini, W. Borucki, G. Colombatti, M. Coradini, A.

Coustenis, S. Debei, P. Falkner, G. Fanti, E. Flamini, V. Gaborit, R. Grard, M. Hamelin, A. M. Harri, B. Hathi, I. Jernej, M. R. Leese, A. Lehto, P. F. Lion Stoppato, J. J. López-Moreno, T. Mäkinen, J. A. M. McDonnell, C. P. McKay, G. Molina-Cuberos, F. M. Neubauer, V. Pirronello, R. Rodrigo, B. Saggin, K. Schwingenschuh, A. Seiff, F. Simões, H. Svedhem, T. Tokano, M. C. Towner, R. Trautner, P. Withers, and J. C. Zarnecki (2005). "In situ measurements of the physical characteristics of Titan's environment". In: *Nature* 438, pp. 785–791. DOI: 10.1038/nature04314.

Giri, M., D. B. Bousfield, and W. N. Unertl (2001). "Dynamic contacts on viscoelastic films: work of adhesion". In: *Langmuir* 17, pp. 2973–2981.

Gladstone, G. R. et al. (2016). "The atmosphere of Pluto as observed by New Horizons". In: *Science* 351, aad8866. DOI: 10.1126/science.aad8866.

Greeley, R., R. Leach, B. White, J. Iversen, and J. B. Pollack (1980). "Threshold windspeeds for sand on Mars - Wind tunnel simulations". In: *Geophysical Research Letters* 7, pp. 121–124. DOI: 10.1029/GL007i002p00121.

Greeley, R. and J. D. Iversen (1985). *Wind as a geological process on Earth, Mars, Venus and Titan*. Cambridge University Press, Cambridge.

Greeley, R., B. White, R. Leach, J. Iversen, and J. Pollack (1976). "Mars - Wind friction speeds for particle movement". In: *Geophysical Research Letters* 3, pp. 417–420. DOI: 10.1029/GL003i008p00417.

Greeley, R., B. R. White, J. B. Pollack, J. D. Iverson, and R. N. Leach (1977). *Dust storms on Mars: Considerations and simulations*.

Greeley, R., J. Iversen, R. Leach, J. Marshall, B. White, and S. Williams (1984). "Windblown sand on Venus - Preliminary results of laboratory simulations". In: *Icarus* 57, pp. 112–124. DOI: 10.1016/0019-1035(84)90013-7.

Greeley, R., J. R. Marshall, and R. N. Leach (1985). *Microdunes and other aeolian bedforms on Venus: Wind tunnel simulations*. Tech. rep.

Greenwood, J. A. and J. B. P. Williamson (1966). "Contact of Nominally Flat Surfaces". In: *Proceedings of the Royal Society of London Series A* 295, pp. 300–319. DOI: 10.1098/rspa.1966.0242.

Griffith, C. A., J. M. Lora, J. Turner, P. F. Penteado, R. H. Brown, M. G. Tomasko, L. Doose, and C. See (2012). "Possible tropical lakes on Titan from observations of dark terrain". In: *Nature* 486, pp. 237–239. DOI: 10.1038/nature11165.

Gwon, J. G., S. Y. Lee, S. J. Chun, G. H. Doh, and J. H. Kim (2010). "Effects of chemical treatments of hybrid fillers on the physical and thermal properties of wood plastic composites". In: *Composites Part A* 41, pp. 1491–1497. DOI: 10.1016/j.compositesa.2010.06.011.

Hanel, R., B. Conrath, F. M. Flasar, V. Kunde, W. Maguire, J. C. Pearl, J. Pirraglia, R. Samuelson, L. Herath, M. Allison, D. P. Cruikshank, D. Gautier, P. J. Gierasch, L. Horn, R. Koppany, and C. Ponnamperuma (1981). "Infrared observations of the Saturnian system from Voyager 1". In: *Science* 212, pp. 192–200. DOI: 10.1126/science.212.4491.192.

Harding, D., W. Oliver, and G. Pharr (1994). "Cracking during nanoindentation and its use in the measurement of fracture toughness". In: *MRS Proceedings* 356, 663âĂŞ668. DOI: 10.1557/PROC-356-663.

Haugstad, G. (2012). *Atomic force microscopy: Understanding basic modes and advanced applications.* Hoboken, NJ: John Wiley. DOI: 10.1002/9781118360668.

Hay, J. and B. Crawford (2011). "Measuring substrate-independent modulus of thin films". In: *Journal of Materials Research* 26, pp. 727–738. DOI: 10.1557/jmr.2011.8.

Hayes, A. G. (2016). "The Lakes and Seas of Titan". In: *Annual Review of Earth and Planetary Sciences* 44, pp. 57–83. DOI: 10.1146/annurev-earth-060115-012247.

He, C. and M. A. Smith (2013). "Identification of nitrogenous organic species in Titan aerosols analogs: Nitrogen fixation routes in early atmospheres". In: *Icarus* 226, pp. 33–40. DOI: 10.1016/j.icarus.2013.05.013.

He, C. and M. A. Smith (2014c). "Solubility and stability investigation of Titan aerosol analogs: New insight from NMR analysis". In: *Icarus* 232, pp. 54–59. DOI: 10.1016/j.icarus.2014.01.007.

He, C. and M. A. Smith (2014b). "Identification of nitrogenous organic species in Titan aerosols analogs: Implication for prebiotic chemistry on Titan and early Earth". In: *Icarus* 238, pp. 86–92. DOI: 10.1016/j.icarus.2014.05.012.

He, C. and M. A. Smith (2014a). "A comprehensive NMR structural study of Titan aerosol analogs: Implications for Titan's atmospheric chemistry". In: *Icarus* 243, pp. 31–38. DOI: 10.1016/j.icarus.2014.09.021.

He, C., G. Lin, K. T. Upton, H. Imanaka, and M. A. Smith (2012). "Structural Investigation of Titan Tholins by Solution-State1H,13C, and15N NMR: One-Dimensional and Decoupling Experiments". In: *Journal of Physical Chemistry A* 116, pp. 4760–4767. DOI: 10.1021/jp3016062.

He, C., S. M. Hörst, S. Riemer, J. A. Sebree, N. Pauley, and V. Vuitton (2017). "Carbon Monoxide Affecting Planetary Atmospheric Chemistry". In: *ApJL* 841, p. L31. DOI: 10.3847/2041-8213/aa74cc.

Hejda, F. (2010). "Surface Free Energy Determination by Contact Angle Measurements - A Comparison of Various Approaches". In: *WDS 2010 - Proceedings of Contributed Papers. Proceedings of the 19th Annual Conference of Doctoral Students, held 1-4 June 2010, in Prague.* Pp. 25–30.

Hirtzig, M., B. Bézard, E. Lellouch, A. Coustenis, C. de Bergh, P. Drossart, A. Campargue, V. Boudon, V. Tyuterev, P. Rannou, T. Cours, S. Kassi, A. Nikitin, D. Mondelain, S. Rodriguez, and S. Le Mouélic (2013). "Titan's surface and atmosphere from Cassini/VIMS data with updated methane opacity". In: *Icarus* 226, pp. 470–486. DOI: 10.1016/j.icarus.2013.05.033.

Hörst, S. M. (2017). "Titan's atmosphere and climate". In: *Journal of Geophysical Research (Planets)* 122, pp. 432–482. DOI: 10.1002/2016JE005240.

Hörst, S. M., R. V. Yelle, A. Buch, N. Carrasco, G. Cernogora, O. Dutuit, E. Quirico, E. Sciamma-O'Brien, M. A. Smith, Á. Somogyi, C. Szopa, R. Thissen, and V. Vuitton (2012). "Formation of Amino Acids and Nucleotide Bases in a Titan Atmosphere Simulation Experiment". In: *Astrobiology* 12, pp. 809–817. DOI: 10.1089/ast.2011.0623.

Hörst, S. M. and M. A. Tolbert (2014). "The Effect of Carbon Monoxide on Planetary Haze Formation". In: *ApJ* 781, p. 53. DOI: 10.1088/0004-637X/781/1/53.

Imanaka, H., D. P. Cruikshank, B. N. Khare, and C. P. McKay (2012). "Optical constants of Titan tholins at mid-infrared wavelengths (2.5-25 μm) and the possible chemical nature of Titan's haze particles". In: *Icarus* 218, pp. 247–261. DOI: 10.1016/j.icarus.2011.11.018.

Israelachvili, J. N. (2011). *Intermolecular and surface forces.* Academic press.

Iversen, J. D. and B. R. White (1982). "Saltation threshold on Earth, Mars and Venus". In: *Sedimentology* 29, pp. 111–119. DOI: 10.1111/j.1365-3091.1982.tb01713.x.

Iversen, J. D., J. B. Pollack, R. Greeley, and B. R. White (1976). "Saltation threshold on Mars - The effect of interparticle force, surface roughness, and low atmospheric density". In: *Icarus* 29, pp. 381–393. DOI: 10.1016/0019-1035(76)90140-8.

Iwamatsu, M. and K. Horii (1996). "Capillary Condensation and Adhesion of Two Wetter Surfaces". In: *Journal of Colloid and Interface Science* 182, pp. 400–406. DOI: 10.1006/jcis.1996.0480.

Janssen, M. A., R. D. Lorenz, R. West, F. Paganelli, R. M. Lopes, R. L. Kirk, C. Elachi, S. D. Wall, W. T. K. Johnson, Y. Anderson, R. A. Boehmer, P. Callahan, Y. Gim, G. A. Hamilton, K. D. Kelleher, L. Roth, B. Stiles, A. Le Gall, and the Cassini Radar Team (2009). "Titan's surface at 2.2-cm

wavelength imaged by the Cassini RADAR radiometer: Calibration and first results". In: *Icarus* 200, pp. 222–239. DOI: 10.1016/j.icarus.2008.10.017.

Jennings, D. E., F. M. Flasar, V. G. Kunde, R. E. Samuelson, J. C. Pearl, C. A. Nixon, R. C. Carlson, A. A. Mamoutkine, J. C. Brasunas, E. Guandique, R. K. Achterberg, G. L. Bjoraker, P. N. Romani, M. E. Segura, S. A. Albright, M. H. Elliott, J. S. Tingley, S. Calcutt, A. Coustenis, and R. Courtin (2009). "Titan's Surface Brightness Temperatures". In: *ApJL* 691, pp. L103–L105. DOI: 10.1088/0004-637X/691/2/L103.

Johnson, K. L., K. Kendall, and A. D. Roberts (1971). "Surface Energy and the Contact of Elastic Solids". In: *Proceedings of the Royal Society of London Series A* 324, pp. 301–313. DOI: 10.1098/rspa.1971.0141.

Jones, R., H. M. Pollock, J. A. Cleaver, and C. S. Hodges (2002). "Adhesion forces between glass and silicon surfaces in air studied by AFM: Effects of relative humidity, particle size, roughness, and surface treatment". In: *Langmuir* 18, pp. 8045–8055. DOI: 10.1021/la0259196.

Kirk, R. L., E. Howington-Kraus, B. Redding, P. S. Callahan, A. G. Hayes, A. Legall, R. M. C. Lopes, R. D. Lorenz, A. Lucas, K. L. Mitchell, C. D. Neish, O. Aharonson, J. Radebaugh, B. W. Stiles, E. R. Stofan, S. D. Wall, C. A. Wood, and Cassini RADAR Team (2012). "Topographic Mapping of Titan: Latest Results". In: *Lunar and Planetary Science Conference*. Vol. 43. Lunar and Planetary Inst. Technical Report, p. 2759.

Kok, J. F. (2010). "An improved parameterization of wind-blown sand flux on Mars that includes the effect of hysteresis". In: *Geophysical Research Letters* 37, p. L12202. DOI: 10.1029/2010GL043646.

Kok, J. F. and D. J. Lacks (2009). "Electrification of granular systems of identical insulators". In: *Physical Review E* 79.5, p. 051304. DOI: 10.1103/PhysRevE.79.051304.

Kok, J. F. and N. O. Renno (2009). "A comprehensive numerical model of steady state saltation (COMSALT)". In: *Journal of Geophysical Research (Atmospheres)* 114, p. D17204. DOI: 10.1029/2009JD011702.

Kok, J. F., E. J. R. Parteli, T. I. Michaels, and D. B. Karam (2012). "The physics of wind-blown sand and dust". In: *Reports on Progress in Physics* 75.10, p. 106901. DOI: 10.1088/0034-4885/75/10/106901.

Krabbe, K. (2014). *Fracture Toughness of Thin Films Estimated by Rockwell C Indentation.* Gistrup, Denmark: River Publishers.

Kuenen, P. H. (1960). "Experimental Abrasion 4: Eolian Action". In: *Journal of Geology* 68, pp. 427–449. DOI: 10.1086/626675.

Kunde, V. G., A. C. Aikin, R. A. Hanel, D. E. Jennings, W. C. Maguire, and R. E. Samuelson (1981). "C4H2, HC3N and C2N2 in Titan's atmosphere". In: *Nature* 292, pp. 686–688. DOI: 10.1038/292686a0.

Lancaster, N. (1982). "Dunes on the skeleton coast, Namibia (South West Africa): Geomorphology and grain size relationships". In: *Earth Surface Processes and Landforms* 7, pp. 575–587. DOI: 10.1002/esp.3290070606.

Lancaster, N. (1984). "Characteristics and occurrence of wind erosion features in the Namib Desert". In: *Earth Surface Processes and Landforms* 9, pp. 469–478. DOI: 10.1002/esp.3290090507.

Lancaster, N. (1995). *Geomorphology of Desert Dunes.* Routledge, London.

Lavvas, P., C. A. Griffith, and R. V. Yelle (2011). "Condensation in Titan's atmosphere at the Huygens landing site". In: *Icarus* 215, pp. 732–750. DOI: 10.1016/j.icarus.2011.06.040.

Lawn, B. R., A. G. Evans, and D. B. Marshall (1980). "Elastic/plastic indentation damage in ceramics: The median/radial crack system". In: *Journal of the American Ceramic Society* 63, 574âĂŞ581. DOI: 10.1111/j.1151-2916.1980.tb10768.

Lee, P. and P. C. Thomas (1995). "Longitudinal dunes on Mars: Relation to current wind regimes". In: *Journal of Geophysical Research* 100, pp. 5381–5395. DOI: 10.1029/95JE00225.

Le Mouélic, S., S. Rodriguez, R. Robidel, B. Rousseau, B. Seignovert, C. Sotin, J. W. Barnes, R. H. Brown, K. H. Baines, B. J. Buratti, R. N. Clark, P. D. Nicholson, P. Rannou, and T. Cornet (2018). "Mapping polar atmospheric features on Titan with VIMS: From the dissipation of the northern cloud to the onset of a southern polar vortex". In: *Icarus* 311, pp. 371–383. DOI: 10.1016/j.icarus.2018.04.028.

Lebonnois, S., J. Burgalat, P. Rannou, and B. Charnay (2012). "Titan global climate model: A new 3-dimensional version of the IPSL Titan GCM". In: *Icarus* 218, pp. 707–722. DOI: 10.1016/j.icarus.2011.11.032.

Le Gall, A., M. A. Janssen, L. C. Wye, A. G. Hayes, J. Radebaugh, C. Savage, H. Zebker, R. D. Lorenz, J. I. Lunine, R. L. Kirk, R. M. C. Lopes, S. Wall, P. Callahan, E. R. Stofan, T. Farr, and the Cassini Radar Team (2011). "Cassini SAR, radiometry, scatterometry and altimetry observations of Titan's dune fields". In: *Icarus* 213, pp. 608–624. DOI: 10.1016/j.icarus.2011.03.026.

Le Gall, A., M. J. Malaska, R. D. Lorenz, M. A. Janssen, T. Tokano, A. G. Hayes, M. Mastrogiuseppe, J. I. Lunine, G. Veyssière, P. Encrenaz, and O. Karatekin (2016). "Composition, seasonal change, and bathymetry of Ligeia Mare, Titan, derived from its microwave thermal emission". In:

Journal of Geophysical Research (Planets) 121, pp. 233–251. DOI: 10.1002/2015JE004920.

Le Mouélic, S., T. Cornet, S. Rodriguez, C. Sotin, B. Seignovert, J. W. Barnes, R. H. Brown, K. H. Baines, B. J. Buratti, R. N. Clark, P. D. Nicholson, J. Lasue, V. Pasek, and J. M. Soderblom (2019). "The Cassini VIMS archive of Titan: From browse products to global infrared color maps". In: *Icarus* 319, pp. 121–132. DOI: 10.1016/j.icarus.2018.09.017.

Liftshitz, E. (1956). "The theory of molecular attractive forces between solids". In: *Journal of Experimental and Theoretical Physics* 29, pp. 94–110.

Litwin, K. L., B. R. Zygielbaum, P. J. Polito, L. S. Sklar, and G. C. Collins (2012). "Influence of temperature, composition, and grain size on the tensile failure of water ice: Implications for erosion on Titan". In: *Journal of Geophysical Research (Planets)* 117, E08013. DOI: 10.1029/2012JE004101.

Lopes, R. M. C., K. L. Mitchell, E. R. Stofan, J. I. Lunine, R. Lorenz, F. Paganelli, R. L. Kirk, C. A. Wood, S. D. Wall, L. E. Robshaw, A. D. Fortes, C. D. Neish, J. Radebaugh, E. Reffet, S. J. Ostro, C. Elachi, M. D. Allison, Y. Anderson, R. Boehmer, G. Boubin, P. Callahan, P. Encrenaz, E. Flamini, G. Francescetti, Y. Gim, G. Hamilton, S. Hensley, M. A. Janssen, W. T. K. Johnson, K. Kelleher, D. O. Muhleman, G. Ori, R. Orosei, G. Picardi, F. Posa, L. E. Roth, R. Seu, S. Shaffer, L. A. Soderblom, B. Stiles, S. Vetrella, R. D. West, L. Wye, and H. A. Zebker (2007). "Cryovolcanic features on Titan's surface as revealed by the Cassini Titan Radar Mapper". In: *Icarus* 186, pp. 395–412. DOI: 10.1016/j.icarus.2006.09.006.

Lopes, R. M. C., E. R. Stofan, R. Peckyno, J. Radebaugh, K. L. Mitchell, G. Mitri, C. A. Wood, R. L. Kirk, S. D. Wall, J. I. Lunine, A. Hayes, R. Lorenz, T. Farr, L. Wye, J. Craig, R. J. Ollerenshaw, M. Janssen, A. Legall, F. Paganelli, R. West, B. Stiles, P. Callahan, Y. Anderson, P. Valora, L. Soderblom, and The Cassini Radar Team (2010). "Distribution and interplay of geologic processes on Titan from Cassini radar data". In: *Icarus* 205, pp. 540–558. DOI: 10.1016/j.icarus.2009.08.010.

Lopes, R. M. C., R. L. Kirk, K. L. Mitchell, A. Legall, J. W. Barnes, A. Hayes, J. Kargel, L. Wye, J. Radebaugh, E. R. Stofan, M. A. Janssen, C. D. Neish, S. D. Wall, C. A. Wood, J. I. Lunine, and M. J. Malaska (2013). "Cryovolcanism on Titan: New results from Cassini RADAR and VIMS". In: *Journal of Geophysical Research (Planets)* 118, pp. 416–435. DOI: 10.1002/jgre.20062.

Lopes, R. M. C., M. J. Malaska, A. Solomonidou, A. Le Gall, M. A. Janssen, C. D. Neish, E. P. Turtle, S. P. D. Birch, A. G. Hayes, J. Radebaugh, A. Coustenis, A. Schoenfeld, B. W. Stiles, R. L. Kirk, K. L. Mitchell, E. R. Stofan, K. J.

Lawrence, and The Cassini Radar Team (2016). "Nature, distribution, and origin of Titan's Undifferentiated Plains". In: *Icarus* 270, pp. 162–182. DOI: 10.1016/j.icarus.2015.11.034.

Lora, J. M., J. I. Lunine, J. L. Russell, and A. G. Hayes (2014). "Simulations of Titan's paleoclimate". In: *Icarus* 243, pp. 264–273. DOI: 10.1016/j.icarus.2014.08.042.

Lora, J. M., J. I. Lunine, and J. L. Russell (2015). "GCM simulations of Titan's middle and lower atmosphere and comparison to observations". In: *Icarus* 250, pp. 516–528. DOI: 10.1016/j.icarus.2014.12.030.

Lorenz, R. D. (2014). "Physics of saltation and sand transport on Titan: A brief review". In: *Icarus* 230, pp. 162–167. DOI: 10.1016/j.icarus.2013.06.023.

Lorenz, R. D. and J. Radebaugh (2009). "Global pattern of Titan's dunes: Radar survey from the Cassini prime mission". In: *Geophysical Research Letters* 36, p. L03202. DOI: 10.1029/2008GL036850.

Lorenz, R. D. and J. R. Zimbelman (2014). *Dune Worlds: How Windblown Sand Shapes Planetary Landscapes*. Heidelberg, New York: Springer Science & Business Media.

Lorenz, R. D., J. I. Lunine, J. A. Grier, and M. A. Fisher (1995). "Prediction of aeolian features on planets: Application to Titan paleoclimatology". In: *Journal of Geophysical Research* 100, pp. 26377–26386. DOI: 10.1029/95JE02708.

Lorenz, R. D., S. Wall, J. Radebaugh, G. Boubin, E. Reffet, M. Janssen, E. Stofan, R. Lopes, R. Kirk, C. Elachi, J. Lunine, K. Mitchell, F. Paganelli, L. Soderblom, C. Wood, L. Wye, H. Zebker, Y. Anderson, S. Ostro, M. Allison, R. Boehmer, P. Callahan, P. Encrenaz, G. G. Ori, G. Francescetti, Y. Gim, G. Hamilton, S. Hensley, W. Johnson, K. Kelleher, D. Muhleman, G. Picardi, F. Posa, L. Roth, R. Seu, S. Shaffer, B. Stiles, S. Vetrella, E. Flamini, and R. West (2006). "The Sand Seas of Titan: Cassini RADAR Observations of Longitudinal Dunes". In: *Science* 312, pp. 724–727. DOI: 10.1126/science.1123257.

Lorenz, R. D., C. A. Wood, J. I. Lunine, S. D. Wall, R. M. Lopes, K. L. Mitchell, F. Paganelli, Y. Z. Anderson, L. Wye, C. Tsai, H. Zebker, and E. R. Stofan (2007). "Titan's young surface: Initial impact crater survey by Cassini RADAR and model comparison". In: *Geophysical Research Letters* 34, p. L07204. DOI: 10.1029/2006GL028971.

Lorenz, R. D., K. L. Mitchell, R. L. Kirk, A. G. Hayes, O. Aharonson, H. A. Zebker, P. Paillou, J. Radebaugh, J. I. Lunine, M. A. Janssen, S. D. Wall, R. M. Lopes, B. Stiles, S. Ostro, G. Mitri, and E. R. Stofan (2008). "Titan's

inventory of organic surface materials". In: *Geophysical Research Letters* 35, p. L02206. DOI: 10.1029/2007GL032118.

Lorenz, R. D., P. Claudin, B. Andreotti, J. Radebaugh, and T. Tokano (2010). "A 3 km atmospheric boundary layer on Titan indicated by dune spacing and Huygens data". In: *Icarus* 205, pp. 719–721. DOI: 10.1016/j.icarus.2009.08.002.

Lowell, J. and W. S. Truscott (1986). "Triboelectrification of identical insulators. I. An experimental investigation". In: *Journal of Physics D Applied Physics* 19, pp. 1273–1280. DOI: 10.1088/0022-3727/19/7/017.

Lucas, A., O. Aharonson, C. Deledalle, A. G. Hayes, R. Kirk, and E. Howington-Kraus (2014b). "Insights into Titan's geology and hydrology based on enhanced image processing of Cassini RADAR data". In: *Journal of Geophysical Research (Planets)* 119, pp. 2149–2166. DOI: 10.1002/2013JE004584.

Lucas, A., S. Rodriguez, C. Narteau, B. Charnay, S. C. Pont, T. Tokano, A. Garcia, M. Thiriet, A. G. Hayes, R. D. Lorenz, and O. Aharonson (2014a). "Growth mechanisms and dune orientation on Titan". In: *Geophysical Research Letters* 41, pp. 6093–6100. DOI: 10.1002/2014GL060971.

Malaska, M. J., R. M. Lopes, A. G. Hayes, J. Radebaugh, R. D. Lorenz, and E. P. Turtle (2016). "Material transport map of Titan: The fate of dunes". In: *Icarus* 270, pp. 183–196. DOI: 10.1016/j.icarus.2015.09.029.

Malin, M. C. and K. S. Edgett (2001). "Mars Global Surveyor Mars Orbiter Camera: Interplanetary cruise through primary mission". In: *Journal of Geophysical Research* 106, pp. 23429–23570. DOI: 10.1029/2000JE001455.

Marshall, J. R. and R. Greeley (1992). "An experimental study of aeolian structures on Venus". In: *Journal of Geophysical Research* 97, pp. 1007–1016. DOI: 10.1029/91JE02862.

Mastrogiuseppe, M., V. Poggiali, R. Seu, R. Martufi, and C. Notarnicola (2014b). "Titan dune heights retrieval by using Cassini Radar Altimeter". In: *Icarus* 230, pp. 191–197. DOI: 10.1016/j.icarus.2013.09.028.

Mastrogiuseppe, M., V. Poggiali, A. Hayes, R. Lorenz, J. Lunine, G. Picardi, R. Seu, E. Flamini, G. Mitri, C. Notarnicola, P. Paillou, and H. Zebker (2014a). "The bathymetry of a Titan sea". In: *Geophysical Research Letters* 41, pp. 1432–1437. DOI: 10.1002/2013GL058618.

Maugis, D. (1992). "Adhesion of spheres: The JKR-DMT transition using a dugdale model". In: *Journal of Colloid and Interface Science* 150, pp. 243–269. DOI: 10.1016/0021-9797(92)90285-T.

McCord, T. B., G. B. Hansen, B. J. Buratti, R. N. Clark, D. P. Cruikshank, E. D'Aversa, C. A. Griffith, E. K. H. Baines, R. H. Brown, C. M. Dalle Ore,

G. Filacchione, V. Formisano, C. A. Hibbitts, R. Jaumann, J. I. Lunine, R. M. Nelson, C. Sotin, and the Cassini VIMS Team (2006). "Composition of Titan's surface from Cassini VIMS". In: *Planetary and Space Science* 54, pp. 1524–1539. DOI: 10.1016/j.pss.2006.06.007.

McDonald, G. D., A. G. Hayes, R. C. Ewing, J. M. Lora, C. E. Newman, T. Tokano, A. Lucas, A. Soto, and G. Chen (2016). "Variations in Titan's dune orientations as a result of orbital forcing". In: *Icarus* 270, pp. 197–210. DOI: 10.1016/j.icarus.2015.11.036.

McFarlane, J. S. and D. Tabor (1950). "Adhesion of Solids and the Effect of Surface Films". In: *Proceedings of the Royal Society of London Series A* 202, pp. 224–243. DOI: 10.1098/rspa.1950.0096.

McGuiggan, P. M., D. A. Grave, J. S. Wallace, S. Cheng, A. Prosperetti, and O. Robbins M (2011). "Dynamics of a disturbed sessile drop measured by atomic force microscopy (AFM)". In: *Langmuir* 27, pp. 11966–11972. DOI: 10.1021/la2023709.

McKay, C. P. (1996). "Elemental composition, solubility, and optical properties of Titan's organic haze". In: *Planetary and Space Science* 44, pp. 741–747. DOI: 10.1016/0032-0633(96)00009-8.

McKenna Neuman, C. M. (2003). "Effects of Temperature and Humidity upon the Entrainment of Sedimentary Particles by Wind". In: *Boundary-Layer Meteorology* 108, pp. 61–89. DOI: 10.1023/A:1023035201953.

McKenna Neuman, C. and S. Sanderson (2008). "Humidity control of particle emissions in aeolian systems". In: *Journal of Geophysical Research (Earth Surface)* 113, F02S14. DOI: 10.1029/2007JF000780.

MacKenzie, S. M., J. W. Barnes, C. Sotin, J. M. Soderblom, S. Le Mouélic, S. Rodriguez, K. H. Baines, B. J. Buratti, R. N. Clark, P. D. Nicholson, and T. B. McCord (2014). "Evidence of Titan's climate history from evaporite distribution". In: *icarus* 243, pp. 191–207. DOI: 10.1016/j.icarus.2014.08.022.

Méndez Harper, J. S., G. D. McDonald, J. Dufek, M. J. Malaska, D. M. Burr, A. G. Hayes, J. McAdams, and J. J. Wray (2017). "Electrification of sand on Titan and its influence on sediment transport". In: *Nature Geoscience* 10, pp. 260–265. DOI: 10.1038/ngeo2921.

Merrison, J. P. (2012). "Sand transport, erosion and granular electrification". In: *Aeolian Research* 4, pp. 1–16. DOI: 10.1016/j.aeolia.2011.12.003.

Merrison, J. P., H. P. Gunnlaugsson, M. R. Hogg, M. Jensen, J. M. Lykke, M. B. Madsen, M. B. Nielsen, P. Nørnberg, T. A. Ottosen, R. T. Pedersen, S. Pedersen, and A. V. Sørensen (2012). "Factors affecting the electrification

of wind-driven dust studied with laboratory simulations". In: *Planetary and Space Science* 60, pp. 328–335. DOI: 10.1016/j.pss.2011.10.008.

Meyers, M. A. and K. K. Chawla (2009). *Mechanical Behavior of Materials*. New York: Cambridge University Press.

Mitchell, J. L. (2008). "The drying of Titan's dunes: Titan's methane hydrology and its impact on atmospheric circulation". In: *Journal of Geophysical Research (Planets)* 113, E08015. DOI: 10.1029/2007JE003017.

Miqueu, C., D. Broseta, J. Satherley, B. Mendiboure, J. Lachaise, and A. Graciaa (2000). "An extended scaled equation for the temperature dependence of the surface tension of pure compounds inferred from an analysis of experimental data". In: *Fluid Phase Equilib.* 172, pp. 169–182. DOI: 10.1016/S0378-3812(00)00384-8.

Mitchell, J. L. and J. M. Lora (2016). "The Climate of Titan". In: *Annual Review of Earth and Planetary Sciences* 44, pp. 353–380. DOI: 10.1146/annurev-earth-060115-012428.

Mitchell, J. L., R. T. Pierrehumbert, D. M. Frierson, and R. Caballero (2006). "The Dynamics Behind Titan's Methane Clouds". In: *AAS/Division for Planetary Sciences Meeting Abstracts #38*. Vol. 38. Bulletin of the American Astronomical Society, p. 531.

Mitchell, J. L., R. T. Pierrehumbert, D. M. W. Frierson, and R. Caballero (2009). "The impact of methane thermodynamics on seasonal convection and circulation in a model Titan atmosphere". In: *Icarus* 203, pp. 250–264. DOI: 10.1016/j.icarus.2009.03.043.

Mitri, G., M. T. Bland, A. P. Showman, J. Radebaugh, B. Stiles, R. M. C. Lopes, J. I. Lunine, and R. T. Pappalardo (2010). "Mountains on Titan: Modeling and observations". In: *Journal of Geophysical Research (Planets)* 115, E10002. DOI: 10.1029/2010JE003592.

Moore, J. M. and R. T. Pappalardo (2011). "Titan: An exogenic world?" In: *Icarus* 212, pp. 790–806. DOI: 10.1016/j.icarus.2011.01.019.

Mousis, O. and B. Schmitt (2008). "Sequestration of Ethane in the Cryovolcanic Subsurface of Titan". In: *ApJL* 677, p. L67. DOI: 10.1086/587141.

Neish, C. D., R. D. Lorenz, R. L. Kirk, and L. C. Wye (2010). "Radarclinometry of the sand seas of Africa's Namibia and Saturn's moon Titan". In: *Icarus* 208, pp. 385–394. DOI: 10.1016/j.icarus.2010.01.023.

Neish, C. D. and R. D. Lorenz (2012). "Titan's global crater population: A new assessment". In: *Planetary and Space Science* 60, pp. 26–33. DOI: 10.1016/j.pss.2011.02.016.

Newman, C. E., C. Lee, Y. Lian, M. I. Richardson, and A. D. Toigo (2011). "Stratospheric superrotation in the TitanWRF model". In: *Icarus* 213, pp. 636–654. DOI: 10.1016/j.icarus.2011.03.025.

Nield, E. V., D. M. Burr, N. T. Bridges, J. K. Smith, J. P. Emery, J. R. Marshall, and J. F. Kok (2016). "A Wind Tunnel Study of the Effect of Pressure on Saltation Threshold Conditions". In: *Lunar and Planetary Science Conference*. Vol. 47. Lunar and Planetary Inst. Technical Report, p. 1028.

Nixon, C. A., D. E. Jennings, B. Bézard, S. Vinatier, N. A. Teanby, K. Sung, T. M. Ansty, P. G. J. Irwin, N. Gorius, V. Cottini, A. Coustenis, and F. M. Flasar (2013). "Detection of Propene in Titan's Stratosphere". In: *ApJL* 776, p. L14. DOI: 10.1088/2041-8205/776/1/L14.

Nourbakhsh, A., F. F. Baghlani, and A. Ashori (2011). "Nano-SiO2 filled rice husk/polypropylene composites: Physico-mechanical properties". In: *Industrial Crops and Products* 33, pp. 183–187. DOI: 10.1016/j.indcrop.2010.10.010.

Oliver, W. C. and G. M. Pharr (1992). "An improved technique for determining hardness and elastic modulus using load and displacement sensing indentation experiments". In: *Journal of Materials Research* 7, pp. 1564–1583. DOI: 10.1557/JMR.1992.1564.

Oliver, W. C. and G. M. Pharr (2004). "Measurement of hardness and elastic modulus by instrumented indentation: Advances in understanding and refinements to methodology". In: *Journal of Materials Research* 19, pp. 3–20. DOI: 10.1557/jmr.2004.19.1.3.

Owen, P. R. (1964). "Saltation of uniform grains in air". In: *Journal of Fluid Mechanics* 20, pp. 225–242. DOI: 10.1017/S0022112064001173.

Owens, D. K. and R. C. Wendt (1969). "Estimation of the surface free energy of polymers". In: *Journal of Applied Polymer Science* 13.

Paganelli, F., M. A. Janssen, B. Stiles, R. West, R. D. Lorenz, J. I. Lunine, S. D. Wall, P. Callahan, R. M. Lopes, E. Stofan, R. L. Kirk, W. T. K. Johnson, L. Roth, C. Elachi, and the Radar Team (2007). "Titan's surface from Cassini RADAR SAR and high resolution radiometry data of the first five flybys". In: *Icarus* 191, pp. 211–222. DOI: 10.1016/j.icarus.2007.04.032.

Paganelli, F., M. A. Janssen, R. M. Lopes, E. Stofan, S. D. Wall, R. D. Lorenz, J. I. Lunine, R. L. Kirk, L. Roth, C. Elachi, and Cassini Radar Team (2008). "Titan's surface from the Cassini RADAR radiometry data during SAR mode". In: *Planetary and Space Science* 56, pp. 100–108. DOI: 10.1016/j.pss.2007.03.015.

Pähtz, T. and O. Durán (2016). "Transport-threshold model suggests sand transport by wind on Triton, Pluto, and 67P/CG". In: *Atmos. Oceanic Phys.*

Parsons, D. F., R. B. Walsh, and V. S. J. Craig (2014). "Surface forces: Surface roughness in theory and experiment". In: *The Journal of Chemical Physics* 140.16, p. 164701. DOI: 10.1063/1.4871412.

Persson, B. N. (2002). "Adhesion between Elastic Bodies with Randomly Rough Surfaces". In: *Physical Review Letters* 89.24, p. 245502. DOI: 10.1103/PhysRevLett.89.245502.

Petrenko, V. F. and R. W. Whitworth. *Physics of ice*. Oxford: OUP.

Pirayesh, H., A. Khazaeian, and T. Tabarsa (2012). "The potential for using walnut (juglans regia l.) shell as a raw material for wood-based particleboard manufacturing". In: *Composites Part B* 43, pp. 3276–3280. DOI: 10.1016/j.compositesb.2012.02.016.

Porco, C. C., E. Baker, J. Barbara, K. Beurle, A. Brahic, J. A. Burns, S. Charnoz, N. Cooper, D. D. Dawson, A. D. Del Genio, T. Denk, L. Dones, U. Dyudina, M. W. Evans, S. Fussner, B. Giese, K. Grazier, P. Helfenstein, A. P. Ingersoll, R. A. Jacobson, T. V. Johnson, A. McEwen, C. D. Murray, G. Neukum, W. M. Owen, J. Perry, T. Roatsch, J. Spitale, S. Squyres, P. Thomas, M. Tiscareno, E. P. Turtle, A. R. Vasavada, J. Veverka, R. Wagner, and R. West (2005). "Imaging of Titan from the Cassini spacecraft". In: *Nature* 434, pp. 159–168. DOI: 10.1038/nature03436.

Proctor, T. M. (1966). "Low-Temperature Speed of Sound in Single-Crystal Ice". In: *Acoustical Society of America Journal* 39, p. 972. DOI: 10.1121/1.1909980.

Quirico, E., C. Szopa, G. Cernogora, V. Lees, S. Derenne, P. F. McMillan, G. Montagnac, B. Reynard, J.-N. Rouzaud, N. Fray, P. Coll, F. Raulin, B. Schmitt, and B. Minard (2008). "Tholins and their relevance for astrophysical issues". In: *Organic Matter in Space*. Vol. 251. IAU Symposium, pp. 409–416. DOI: 10.1017/S1743921308022059.

Rabinovich, Y. I., J. J. Adler, A. Ata, R. K. Singh, and B. M. Moudgil (2000). "Adhesion between Nanoscale Rough Surfaces". In: *Journal of Colloid and Interface Science* 232, pp. 10–16. DOI: 10.1006/jcis.2000.7167.

Radebaugh, J., R. D. Lorenz, R. L. Kirk, J. I. Lunine, E. R. Stofan, R. M. C. Lopes, S. D. Wall, and the Cassini Radar Team (2007). "Mountains on Titan observed by Cassini Radar". In: *Icarus* 192, pp. 77–91. DOI: 10.1016/j.icarus.2007.06.020.

Radebaugh, J., R. D. Lorenz, J. I. Lunine, S. D. Wall, G. Boubin, E. Reffet, R. L. Kirk, R. M. Lopes, E. R. Stofan, L. Soderblom, M. Allison, M. Janssen, P. Paillou, P. Callahan, C. Spencer, and the Cassini Radar Team (2008).

"Dunes on Titan observed by Cassini Radar". In: *Icarus* 194, pp. 690–703. DOI: 10.1016/j.icarus.2007.10.015.

Radebaugh, J., R. Lorenz, T. Farr, P. Paillou, C. Savage, and C. Spencer (2010). "Linear dunes on Titan and earth: Initial remote sensing comparisons". In: *Geomorphology* 121, pp. 122–132. DOI: 10.1016/j.geomorph.2009.02.022.

Rannou, P., F. Montmessin, F. Hourdin, and S. Lebonnois (2006). "The Latitudinal Distribution of Clouds on Titan". In: *Science* 311, pp. 201–205. DOI: 10.1126/science.1118424.

Rasmussen, K. R., J. F. Kok, and J. P. Merrison (2009). "Enhancement in wind-driven sand transport by electric fields". In: *Planetary and Space Science* 57, pp. 804–808. DOI: 10.1016/j.pss.2009.03.001.

Raulin, F. (1987). "Organic chemistry in the oceans of Titan". In: *Advances in Space Research* 7, pp. 71–81. DOI: 10.1016/0273-1177(87)90358-9.

Ravi, S., P. D'Odorico, T. M. Over, and T. M. Zobeck (2004). "On the effect of air humidity on soil susceptibility to wind erosion: The case of air-dry soils". In: *Geophysical Research Letters* 31, p. L09501. DOI: 10.1029/2004GL019485.

Ravi, S., T. M. Zobeck, T. M. Over, G. S. Okin, and P. D'Odorico (2006). "On the effect of moisture bonding forces in air-dry soils on threshold friction velocity of wind erosion". In: *Sedimentology* 53, pp. 597–609. DOI: 10.1111/j.1365-3091.2006.00775.x.

Rodriguez, S., S. Le Mouélic, P. Rannou, G. Tobie, K. H. Baines, J. W. Barnes, C. A. Griffith, M. Hirtzig, K. M. Pitman, C. Sotin, R. H. Brown, B. J. Buratti, R. N. Clark, and P. D. Nicholson (2009). "Global circulation as the main source of cloud activity on Titan". In: *Nature* 459, pp. 678–682. DOI: 10.1038/nature08014.

Rodriguez, S., S. Le Mouélic, P. Rannou, C. Sotin, R. H. Brown, J. W. Barnes, C. A. Griffith, J. Burgalat, K. H. Baines, B. J. Buratti, R. N. Clark, and P. D. Nicholson (2011). "Titan's cloud seasonal activity from winter to spring with Cassini/VIMS". In: *Icarus* 216, pp. 89–110. DOI: 10.1016/j.icarus.2011.07.031.

Rodriguez, S., A. Garcia, A. Lucas, T. Appéré, A. Le Gall, E. Reffet, L. Le Corre, S. Le Mouélic, T. Cornet, S. Courrech du Pont, C. Narteau, O. Bourgeois, J. Radebaugh, K. Arnold, J. W. Barnes, K. Stephan, R. Jaumann, C. Sotin, R. H. Brown, R. D. Lorenz, and E. P. Turtle (2014). "Global mapping and characterization of Titan's dune fields with Cassini: Correlation between RADAR and VIMS observations". In: *Icarus* 230, pp. 168–179. DOI: 10.1016/j.icarus.2013.11.017.

Rodriguez, S., S. Le Mouélic, J. W. Barnes, J. F. Kok, S. C. R. Rafkin, R. D. Lorenz, B. Charnay, J. Radebaugh, C. Narteau, T. Cornet, O. Bourgeois, A. Lucas, P. Rannou, C. A. Griffith, A. Coustenis, T. Appéré, M. Hirtzig, C. Sotin, J. M. Soderblom, R. H. Brown, J. Bow, G. Vixie, L. Maltagliati, S. Courrech du Pont, R. Jaumann, K. Stephan, K. H. Baines, B. J. Buratti, R. N. Clark, and P. D. Nicholson (2018). "Observational evidence for active dust storms on Titan at equinox". In: *Nature Geoscience* 11, pp. 727–732. DOI: 10.1038/s41561-018-0233-2.

Rubin, D. M. and P. A. Hesp (2009). "Multiple origins of linear dunes on Earth and Titan". In: *Nature Geoscience* 2, pp. 653–658. DOI: 10.1038/ngeo610.

Rubin, D. M. and H. Ikeda (1990). "Flume experiments on the alignment of transverse, oblique, and longitudinal dunes in directionally varying flows". In: *Sedimentology* 37, pp. 673–684. DOI: 10.1111/j.1365-3091.1990.tb00628.x.

Rumpf, H. *Particle technology*. London: Chapman and Hall.

Sagan, C. and B. N. Khare (1979). "Tholins - Organic chemistry of interstellar grains and gas". In: *Nature* 277, pp. 102–107. DOI: 10.1038/277102a0.

Sagan, C., B. N. Khare, W. R. Thompson, G. D. McDonald, M. R. Wing, J. L. Bada, T. Vo-Dinh, and E. T. Arakawa (1993). "Polycyclic aromatic hydrocarbons in the atmospheres of Titan and Jupiter". In: *ApJ* 414, pp. 399–405. DOI: 10.1086/173086.

Sakurada, I. and K. Keisuke (1975). "Relation between the crystal structure of polymers and the elastic modulus of polymer crystals in the direction perpendicular to the chain axis". In: *Macromolecular Chemistry and Physics* 1.

Sarker, N., A. Somogyi, J. I. Lunine, and M. A. Smith (2003). "Titan Aerosol Analogues: Analysis of the Nonvolatile Tholins". In: *Astrobiology* 3, pp. 719–726. DOI: 10.1089/153110703322736042.

Savage, C. J., J. Radebaugh, E. H. Christiansen, and R. D. Lorenz (2014). "Implications of dune pattern analysis for Titan's surface history". In: *Icarus* 230, pp. 180–190. DOI: 10.1016/j.icarus.2013.08.009.

Schaefer, D. M., M. Carpenter, B. Gady, R. Reifenberger, L. P. Demejo, and D. S. Rimai (1995). "Surface roughness and its influence on particle adhesion using atomic force techniques". In: *Journal of adhesion science and technology* 9, pp. 1049–1062. DOI: 10.1163/156856195X00897.

Schmidt, D. S., R. A. Schmidt, and J. D. Dent (1998). "Electrostatic force on saltating sand". In: *Journal of Geophysical Research: Atmospheres* 103, pp. 8997–9001. DOI: 10.1029/98JD00278.

Schneider, T., S. D. B. Graves, E. L. Schaller, and M. E. Brown (2012). "Polar methane accumulation and rainstorms on Titan from simulations of the methane cycle". In: *Nature* 481, pp. 58–61. DOI: 10.1038/nature10666.

Sears, W. D. (1995). "Tidal dissipation in oceans on Titan". In: *Icarus* 113, pp. 39–56. DOI: 10.1006/icar.1995.1004.

Selah, A. and D. W. Fryrear (1995). "Threshold Wind Velocities of Wet Soils as Affected by Wind Blown Sand". In: *Soil Science* 160, pp. 304–309. DOI: 10.1097/00010694-199510000-00009.

Shao, Y. and H. Lu (2000). "A simple expression for wind erosion threshold friction velocity". In: *Journal of Geophysical Research: Atmospheres* 105, p. 22. DOI: 10.1029/2000JD900304.

Singh, S., J.-P. Combe, D. Cordier, A. Wagner, V. F. Chevrier, and Z. McMahon (2017). "Experimental determination of acetylene and ethylene solubility in liquid methane and ethane: Implications to Titan's surface". In: *Geochimica et Cosmochimica Acta* 208, pp. 86–101. DOI: 10.1016/j.gca.2017.03.007.

Smith, B. A., L. A. Soderblom, D. Banfield, C. Barnet, A. T. Basilevksy, R. F. Beebe, K. Bollinger, J. M. Boyce, A. Brahic, G. A. Briggs, R. H. Brown, C. Chyba, S. A. Collins, T. Colvin, A. F. Cook, D. Crisp, S. K. Croft, D. Cruikshank, J. N. Cuzzi, G. E. Danielson, M. E. Davies, E. de Jong, L. Dones, D. Godfrey, J. Goguen, I. Grenier, V. R. Haemmerle, H. Hammel, C. J. Hansen, C. P. Helfenstein, C. Howell, G. E. Hunt, A. P. Ingersoll, T. V. Johnson, J. Kargel, R. Kirk, D. I. Kuehn, S. Limaye, H. Masursky, A. McEwen, D. Morrison, T. Owen, W. Owen, J. B. Pollack, C. C. Porco, K. Rages, P. Rogers, D. Rudy, C. Sagan, J. Schwartz, E. M. Shoemaker, M. Showalter, B. Sicardy, D. Simonelli, J. Spencer, L. A. Sromovsky, C. Stoker, R. G. Strom, V. E. Suomi, S. P. Synott, R. J. Terrile, P. Thomas, W. R. Thompson, A. Verbiscer, and J. Veverka (1989). "Voyager 2 at Neptune: Imaging Science Results". In: *Science* 246, pp. 1422–1449. DOI: 10.1126/science.246.4936.1422.

Soderblom, L. A., R. L. Kirk, J. I. Lunine, J. A. Anderson, K. H. Baines, J. W. Barnes, J. M. Barrett, R. H. Brown, B. J. Buratti, R. N. Clark, D. P. Cruikshank, C. Elachi, M. A. Janssen, R. Jaumann, E. Karkoschka, S. Le Mouélic, R. M. Lopes, R. D. Lorenz, T. B. McCord, P. D. Nicholson, J. Radebaugh, B. Rizk, C. Sotin, E. R. Stofan, T. L. Sucharski, M. G. Tomasko, and S. D. Wall (2007). "Correlations between Cassini VIMS spectra and RADAR SAR images: Implications for Titan's surface composition and the character of the Huygens Probe Landing Site". In: *Planetary and Space Science* 55, pp. 2025–2036. DOI: 10.1016/j.pss.2007.04.014.

Solomonidou, A., M. Hirtzig, A. Coustenis, E. Bratsolis, S. Le Mouélic, S. Rodriguez, K. Stephan, P. Drossart, C. Sotin, R. Jaumann, R. H. Brown, K. Kyriakopoulos, R. M. C. Lopes, G. Bampasidis, K. Stamatelopoulou-Seymour, and X. Moussas (2014). "Surface albedo spectral properties of geologically interesting areas on Titan". In: *Journal of Geophysical Research (Planets)* 119, pp. 1729–1747. DOI: 10.1002/2014JE004634.

Solomonidou, A., A. Coustenis, M. Hirtzig, S. Rodriguez, K. Stephan, R. M. C. Lopes, P. Drossart, C. Sotin, S. Le Mouélic, K. Lawrence, E. Bratsolis, R. Jaumann, and R. H. Brown (2016). "Temporal variations of Titan's surface with Cassini/VIMS". In: *Icarus* 270, pp. 85–99. DOI: 10.1016/j.icarus.2015.05.003.

Solomonidou, A., A. Coustenis, R. M. C. Lopes, M. J. Malaska, S. Rodriguez, P. Drossart, C. Elachi, B. Schmitt, S. Philippe, M. Janssen, M. Hirtzig, S. Wall, C. Sotin, K. Lawrence, N. Altobelli, E. Bratsolis, J. Radebaugh, K. Stephan, R. H. Brown, S. Le Mouélic, A. Le Gall, E. V. Villanueva, J. F. Brossier, A. A. Bloom, O. Witasse, C. Matsoukas, and A. Schoenfeld (2018). "The Spectral Nature of Titan's Major Geomorphological Units: Constraints on Surface Composition". In: *Journal of Geophysical Research (Planets)* 123, pp. 489–507. DOI: 10.1002/2017JE005477.

Stofan, E. R., C. Elachi, J. I. Lunine, R. D. Lorenz, B. Stiles, K. L. Mitchell, S. Ostro, L. Soderblom, C. Wood, H. Zebker, S. Wall, M. Janssen, R. Kirk, R. Lopes, F. Paganelli, J. Radebaugh, L. Wye, Y. Anderson, M. Allison, R. Boehmer, P. Callahan, P. Encrenaz, E. Flamini, G. Francescetti, Y. Gim, G. Hamilton, S. Hensley, W. T. K. Johnson, K. Kelleher, D. Muhleman, P. Paillou, G. Picardi, F. Posa, L. Roth, R. Seu, S. Shaffer, S. Vetrella, and R. West (2007). "The lakes of Titan". In: *Nature* 445, pp. 61–64. DOI: 10.1038/nature05438.

Taylor, c. j., L. E. Dieker, K. T. Miller, C. A. Koh, and E. D. Sloan (2008). "Hydrate particles adhesion force measurements: Effects of temperature, low dosage inhibitors, and interfacial energy". In: *In Proceedings of the 6th International Conference on Gas Hydrates. In Proceedings of the 6th International Conference on Gas Hydrates. Vancouver, British Columbia, Canada: ICGH.*

Telfer, M. W., E. J. R. Parteli, J. Radebaugh, R. A. Beyer, T. Bertrand, F. Forget, F. Nimmo, W. M. Grundy, J. M. Moore, S. A. Stern, J. Spencer, T. R. Lauer, A. M. Earle, R. P. Binzel, H. A. Weaver, C. B. Olkin, L. A. Young, K. Ennico, K. Runyon, and aff12 (2018). "Dunes on Pluto". In: *Science* 360, pp. 992–997. DOI: 10.1126/science.aao2975.

Thomas, N., H. Sierks, C. Barbieri, P. L. Lamy, R. Rodrigo, H. Rickman, D. Koschny, H. U. Keller, J. Agarwal, M. F. A'Hearn, F. Angrilli, A.-T. Auger, M. A. Barucci, J.-L. Bertaux, I. Bertini, S. Besse, D. Bodewits, G. Cremonese, V. Da Deppo, B. Davidsson, M. De Cecco, S. Debei, M. R. El-Maarry, F. Ferri, S. Fornasier, M. Fulle, L. Giacomini, O. Groussin, P. J. Gutierrez, C. Güttler, S. F. Hviid, W.-H. Ip, L. Jorda, J. Knollenberg, J.-R. Kramm, E. Kührt, M. Küppers, F. La Forgia, L. M. Lara, M. Lazzarin, J. J. L. Moreno, S. Magrin, S. Marchi, F. Marzari, M. Massironi, H. Michalik, R. Moissl, S. Mottola, G. Naletto, N. Oklay, M. Pajola, A. Pommerol, F. Preusker, L. Sabau, F. Scholten, C. Snodgrass, C. Tubiana, J.-B. Vincent, and K.-P. Wenzel (2015). "The morphological diversity of comet 67P/Churyumov-Gerasimenko". In: *Science* 347.1, aaa0440. DOI: 10.1126/science.aaa0440.

Tokano, T. and F. M. Neubauer (2002). "Tidal Winds on Titan Caused by Saturn". In: *Icarus* 158, pp. 499–515. DOI: 10.1006/icar.2002.6883.

Tokano, T. (2008). "Dune-forming winds on Titan and the influence of topography". In: *Icarus* 194, pp. 243–262. DOI: 10.1016/j.icarus.2007.10.007.

Tokano, T. (2010). "Relevance of fast westerlies at equinox for the eastward elongation of Titan's dunes". In: *Aeolian Research* 2, pp. 113–127. DOI: 10.1016/j.aeolia.2010.04.003.

Tomasko, M. G., B. Archinal, T. Becker, B. Bézard, M. Bushroe, M. Combes, D. Cook, A. Coustenis, C. de Bergh, L. E. Dafoe, L. Doose, S. Douté, A. Eibl, S. Engel, F. Gliem, B. Grieger, K. Holso, E. Howington-Kraus, E. Karkoschka, H. U. Keller, R. Kirk, R. Kramm, M. Küppers, P. Lanagan, E. Lellouch, M. Lemmon, J. Lunine, E. McFarlane, J. Moores, G. M. Prout, B. Rizk, M. Rosiek, P. Rueffer, S. E. Schröder, B. Schmitt, C. See, P. Smith, L. Soderblom, N. Thomas, and R. West (2005). "Rain, winds and haze during the Huygens probe's descent to Titan's surface". In: *Nature* 438, pp. 765–778. DOI: 10.1038/nature04126.

Tsoar, H. (1983). "Dynamic processes acting on a longitudinal (seif) sand dune". In: *Sedimentology* 30, pp. 567–578. DOI: 10.1111/j.1365-3091.1983.tb00694.x.

Tuller, M. and D. Or (2005). "Water films and scaling of soil characteristic curves at low water contents". In: *Water Resources Research* 41, p. 09403. DOI: 10.1029/2005WR004142.

Turtle, E. P., J. E. Perry, A. S. McEwen, A. D. Del Genio, J. Barbara, R. A. West, D. D. Dawson, and C. C. Porco (2009). "Cassini imaging of Titan's high-latitude lakes, clouds, and south-polar surface changes". In: *Geophysical Research Letters* 36, p. L02204. DOI: 10.1029/2008GL036186.

Turtle, E. P., A. D. Del Genio, J. M. Barbara, J. E. Perry, E. L. Schaller, A. S. McEwen, R. A. West, and T. L. Ray (2011b). "Seasonal changes in Titan's meteorology". In: *Geophysical Research Letters* 38, p. L03203. DOI: 10.1029/2010GL046266.

Turtle, E. P., J. E. Perry, A. G. Hayes, R. D. Lorenz, J. W. Barnes, A. S. McEwen, R. A. West, A. D. Del Genio, J. M. Barbara, J. I. Lunine, E. L. Schaller, T. L. Ray, R. M. C. Lopes, and E. R. Stofan (2011a). "Rapid and Extensive Surface Changes Near Titan's Equator: Evidence of April Showers". In: *Science* 331, p. 1414. DOI: 10.1126/science.1201063.

Turtle, E. P., J. E. Perry, J. M. Barbara, A. D. Del Genio, S. Rodriguez, S. Le Mouélic, C. Sotin, J. M. Lora, S. Faulk, P. Corlies, J. Kelland, S. M. MacKenzie, R. A. West, A. S. McEwen, J. I. Lunine, J. Pitesky, T. L. Ray, and M. Roy (2018). "Titan's Meteorology Over the Cassini Mission: Evidence for Extensive Subsurface Methane Reservoirs". In: *Geophysical Research Letters* 45, pp. 5320–5328. DOI: 10.1029/2018GL078170.

Vinatier, S., B. Bézard, S. Lebonnois, N. A. Teanby, R. K. Achterberg, N. Gorius, A. Mamoutkine, E. Guandique, A. Jolly, D. E. Jennings, and F. M. Flasar (2015). "Seasonal variations in Titan's middle atmosphere during the northern spring derived from Cassini/CIRS observations". In: *Icarus* 250, pp. 95–115. DOI: 10.1016/j.icarus.2014.11.019.

von Holstein-Rathlou, C., J. P. Merrison, C. F. Brædstrup, and P. Nørnberg (2012). "The effects of electric fields on wind driven particulate detachment". In: *Icarus* 220, pp. 1–5. DOI: 10.1016/j.icarus.2012.04.011.

Waite, J. H., H. Niemann, R. V. Yelle, W. T. Kasprzak, T. E. Cravens, J. G. Luhmann, R. L. McNutt, W.-H. Ip, D. Gell, V. De La Haye, I. Müller-Wordag, B. Magee, N. Borggren, S. Ledvina, G. Fletcher, E. Walter, R. Miller, S. Scherer, R. Thorpe, J. Xu, B. Block, and K. Arnett (2005). "Ion Neutral Mass Spectrometer Results from the First Flyby of Titan". In: *Science* 308, pp. 982–986. DOI: 10.1126/science.1110652.

Waite, J. H., D. T. Young, T. E. Cravens, A. J. Coates, F. J. Crary, B. Magee, and J. Westlake (2007). "The Process of Tholin Formation in Titan's Upper Atmosphere". In: *Science* 316, p. 870. DOI: 10.1126/science.1139727.

Webb, P. A. (2001). "Volume and density determinations for particle technologists". In: *Micromeritics Instrum. Corp* 2.

Weitz, C. M., J. J. Plaut, R. Greeley, and R. S. Saunders (1994). "Dunes and microdunes on Venus: Why were so few found in the Magellan data?" In: *Icarus* 112, pp. 282–295. DOI: 10.1006/icar.1994.1181.

Wood, C. A., R. Lorenz, R. Kirk, R. Lopes, K. Mitchell, E. Stofan, and Cassini Radar Team (2010). "Impact craters on Titan". In: *Icarus* 206, pp. 334–344. DOI: 10.1016/j.icarus.2009.08.021.

Wu, S. (1971). "Calculation of interfacial tension in polymer systems". In: *Journal of Polymer Science* 34, pp. 19–30. DOI: 10.1002/polc.5070340105.

Xie, H. Y. (1997). "The role of interparticle forces in the fluidization of fine particles". In: *Powder Technology* 94, pp. 99–108. DOI: 10.1016/S0032-5910(97)03270-1.

Yang, S.-o., D. M. Kleehammer, Z. Huo, E. D. Sloan, and K. T. Miller (2004). "Temperature dependence of particle-particle adherence forces in ice and clathrate hydrates". In: *Journal of Colloid and Interface Science* 277, pp. 335–341. DOI: 10.1016/j.jcis.2004.04.049.

Yang, C., B. N. J. Persson, J. Israelachvili, and K. Rosenberg (2008). "Contact mechanics with adhesion: Interfacial separation and contact area". In: *EPL (Europhysics Letters)* 84, p. 46004. DOI: 10.1209/0295-5075/84/46004.

Yung, Y. L., M. Allen, and J. P. Pinto (1984). "Photochemistry of the atmosphere of Titan - Comparison between model and observations". In: *Astrophysical Journal Supplement Series* 55, pp. 465–506. DOI: 10.1086/190963.

Yu, X., S. M. Hörst, C. He, N. T. Bridges, D. M. Burr, J. A. Sebree, and J. K. Smith (2017b). "The effect of adsorbed liquid and material density on saltation threshold: Insight from laboratory and wind tunnel experiments". In: *Icarus* 297, pp. 97–109. DOI: 10.1016/j.icarus.2017.06.034.

Yu, X., S. M. Hörst, C. He, P. McGuiggan, and N. T. Bridges (2017a). "Direct Measurement of Interparticle Forces of Titan Aerosol Analogs ("Tholin") Using Atomic Force Microscopy". In: *Journal of Geophysical Research (Planets)* 122, pp. 2610–2622. DOI: 10.1002/2017JE005437.

Yu, X., S. M. Hörst, C. He, P. McGuiggan, and B. Crawford (2018). "Where Does Titan Sand Come From: Insight From Mechanical Properties of Titan Sand Candidates". In: *Journal of Geophysical Research (Planets)* 123, pp. 2310–2321. DOI: 10.1029/2018JE005651.

Xinting Yu

Department of Earth and Planetary Sciences, Olin Hall
3400 N. Charles Street, Baltimore, MD 21218 – USA
✉ xyu33@jhu.edu • www.xintingyu.com • JonesKuma

Education

Johns Hopkins University — **Baltimore, MD, USA**
Candidate of PhD in Planetary Sciences — *2014-Present*

University of Science and Technology of China — **Hefei, Anhui, China**
BS in Space Physics with honors — *2010-2014*

Research Experience

University of California, Santa Cruz — **Santa Cruz, CA**
51 Pegasi b Postdoctoral Fellow (Supervisor: Xi Zhang) — *Starting July, 2019*
Laboratory production of exoplanet aerosol analogs ("tholins"), material property characterization, exoplanet microphysics modeling

Johns Hopkins University — **Baltimore, MD**
Graduate Research Assistant (Advisor: Sarah Hörst) — *2014–Present*
Laboratory production of Titan aerosol analogs ("tholins"), material characterization (interparticle forces and mechanical properties), study the origin and evolution of aeolian process on Titan

NASA Ames Research Center — **Mountain View, CA**
Visiting Student (Collaborators: Nathan Bridges, Devon Burr, James Smith) — *2015 & 2016 Summer*
Study aeolian processes on Titan using Titan Wind Tunnel

Key Laboratory of Solar Activity, National Astronomical Observatories — **Beijing, China**
Undergraduate Research Assistant (Advisor: Jun Zhang) — *2013–2014*
Investigation of cyclones in the Sun using data from SDO/AIA and HMI

Honors and Awards

- 51 Pegasi b Postdoctoral Fellowship, University of California, Santa Cruz
- JHU EPS Journal Club Long Presentation Award ($2,000), 2018
- 50th DPS Hartmann Travel Grant ($500), 2018
- Stephen E. Dwornik Award at the 49th Lunar and Planetary Science Conference – Best Graduate Oral Presentation, 2018
- Johns Hopkins University 2018-19 Technology Fellowship ($5,000)
- Johns Hopkins University 2018-19 Dean's Teaching Fellow
- Titan Surface Meeting travel grant, 2018
- Johns Hopkins University J. Brien Key Fund ($500), 2017
- Women in Astronomy IV travel grant, 2017

- Johns Hopkins University Shark Tank Education Innovation Competition ($3,000), Winner, 2016
- Johns Hopkins University Owen Scholars Award ($6,000/yr, 3yrs), 2014
- University of Science and Technology of China (USTC), Outstanding Bachelor Thesis, 2014
- USTC, Outstanding Award in Undergraduate Research Program, 2013
- USTC Outstanding Student Scholarship (Grade 1), 2013
- USTC Outstanding Student Scholarship (Grade 2), 2012
- USTC Outstanding Student Scholarship (Grade 3), 2011

Teaching Experience

Instructor

Johns Hopkins University **Baltimore, MD**

AS.270.328 Planetary Exploration: Techniques and Data Analysis (New Course) *Fall 2018*

Teaching Assistant and Guest Lecturer

Johns Hopkins University **Baltimore, MD**

Teaching Assistant AS.270.114 Guided Tour of the Planets *Spring 2019*
Guest Lecturer (1 lecture) AS.270.335 Planets, Life and the Universe *Fall 2018*
Guest Lecturer (1 lecture) AS.270.114 Guided Tour of the Planets *Spring 2018*
Teaching Assistant AS.270.335 Planets, Life and the Universe *Fall 2017*
Guest Lecturer (1 lecture) AS.270.410 Planetary Surface Processes *Fall 2017*
Teaching Assistant AS.270.114 Guided Tour of the Planets *Spring 2017*
Guest Lecturer (1 lecture) AS.270.366 Spacecraft Instrumentation Project *Spring 2017*
Guest Lecturer (1 lecture) AS.270.114 Guided Tour of the Planets *Spring 2017*
Restructure AS.270.114 Guided Tour for Shark Tank Education Innovation Competition *Winter 2017*
Teaching Assistant AS.270.103 Introduction to Global Environmental Change *Fall 2016*
Guest Lecturer (1 lecture) AS.270.114 Guided Tour of the Planets *Spring 2016*
Teaching Assistant AS.270.114 Guided Tour of the Planets *Spring 2016*

Additional Training

- EON-ELSI Winter School in Earth–Life Science *Winter 2018*
- JHU Teaching Academy–Teaching Institute Certificate Program *Summer 2016*

Referred Publications

[7]: **Xinting Yu**, Sarah M. Hörst, Chao He, Bryan Crawford, and Patricia McGuiggan, "Where does Titan Sand Come From: Insight from Mechanical Properties of Titan Organic Analogs", *Journal of Geophysical Research - Planets*, 123, 2310-2321, https://doi.org/10.1029/2018JE005651, 2018. **(Featured article in *JGR-planets* and article on *Universe Today*: link)**

[6]: Chao He, Sarah M. Hörst, Nikole K. Lewis, **Xinting Yu**, Julianne I. Moses, Eliza M.-R. Kempton, Mark S. Marley, Patricia McGuiggan, Caroline V. Morley, Jeff A. Valenti, and Véronique Vuitton, "Photochemical Haze Formation in the Atmospheres of Super-Earths and Mini-Neptunes", *The Astronomical Journal*, 156, 1, https://doi.org/10.3847/1538-3881/aac883, 2018.

[5]: Chao He, Sarah M. Hörst, Nikole K. Lewis, **Xinting Yu**, Julianne I. Moses, Eliza M.-R. Kempton, Patricia McGuiggan, Caroline V. Morley, Jeff A. Valenti, and Véronique Vuitton, "Laboratory Simulations on Haze Formation in Cool Exoplanet Atmospheres: Particle Color and Size Distribution", *Astrophysical Journal Letters*, 865(1), L3, https://doi.org/10.3847/2041-8213/aab42b, 2018.

[4]: **Xinting Yu**, Sarah M. Hörst, Chao He, Patricia McGuiggan, and Nathan T. Bridges, "Direct Measurement of Interparticle Forces of Titan Aerosol Analogs ("Tholin") Using Atomic Force Microscopy", *Journal of Geophysical Research - Planets*, 122(12), 2610-2622, doi:10.1002/2017JE005437, 2017.

[3]: **Xinting Yu**, Sarah M. Hörst, Chao He, Nathan T. Bridges, Devon M. Burr, Joshua A. Sebree, and James K. Smith, "The Effect of Adsorbed Liquid and Material Density on Saltation Threshold: Insight from Laboratory and Wind Tunnel Experiments", *Icarus*, 297, 97-109, doi:10.1016/j.icarus.2017.06.034, 2017.

[2]: **Xin-Ting Yu**, Jun Zhang, Ting Li, and Shu-Hong Yang, "Case Studies of EUV Cyclones and Their Associated Magnetic Fields", *Res. Astron. and Astrophys.*, 15, 1525, doi.org/10.1088/1674-4527/15/9/009, 2015.

[1]: **Xinting Yu**, Jun Zhang, Ting Li, Yuzong Zhang, and Shuhong Yang, "Homologous Cyclones in the Quiet Sun", *Astrophysical Journal Letters*, 782(2), L15, doi.org/10.1088/2041-8205/782/2/L15, 2014.

Conference Proceedings

[12]: **Yu X.**, Hörst S.M., He C., McGuiggan P., and Crawford B., Interpreting Sand Formation on Titan: Insight from Interparticle Forces and Mechanical Properties of Titan Organic Analogs, *DPS*, 203.07D, 2018.

[11]: **Yu X.**, Hörst S.M., He C., McGuiggan P., and Crawford B., Where Does Titan Sand Come From: Insight from Interparticle Forces and Mechanical Properties of Titan Organic Analogs, *Titan Surface Meeting*, 2018.

[10]: **Yu X.**, Hörst S.M., He C., Crawford B., and McGuiggan P., Where Does Titan Sand Come From: Insight from Mechanical Properties of Titan Organic Analogs, *LPSC*, 1786, 2018, **Stephen E. Dwornik Award–Best Graduate Oral Presentation.**

[9]: Radebaugh, J., Barnes, J. W., Mackenzie S., Hörst S. M., **Yu X.**, Lorenz, R. D., ... Bishop, B., The importance of Sand for Understanding Dune Processes and Surface Conditions of Titan, *LPSC*, 2083, 2018.

[8]: **Yu X.**, Hörst S.M., He C., McGuiggan P., and Bridges N.T., Direct Measurements of Surface Energy, Elastic Modulus and Interparticle Forces of Titan Aerosol Analog ("Tholin") Using Atomic Force Microscopy, *AGU fall meeting*, 221907, 2017.

[7]: He C., Hörst S.M., Lewis, N., **Yu X.**, McGuiggan P., and Moses J.I., Laboratory Simulations on Haze Formation in Cool Exoplanet Atmospheres, *DPS*, 300.01, 2017.

[6]: **Yu X.**, Hörst S.M., He C., McGuiggan P., and Bridges N.T., Direct Measurement of Interparticle Adhesion of Titan Aerosol Analogs ("Tholin") Using Atomic Force Microscopy, *5th International Dune Workshop*, 3048, 2017.

[5]: Stephen L.F. Sutton, Devon M. Burr, Nathan T. Bridges, James K. Smith, Sarah M. Hörst, **Xinting Yu**, Jasper F. Kok, Francis A. Turney, J.R. Marshall, and D.A. Williams, The Titan Wind Tunnel in the NASA Planetary Aeolian Laboratory: Facility Improvements, *LPSC*, 1964, 2017.

[4]: **Xinting Yu**, Sarah M. Hörst, Chao He, Nathan T. Bridges, Devon M. Burr, and Joshua A. Sebree, Quantifying Water Content and Equilibration Properties of Wind Tunnel Materials, *DPS-EPSC*, 425.03, 2016.

[3]: Devon M. Burr, Emily Nield, Joshua Emery, Nathan T. Bridges, James K. Smith, John Marshall, Jasper Kok, **Xinting Yu**, and Sarah M. Hörst, Experimental (wind tunnel) investigations into aeolian entrainment: application to extraterrestrial environments, *32nd IAS International Meeting of Sedimentology*, 2016.

[2]: **Xinting Yu**, Sarah M. Hörst, Chao He, Nathan T. Bridges, and Devon M. Burr, Quantifying Density, Water Adsorption and Equilibration Timescale of Wind Tunnel Materials, *LPSC*, 2683, 2016.

[1]: NT Bridges, DM Burr, J Marshall, JK Smith, SM Hörst, E Nield, and **X Yu**, New Titan Saltation Threshold Experiments: Investigating Current and Past Climates, *AGU*, P12B-05, 2015.

Skills

Language: Chinese (native), English (fluent), Japanese and Spanish (conversational)

Programming: Matlab, IDL, C++, Fortran, Python, Mathematica

Computer: Windows, Linux, Mac OS, MS Office, LaTeX

Laboratory Instruments: RGA-MS, SEM, AFM, Nanoindenter, Pycnometer

Laboratory Skills: Vacuum Techniques, Photochemistry Synthesis, Low/High Temperature and Low-Pressure Gas Reactions

Invited Seminars and Colloquia

∘ University of California, Santa Cruz, Earth and Planetary Sciences *Spring 2019*

Outreach

∘ 49th LPSC microblogger *Spring 2018*

∘ 15th Annual Physics Fair organizer, Johns Hopkins University *Spring 2018*

Professional Affiliations

∘ Division for Planetary Sciences of the American Astronomical Society

∘ American Geophysical Union

Other Experiences

∘ Active Animal Interpretation Volunteer in the Maryland Zoo in Baltimore since Fall 2017

∘ Active Animal Handling Volunteer in the Maryland Zoo in Baltimore since Summer 2017

∘ Yelp Elite Member since 2017, Review of the Day (ROTD) winner

- Active Education Volunteer in the Maryland Zoo in Baltimore since Fall 2016
- Volunteer Translator (adding English subtitles and translate English to Chinese) for Educational Videos, Youzimu Subtitle Team, 2016–2017
- Completed my 9th Full Marathon in 2016 Chicago
- Completed Full Marathon in 2015 Honolulu, 2015 Philadelphia, 2015 Marine Corps
- Women's 3rd place, IFC Anhui Stair Climb Competition, 2014 Hefei
- Completed Full Marathon 2014 Baltimore, 2014 Honolulu
- Completed Full Marathon in 2013 Beijing, 2013 Shanghai, 2014 Xiamen
- Completing Half Marathon in 2015 Xiamen, 2014 Kangbao, 2013 Yangzhou, 2012 Yangzhou, 2012 Beijing